Characterisation of stripline resonators in a waveguide

David Zöpfl

Supervisor:
Univ.-Prof. Dr. Gerhard Kirchmair

A thesis presented for the degree of
Master of Science

Superconducting Quantum Circuits
Institute of Experimental Physics
University of Innsbruck
Austria

April 2017

Abstract

In this thesis a chiral waveguide was simulated and analysed, which is sensitive on the circular polarisation of the incoming signals. The waveguide either reflects the incoming signal or allows it to propagate through. This leads to an asymmetric behaviour in transmission. To launch a signal, the waveguide was combined with spiral antennas in the simulations. After everything was put together, transmission from the one to the other antenna was found to be symmetric, which is also implied by the antenna theorem.
Microwave cavities made from aluminium and copper were measured in reflection configuration at room temperature. Different setups for the coupling to the cavities were probed. Each of the setups was measured using coupling pins of different length. This was done in the under-coupled, as well as in the over-coupled regime. The expected relation between the coupling quality factor Q_c and the pin length was seen. Q_c showed an exponential behaviour in the under-coupled and an approximate linear behaviour in the over-coupled regime. The extracted information provides knowledge to design coupling pin length in the future.
U-shaped stripline resonators made from aluminium and niobium were placed in a rectangular waveguide. The setup was cooled down to achieve superconductivity. The quality factors (internal and coupling) and the resonance frequency of the resonators were determined by measurements. The striplines were mounted such that they were critically coupled. Measurements were performed with the striplines placed in a copper and an aluminium waveguide. Simulations performed with HFSS show general agreement on the resonance frequency and the coupling quality factor. A developed circuit model, representing the stripline as a transmission line shows good agreement and yields a resonance frequency in the measured range. Internal quality factors of about 7×10^5 to 1×10^6 were found for the niobium striplines in the single photon limit and between 1×10^5 and 6×10^5 for the aluminium ones. A trend for increasing quality factors with increasing input powers was measured. Performing temperature ramp up measurements to around 1 K showed, that the internal quality factor of the niobium striplines increases, while the striplines made from aluminium showed a decreasing Q_i.

Acknowledgement

First of all I want to thank my supervisor Univ.-Prof. Dr. Gerhard Kirchmair for giving me the opportunity to do my Master thesis in his research group. He was always available, if needed, and gave his most welcome support. The level he cares about the members of our research group is not taken for granted, but very much appreciated.
I also want to thank all members of our research group for their support. Especially I want to thank Christian Schneider for his support in the implementation of the circle fit and his help in the circuit model, describing the stripline resonator. In addition, I have to thank Oscar Gargiulo, for providing an excellent coffee (nearly) every afternoon.
Obviously I also have to thank my parents for the tremendous support throughout my studies. Without their support this would not have been possible.
Moreover, I want to thank Johann Moser and Theresa Baur, for proof reading this thesis on short notice. Finally, I also want to thank everyone, who supported me in this thesis, and is not mentioned personally.

Contents

Chapter 1

Introduction

Quantum computation promises to solve problems not feasible using classical computers [1]. In particular quantum computers are superior in solving systems, which follow the laws of quantum mechanics [2]. With classical computers they can only be solved using a lot of computation time in combination with approximations [2].
Instead of classical bits of a classical computer, which can be either in the state 0 or 1, quantum bits, or qubits, are used in quantum computers. They can be in an arbitrary superposition of 0 and 1, which is described by the laws of quantum physics [1]. There are different approaches on what systems can be used as quantum bits. Some basic requirements have to be considered [3]. Qubits have to follow the laws of quantum mechanics and are, similar to bits, two level systems. It has to be possible to initialise, measure and perform arbitrary operations on the qubits. This leads to the requirement of a set of single qubit gates. In addition, their coherence time is required to be a lot longer than the gate time. To do quantum computation then, it is sufficient to have a universal two qubit gate [4].
One of the most successful approaches is to use ions as qubits and use the discrete energy states of its (outer) electron as the required two level system [5]. Ions carry disadvantages, because the ion itself cannot be customised, as it is given by nature. Some of the disadvantages can be overcome by using superconducting qubits [5]. The two level system is provided by the non linearity of a Josephson junction. Superconducting qubits offer advantages, as they can be customised in their properties, but have to be fabricated. For instance exotic properties, not found in natural atoms, can be designed [6]. Also the strong coupling regime can be investigated, which is not possible with weakly coupled natural atoms [6]. However the fabrication is quite a challenge.
To do computation superconductivity is required, therefore the samples have to be cooled down, to a few Kelvin or below. To communicate with these qubits microwaves are required, with a frequency in the range of several GHz. This frequency prevents thermal effects to play a major role, at the base temperature of the cryostat. Given the frequency and followed by the size of structures, it is possible to see them with the bare eye, giving advantages in the assembling process.
A challenge is to couple the qubits in a controlled way to the environment. This is necessary to perform operations on the qubit and to do the readout [7]. In this thesis stripline resonators were investigated, which can be used for readout. Of particular interest were the internal losses, compared to the coupling to the environment, also called coupling losses. Coupling losses include losses to the read out circuit, and should be a lot higher

than internal losses [8], which lead to a loss of information. The stripline resonators are discussed in chapter 7. To extract their properties a fitting routine was developed based on the theoretical model, discussed in chapter 6. In this chapter also the measurement of microwave cavity resonators is discussed. Their measurement results can be extracted with a similar readout routine as discussed for the resonators in chapter 7. Moreover it is investigated, to which extent simulation results can be trusted. They give important information on the design considerations for future setups. In addition they allow to test setups, that are not possible to build in experiments and give useful insight. Simulations were run and compared to the measurement results, which got also compared to predictions from theory. This was done for the resonators in chapter 6 and 7.

In the first chapter of this thesis, a brief background for describing transmission lines is presented. Based on this, the 3D waveguide is discussed, as a special case of a 3D transmission line. The rectangular and the circular waveguides are discussed in detail. As it is not feasible to solve all systems rigorously using Maxwell's equations, a background about network analysis is given in the next section. This concludes the theoretical chapters. Following this, in chapter 5, the design of a chiral waveguide is presented. It either allows transmission or reflects a signal, depending of its circular polarisation. As this asymmetry was lifted, when combing the waveguide with spiral antennas, required for the feed, this project did not leave the simulation stage.

Chapter 2

Transmission lines

Transmission lines consist of two conductors, allowing electromagnetic waves to propagate along them. Starting with Kirchhoff's laws, solutions can be found and are presented in this chapter. A general solution is obtained and also the special case of a terminated transmission line is discussed.
The discussion is based on [9], where a more profound description is given.

2.1 Fundamentals

A transmission line typically consists of two conductors with a dielectric in between. A circuit model for an infinitesimal part of a transmission line is shown in figure 2.1, where R and L is the resistance respectively inductance per unit length for both conductors, while G and C represent the shunt resistance and capacitance per unit length.

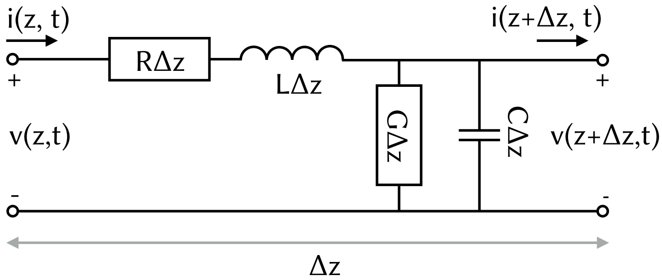

Figure 2.1: Circuit model of an infinitesimal part of a transmission line.

Applying Kirchhoff's laws to the circuit yields two differential equations, one for the voltage and one for the current derivation with respect to the position:

$$v(z,t) - v(z+\Delta z, t) = R\Delta z j(z,t) + L\Delta z \frac{\partial j(z,t)}{\partial t} \tag{2.1}$$

$$j(z,t) - j(z+\Delta z, t) = G\Delta z v(z+\Delta z,t) + C\Delta z \frac{\partial v(z+\Delta z,t)}{\partial t} \tag{2.2}$$

In this equation j is the current and v the voltage. Taking $\Delta \to 0$ leads to differential equations. Assuming that the time dependence is of a form similar to $\sin(\omega t)$, where

ω is the frequency and t the time, we find:

$$\frac{dV(z)}{dz} = -(R + i\omega L)I(z) \tag{2.3}$$

$$\frac{dI(z)}{dz} = -(G + i\omega C)V(z) \tag{2.4}$$

The above system is solved by these two equations simultaneously:

$$\frac{d^2V(z)}{dz} - \gamma^2 V(z) = 0 \tag{2.5}$$

$$\frac{d^2I(z)}{dz} - \gamma^2 I(z) = 0 \tag{2.6}$$

Here γ represents the complex propagation constant:

$$\gamma = \alpha + i\beta = \sqrt{(R + i\omega L)(G + i\omega C)} \tag{2.7}$$

From equations 2.3 and 2.4 propagating wave solutions follow:

$$I(z) = I_0^+ e^{-\gamma z} + I_0^- e^{\gamma z}, \tag{2.8}$$

with $e^{\pm\gamma z}$ representing the propagation. The equation for the voltage is of the same form. Inserting equation 2.4 into the expression 2.8 and comparing to $V = Z_0 I$ yields:

$$Z_0 = \frac{R + i\omega L}{\gamma} = \sqrt{\frac{R + i\omega L}{G + i\omega C}} \tag{2.9}$$

In addition we find that:

$$\frac{V_0^+}{I_0^+} = Z_0 = -\frac{V_0^-}{I_0^-} \tag{2.10}$$

Furthermore we obtain the following relation for the wavelength λ on the transmission line:

$$\lambda = \frac{2\pi}{\beta} \tag{2.11}$$

This is linked to the phase velocity v_p:

$$\beta = \frac{\omega}{v_p} \tag{2.12}$$

In the lossless case $\alpha = 0$ in equation 2.7, as a result of this only the propagating part remains. For that case Z_0 simplifies to $\sqrt{L/C}$.

2.2 Terminated lossless transmission line

Here terminating a lossless transmission line with a load is considered. The load has a different impedance than the transmission line, leading to reflections at the load. Afterwards the special case of the load being an open is discussed.
A load, Z_L is placed at the position $z = 0$, see figure 2.2.

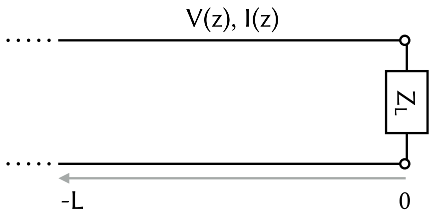

Figure 2.2: Load at the end of transmission line with length L.

We consider a voltage source generating an incident wave of the form $V(z) = V_0^+ e^{-i\beta z}$. Z_0 relates the voltage to the current (equation 2.10). At the load the impedance changes to Z_L and the current-voltage relation, $Z_L = V(z=0)/I(z=0)$, has to be full filled. As a consequence a part of the incident wave will be reflected, such that we end up with:

$$V(z) = V_0^+ e^{-i\beta z} + V_0^- e^{i\beta z} \tag{2.13}$$

The expression for the current follows using equation 2.10, having a $-$ instead of the $+$ sign.
Inserting and rearranging the current-voltage relation at the load, $Z_L = V(0)/I(0)$. We obtain:

$$V_0^- = \frac{Z_L - Z_0}{Z_L + Z_0} V_0^+ \equiv \Gamma V_0^+, \tag{2.14}$$

where equation 2.10 was used. Γ is the voltage reflection coefficient. Now we can express the voltage along the transmission line as:

$$V(z) = V_0^+ (e^{-i\beta z} + \Gamma e^{i\beta z}) \tag{2.15}$$

The influence of the load is seen along the transmission line. The impedance of the load, seen at location z on the transmission line, changes in dependence of z. The so called input impedance, which is the impedance seen at the beginning of the transmission line, $-L$ in this case, is given by:

$$Z_{in} = \frac{V(-L)}{I(-L)} = \frac{1 + \Gamma e^{-2i\beta L}}{1 - \Gamma e^{-2i\beta L}} Z_0 = \tag{2.16}$$

$$= \frac{Z_L + iZ_0 \tan(\beta L)}{Z_0 + iZ_L \tan(\beta L)} Z_0 \tag{2.17}$$

Case of $Z_L = \infty$

In the special case of an open, $Z_L = \infty$, the voltage and current on the transmission line, equation 2.15, simplify to:

$$V(z) = 2V_0^+ \cos(\beta z) \tag{2.18}$$

$$I(z) = -\frac{2iV_0^+}{Z_0} \sin(\beta z) \tag{2.19}$$

Furthermore, the input impedance, equation 2.17, simplifies to:

$$Z_{in} = -iZ_0 \cot(\beta L) \tag{2.20}$$

These expressions are plotted in figure 2.3 for different lengths of the transmission

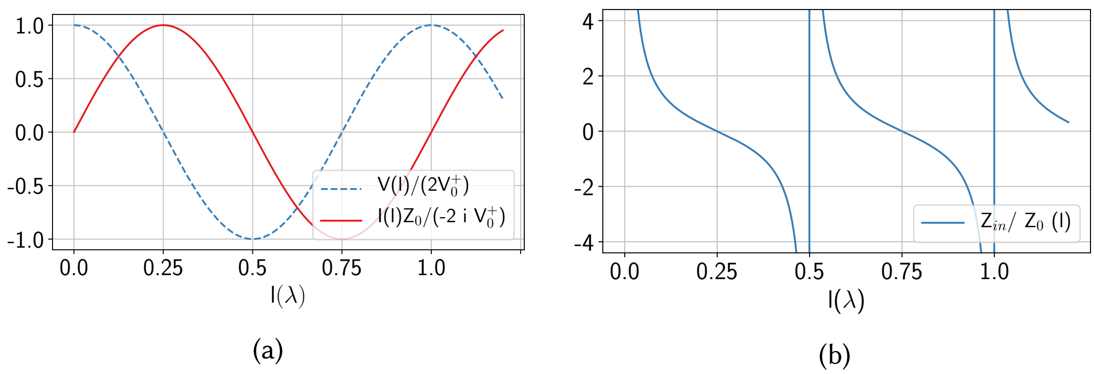

Figure 2.3: (a) Voltage and current distribution, (b) input impedance of an open lossless transmission line in dependence of its length, l, in comparison to the wavelength.

line in terms of the incident wave's wavelength. For a transmission line with a length of multiple of $\lambda/2$, resonances occur, as Z_{in} goes to infinity. For this case the current at the end of the transmission line is always zero, with the number of nodes depending on the order of the resonance. The maximum of the current is in the middle of the transmission line, $L/2$. The voltage has a node in the middle and reaches a maximum at both ends. In case of an open on both sides of the transmission line, the same dependencies are found for a length of $\lambda/2$. The input impedance goes to infinity, the current and voltage have the discussed form.
A later derived circuit model for the stripline resonator (chapter 7) will be based on the discussions in this chapter. In the following chapter a 3D waveguide, being the special case of a 3D transmission line, is discussed.

Chapter 3

Waveguide theory

The following chapter is based on [9], where a more profound description of the discussed is given.
A waveguide is the special case of a 3D transmission line. Its purpose is to transmit, or guide, electromagnetic waves from one end to the other. In the discussed case, the electromagnetic waves are in the regime of microwave frequencies.
In this chapter solutions of Maxwell's equation will be presented, which give solutions for the electric and magnetic field inside of the waveguide. At first, more general, for waveguides with an arbitrary shape, but uniform in the propagation direction. Based on that the rectangular and the circular waveguide will be discussed.
We distinguish between three different kinds of modes, the TEM (transverse electromagnetic) mode, which has no electric or magnetic field component in the propagating (longitudinal) direction. In contrast to the TEM mode there are the TE (transverse electric) and the TM (transverse magnetic) modes which have either only magnetic or electric field components in the propagation direction.

3.1 General solution

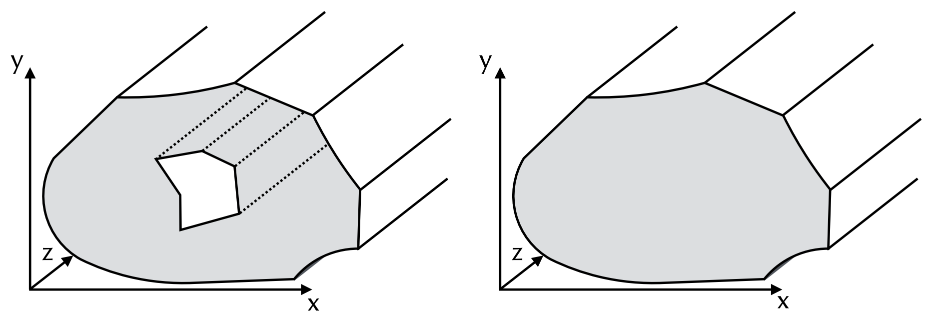

(a) (b)

Figure 3.1: Sketch of a single conductor 3D waveguide, filled with a dielectric. With (a) and without a central conductor (b). The propagation direction is the z direction.

In this chapter a waveguide with an arbitrary, closed shape in the x, y plane, uniform and infinite in the z direction, is discussed (see figure 3.1). It is either hollow or filled with a dielectric. Furthermore, it can have a central conductor of arbitrary, closed shape in the x, y plane, not touching the outer conductor of the waveguide, uniform and infinite in the z direction. It is assumed that the waveguide is a perfect electric conductor (PEC), such that no losses are present and the propagation constant becomes $\gamma = \beta$. Furthermore it is assumed, that the fields are harmonic in time:

$$\vec{E}(x, y, z, t) = \vec{E}(x, y, z)e^{i\omega t} \tag{3.1}$$

and

$$\vec{H}(x, y, z, t) = \vec{H}(x, y, z)e^{i\omega t} \tag{3.2}$$

With the independence of field in the $x - y$ plane from the z position, the electric field can be split in transverse, $\vec{e}(x, y)$, and longitudinal, $\vec{e_z}(x, y)$, components. The reason for this independence is, that the waveguide looks identical, independent from the z coordinate. Therefore the field must not depend on the z position. Using this we arrive at the following expression:

$$\vec{E}(x, y, z) = [\vec{e}(x, y) + \hat{z}e_z(x, y)]e^{-i\beta z} \tag{3.3}$$

$$\vec{H}(x, y, z) = [\vec{h}(x, y) + \hat{z}h_z(x, y)]e^{-i\beta z} \tag{3.4}$$

The magnetic field, $\vec{H}$, follows analogue. Assuming that there are no sources in the waveguide, Maxwell's equations reduce to:

$$\nabla \times \vec{E} = -i\omega\mu\vec{H} \tag{3.5}$$

$$\nabla \times \vec{H} = i\omega\epsilon\vec{E} \tag{3.6}$$

Using these equations and that the only z-dependency is of $e^{-i\beta z}$, we obtain the following relations:

$$H_x = \frac{i}{k_c^2}\left(\omega\epsilon\frac{\partial E_z}{\partial y} - \beta\frac{\partial H_z}{\partial x}\right) \tag{3.7}$$

$$E_x = \frac{-i}{k_c^2}\left(\beta\frac{\partial E_z}{\partial x} + \omega\mu\frac{\partial H_z}{\partial y}\right) \tag{3.8}$$

Similar equations follow for the y components. k_c is the cutoff wave number given by:

$$k_c = \sqrt{k^2 - \beta^2} \tag{3.9}$$

3.1.1 TEM modes

For the TEM modes $E_z = H_z = 0$. In this case nontrivial solutions exist, if $k_c = 0$. This can be also seen following equations 3.5 and 3.6:

$$\beta^2 E_x = \omega^2\mu\epsilon E_x \tag{3.10}$$

and leads to:

$$\beta = \omega\sqrt{\mu\epsilon} = k \tag{3.11}$$

Using the Helmholtz equation in combination with equation 3.10 we obtain:

$$\left(\frac{\partial^2}{\partial_x^2} + \frac{\partial^2}{\partial_y^2}\right)E_x = 0 \tag{3.12}$$

Similar relations can be found for the y component, as well as the magnetic field. Thus the transverse fields have the same form as the fields between two conductors. Moreover, the electric field can be expressed as the gradient of a scalar potential ($e(x,y) = -\nabla_t \Phi(x,y)$). Hence the voltage between the conductors can be found as the potential difference and the current by applying Ampere's law. Furthermore, it can be shown that the wave impedance, calculated by E_x/H_y, equals the vacuum wave impedance.
The solutions for the fields have the same form as the field between two conductors, thus TEM modes can only exist in the two conductor case. In case of a single conductor no voltage difference is possible, which prevents TEM modes from propagating.

3.1.2 TE modes

In the case of TE modes, $E_z = 0$ while $H_z \neq 0$. Equation 3.7 and the equivalent expression for the y component have to be solved, to obtain expressions for the fields. These expressions simplify due to $E_z = 0$:

$$E_x = -\frac{i\omega\mu}{k_c^2}\frac{\partial H_z}{\partial y} \tag{3.13}$$

Furthermore, $k_c \neq 0$ is a requirement, as H_x would diverge otherwise (see equation 3.7). To solve these expressions H_z has to be found, which is then sufficient to solve all the transverse field components. Similar to the TEM case this is done by solving the Helmholtz equation, taking the boundary conditions into account. Using the known decomposition for the transverse and longitudinal components, $H_z(x,y,z) = h_z(x,y)e^{-i\beta z}$, it reduces to the following equation:

$$\left(\frac{\partial^2}{\partial_x^2} + \frac{\partial^2}{\partial_y^2} + k_c^2\right) h_z = 0 \tag{3.14}$$

The wave impedance is now frequency dependent:

$$Z_{TE} = \frac{E_x}{H_y} = \frac{k\eta}{\beta} \tag{3.15}$$

with η being the free space impedance.

3.1.3 TM modes

The TM modes are solved the same way, the only difference being that $E_z \neq 0$, while $H_z = 0$. Therefore a solution for E_z has to be found, which can again be separated in transverse and longitudinal components, $E_z(x,y,z) = e_z(x,y)e^{-i\beta z}$.
The solution is obtained using the Helmholtz equation:

$$\left(\frac{\partial^2}{\partial_x^2} + \frac{\partial^2}{\partial_y^2} + k_c^2\right) e_z = 0 \tag{3.16}$$

The wave impedance is given by:

$$Z_{TM} = \frac{E_x}{H_y} = \frac{\beta\eta}{k} \tag{3.17}$$

The scaling factor is the inverse of the TE mode.

3.2 Rectangular waveguide

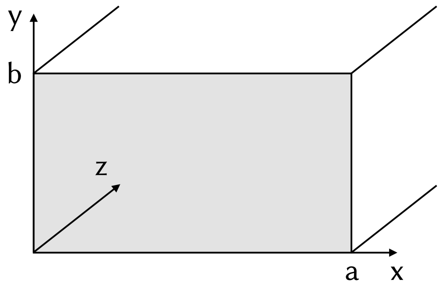

Figure 3.2: Sketch of the rectangular waveguide. It can be hollow or filled with a dielectric.

In this chapter a waveguide with a rectangular cross section is discussed. It is sketched in figure 3.2, assuming $a > b$. The waveguide can be hollow or filled with a dielectric, the walls are again PEC and it is infinitely long.
Due to the case of just a single conductor being present, TEM modes cannot exist, as those need two conductors to propagate.

3.2.1 TE modes

With the knowledge of the boundary conditions it is possible to solve the Helmholtz equation (3.14) from the previous chapter. Therefore specific expressions for the E and H field are obtained. The method to solve the partial differential equation is through separation of variables, also in the transverse field, such that: $h_z(x,y) = X(x)Y(y)$. Putting that into equation 3.14 leads to:

$$\frac{1}{X}\frac{d^2X}{dx^2} + \frac{1}{Y}\frac{d^2Y}{dy^2} + k_c^2 = 0 \tag{3.18}$$

There are two independent parts, one depending on x and the other one on y. To satisfy this for all values, both parts must be equal to a constant, such that $k_x^2 + k_y^2 = k_c^2$.
A general solution for this system is given by:

$$h_z(x,y) = (A\cos k_x x + B\sin k_x x)(C\cos k_y y + D\sin k_y y), \tag{3.19}$$

with A, B, C and D being constants. Due to the boundary conditions the tangential electric field components on the walls have to vanish. This condition cannot be directly applied to the magnetic field, therefore we use relation 3.8, which links the magnetic to the electric field. After applying the boundary conditions the following solution is obtained:

$$h_z(x,y) = A_{mn}\cos\frac{m\pi x}{a}\cos\frac{n\pi y}{b} \tag{3.20}$$

Required by the boundary conditions, $k_x = m\pi/a$ and $k_y = n\pi/b$, with m, n being integers. Combining the above equation with equation 3.8, an expression for the electric field in x direction is obtained. To get the y component, the equivalent equations for the y direction are taken. The electric field components in the x and in the y direction, including the propagation in the z direction, are given in the following expressions:

$$E_x = \frac{i\omega\mu n\pi}{k_c^2 b} A_{mn} \cos\frac{m\pi x}{a} \sin\frac{n\pi y}{b} e^{-i\beta z} \tag{3.21}$$

$$E_y = -\frac{i\omega\mu m\pi}{k_c^2 a} A_{mn} \sin\frac{m\pi x}{a} \cos\frac{n\pi y}{b} e^{-i\beta z} \tag{3.22}$$

Similar equations follow for the magnetic field components. The propagation constant β is given by:

$$\beta = \sqrt{k^2 - k_c^2} = \sqrt{k^2 - \left(\frac{m\pi}{a}\right)^2 - \left(\frac{n\pi}{b}\right)^2} \tag{3.23}$$

For β being real, or $k^2 > k_c^2$, one refers to propagation modes, while for β being imaginary the modes are exponentially attenuated. This leads to the formulation of a cutoff frequency for each mode, given by:

$$f_{mn}^c = \frac{k_c}{2\pi\sqrt{\mu\epsilon}} = \frac{1}{2\pi\sqrt{\mu\epsilon}} \sqrt{\left(\frac{m\pi}{a}\right)^2 + \left(\frac{n\pi}{b}\right)^2} \tag{3.24}$$

For a frequency above the respective cutoff frequency a mode can propagate. The TE mode with the lowest cutoff frequency, also called the fundamental mode, is the TE_{10} mode with $f_{10}^c = 1/(2a\sqrt{\mu\epsilon})$. The wave impedance is given by 3.15.

3.2.2 TM modes

As $H_z = 0$ here, we solve the Helmholtz equations directly for the E field, where exactly the same solutions as in equation 3.19 are obtained. The only difference is that the boundary conditions, which have to be the same, can be applied directly. The obtained expressions for the x and y component of the electric field are:

$$E_x = -\frac{i\beta m\pi}{k_c^2 a} B_{mn} \cos\frac{m\pi x}{a} \sin\frac{n\pi y}{b} e^{-i\beta z} \tag{3.25}$$

$$E_y = -\frac{i\beta n\pi}{k_c^2 b} B_{mn} \sin\frac{m\pi x}{a} \cos\frac{n\pi y}{b} e^{-i\beta z} \tag{3.26}$$

The expressions for the propagation constant and cutoff frequencies are identical to the case of the TE modes. However the difference here is, that in contrast to the TE modes, m, as well as n, have to be 1 or above for the field components not to vanish. This makes the TM_{11} the lowest one in frequency. That can be easily checked for the electric field components using 3.25 and 3.26, and is also true for the magnetic field. Therefore the TE_{10} mode is the fundamental one in any rectangular waveguide. The wave impedance is given by 3.17.
The modes and their respective cutoff frequencies in comparison to the fundamental mode are plotted in figure 3.3. In figure 3.4 the shape of the fields for the first modes are plotted.

3.3 Circular waveguide

For a waveguide with circular shape, equivalent to a rectangular one, only TE and TM modes can propagate due to the lack of the central conductor. In figure 3.5 a circular

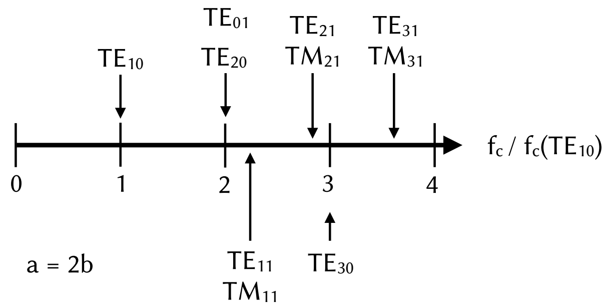

Figure 3.3: Cutoff frequencies for different modes in a rectangular waveguide, compared to the fundamental mode cutoff, for the case $a = 2b$.

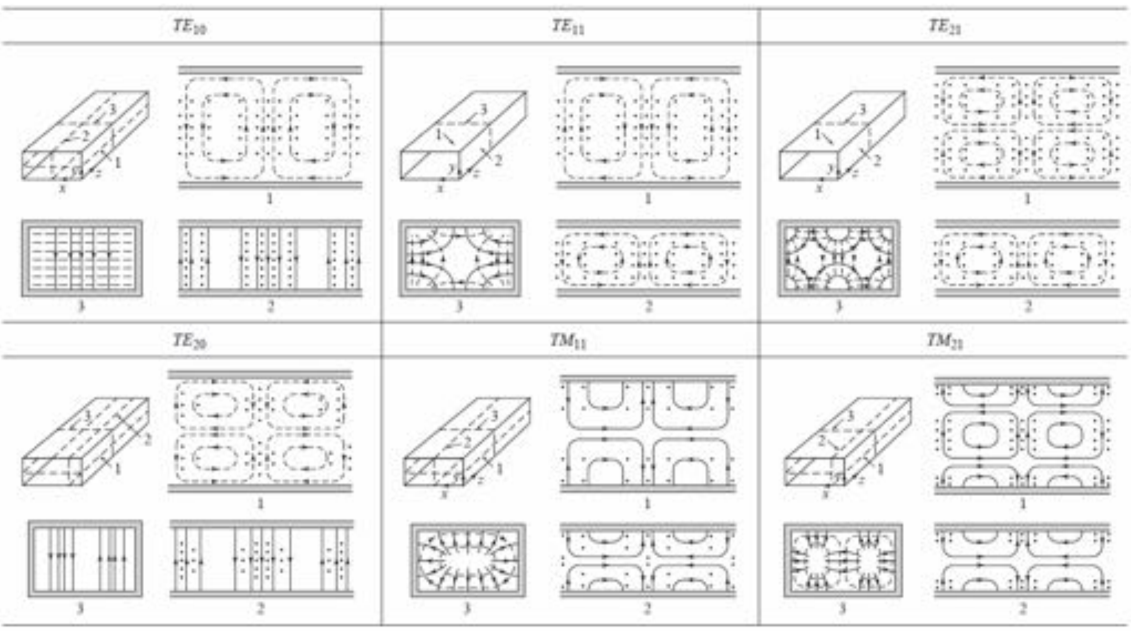

Figure 3.4: E and B field in a rectangular waveguide for different modes. The E field is depicted with solid lines, the B field with dashed ones. From: [9], figure 3.9.

waveguide with the radius a is sketched. It is useful to work in cylindrical coordinates. Again conditions following from equation 3.5 and 3.6 apply and have to be worked out in cylindrical coordinates.

3.3.1 TE modes

For the TE modes H_z has to be solved, which again is divided into a transverse and a longitudinal part, such that $H_z = h_z(\rho, \phi)e^{-i\beta z}$. Applying the Helmholtz equation in cylindrical coordinates leads to:

$$\left(\frac{\partial^2}{\partial \rho^2} + \frac{\partial}{\rho \partial \rho} + \frac{\partial^2}{\rho^2 \partial \phi^2} + k_c^2\right) h_z(\rho, \phi) = 0 \tag{3.27}$$

Similar to the rectangular waveguide, h_z is separated into $h_z(\rho, \phi) = R(\rho)\Phi(\phi)$, leading to two independent parts. For $\Phi(\phi)$ a general solution, already using the required 2π

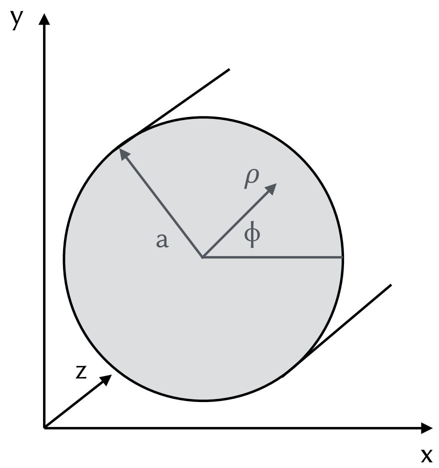

Figure 3.5: Sketch of the circular waveguide, which can be hollow or filled with a dielectric.

periodicity, can be written as

$$\Phi(\phi) = A\sin(n\phi) + B\cos(n\phi), \tag{3.28}$$

with n being an integer. Inserting this solution for the $\Phi(\phi)$ part into 3.27, we identify Bessel's differential equations. Thus $R(\rho)$ has to be of the form

$$R(\rho) = CJ_n(k_c\rho) + DY_n(k_c\rho),$$

where k_c, C, D are constants and J_n, Y_n are the Bessel functions of first and second kind. Due to Y_n diverging at 0, it cannot be accepted as a solution, leading to the following solution for the whole system:

$$h_z(\rho,\phi) = (A'\sin(n\phi) + B'\cos n\phi)J_n(k_c\rho) \tag{3.29}$$

The boundary conditions are, again as in the case of the rectangular waveguide, that the tangential electric field has to vanish. To apply them, we first use the equivalent for equation 3.8 in cylindrical coordinates. Afterwards we are able to apply the boundary conditions. To satisfy them it is required that:

$$J_n'(k_c a) = 0, \tag{3.30}$$

, where J_n' is the derivative of the Bessel function. Therefore $J_n'(p_{nm}') = 0$, with p_{nm}' being the m-th root of the n-th order derivative of the Bessel function. This leads to:

$$k_{c,nm} = p_{nm}'/a \tag{3.31}$$

This has to be computed to get the cutoff wave number. The roots of the Bessel functions can be found in literature (for example [9], table 3.3) and it is obtained that the fundamental TE mode is the TE_{11} mode.
The cutoff frequencies are given by:

$$f_{nm}^c = \frac{p_{nm}'}{2\pi a\sqrt{\mu\epsilon}} \tag{3.32}$$

The final field components are obtained using 3.6 and 3.29, also including the $e^{-i\beta z}$ propagation in z directions:

$$E_\rho = -\frac{i\omega\mu n}{k_c^2\rho}(A\cos n\phi - B\sin n\phi)J_n(k_c\rho)e^{-i\beta z} \tag{3.33}$$

$$E_\phi = -\frac{i\omega\mu}{k_c}(A\sin n\phi - B\cos n\phi)J_n'(k_c\rho)e^{-i\beta z} \tag{3.34}$$

For the components describing the magnetic field, similar equations follow.

3.3.2 TM modes

To solve the TM modes, where $H_z = 0$, identical steps to the TE mode calculation are carried out for the electric field instead of the magnetic field. Everything is identical until the boundary conditions are applied, which can be directly applied as they concern the E field.
Using the equivalent of equation 3.29 for the E field we apply the boundary conditions to obtain:

$$J_n(k_c a) = 0 \Leftrightarrow k_c = \frac{p_{nm}}{a} \tag{3.35}$$

Where p_{nm} is the m-th root of the n-th Bessel's function. The cutoff frequency is found using the cutoff wave number:

$$f_{nm}^c = \frac{p_{nm}}{2\pi a\sqrt{\mu\epsilon}} \tag{3.36}$$

Comparing the cutoff frequencies, we see that the fundamental mode for the circular waveguide is the TE_{11} mode, followed by TM_{01}. In figure 3.6 the cutoff frequencies of the first modes in comparison to the TE_{11} mode are plotted. The expressions for the field

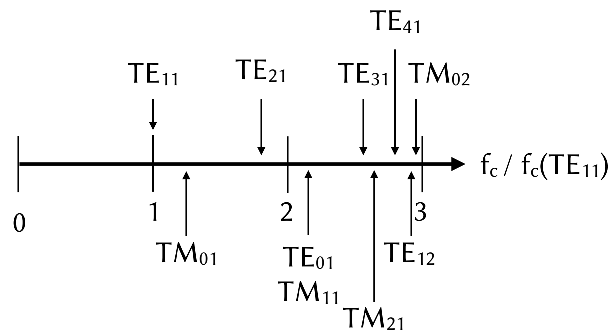

Figure 3.6: Cutoff frequencies for different TE and TM modes in a circular waveguide, compared to the fundamental mode cutoff. Similar to: [9], figure 3.13.

components of the transverse electric field are given in the following:

$$E_\rho = -\frac{i\beta}{k_c}(A\sin n\phi + B\cos n\phi)J_n'(k_c\rho)e^{-i\beta z} \tag{3.37}$$

$$E_\phi = -\frac{i\beta n}{k_c^2\rho}(A\cos n\phi - B\sin n\phi)J_n(k_c\rho)e^{-i\beta z} \tag{3.38}$$

For the components describing the magnetic field, similar equations follow. In figure 3.7 the shape of the fields for the first modes are plotted.

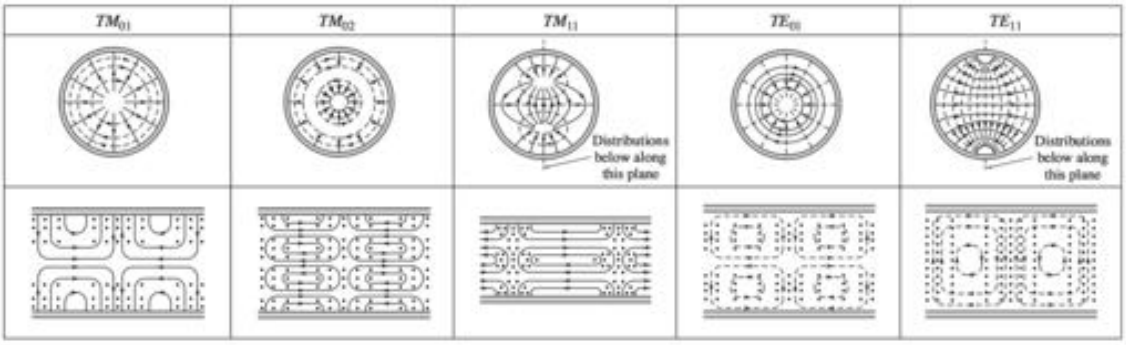

Figure 3.7: E and B field in a circular waveguide for different modes. The E field is depicted with solid lines, the B field with dashed ones. From: [9], figure 3.14.

In this and the chapter before basic elements used for circuits were discussed rigorously. In the following chapter, methods of analysing more complex networks consisting of several devices are given.

Chapter 4

Network analysis

Methods and considerations for analysing networks are presented in this chapter. In contrast to before, a network consisting of multiple basic elements (e.g. a transmission line) is considered. Typically power flows or voltages between terminals are of interest, which are then sufficient to characterise the network and avoid solving Maxwell's equations for the whole system. The following chapter is based on [9], where a more profound description is given.

In the case of low frequencies, where the dimensions of the circuit are below the wavelength, the phase delay can be neglected. Therefore quasi static solutions apply, such that currents and voltages can be assigned conventionally. This is different in the case of microwave frequencies, where the circuit dimensions are similar or larger than the wavelength. Hypothetically one could solve Maxwell's equations and get the electric and magnetic field at every point in space. However, this is cumbersome and yields more information than needed, thus it is not the regular approach.

Usually a set of voltages, currents or the power flow between two terminals is of interest. Such a setup can be extended, joining multiple units together, and due to the knowledge of its components, conclusions for the whole setup can be drawn. Typically some basic devices are analysed rigorously within some simplifications (e.g. the waveguide or transmission line in the previous chapters) to gain knowledge about their behaviour. Joining several basic devices together, intuition about their behaviour exists. The whole network is then typically analysed using the tools of network analysis.

4.1 Equivalences for voltage and current

For the two conductor case, like the transmission line or the briefly discussed waveguide with an inner conductor, a voltage can be assigned as the potential difference between both conductors. The current can be found using Ampere's law, leading in combination with the voltage to the impedance.

For the case of a single conductor this is not possible. In figure 4.1 the electric field of the fundamental mode in a rectangular waveguide is sketched. We see that it critically depends for which point x the voltage is measured over y. This also implies difficulties on how to define voltages. This leads to the formulation of voltage (and current) equivalences for the single conductor case. Therefore some considerations should be taken into account. First of all, the voltage and current should concern a single mode and

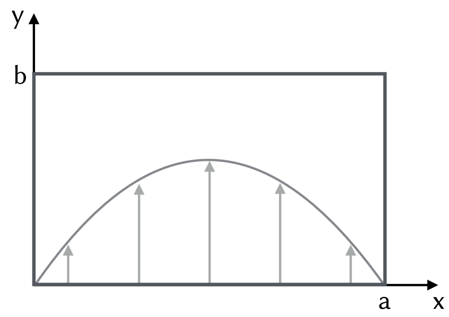

Figure 4.1: Sketch of the E field magnitude in a rectangular waveguide for the fundamental mode.

should be given by the transverse fields, the voltage by the electric and the current by the magnetic field. In addition, the power flow should follow by multiplying the fields. Moreover, the familiar relation between current, voltage and the impedance, $Z = V/I$ should hold.
The idea is then to extend equation 2.8, which is the current over a transmission line and the similar expression for the voltage such that:

$$\vec{E}_t(x,y,z) = \frac{\vec{e}(x,y)}{C_V}(V^+e^{-i\beta z} + V^-e^{i\beta z}) = \frac{\vec{e}(x,y)}{C_V}V(z) \tag{4.1}$$

In the case of the fundamental mode of the rectangular waveguide:

$$\vec{e}(x,y) = \sin\left(\frac{\pi x}{a}\right)\hat{y}, \tag{4.2}$$

where $\hat{y}$ is the unit vector in y direction. Also taking the equivalent equation for current into account and applying the considerations from above one obtains solutions for the constants. C_V, for the electric field, which is linked to the voltage and C_I for the magnetic field, which is linked to the current.
The above illustrates a possibility to obtain expressions for voltage, current and power flow equivalences in the case of a single conductor using some basic requirements in combination with relations derived previously.

4.1.1 Concept of impedance

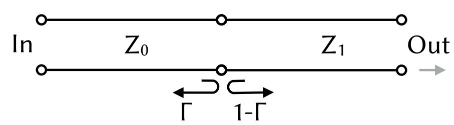

Figure 4.2: Sketch of reflection upon an impedance change. Γ notes the reflected part of the signal, the remaining part, $1-\Gamma$, continues to the output.

This section briefly summarises the different kinds of impedances, which are necessary connections between circuit theory and field theory.
There is the intrinsic impedance of a material, which is determined by the material properties μ and ϵ and is given by $\eta = \sqrt{\mu/\epsilon}$. For vacuum it is around 377 Ω.
Moreover, there is the wave impedance, given by E_t/H_t, being the ratio between the

electric and the magnetic transverse fields. It depends on the type of mode (TEM, TE or TM) and is typically also frequency dependent.
In addition, the impedance is obtained by the relation between voltage and current, V/I, which is also known as the characteristic impedance.
It should be noted, that upon every change of impedance, reflections occur, which is sketched in figure 4.2. The amount of reflection is given by the reflection coefficient, Γ, which was derived in chapter 2.2.

4.2 Scattering parameters

For microwave frequencies it is often difficult to assign and measure currents or voltages [10]. Furthermore, only measuring magnitude neglects the complex nature of these quantities. Therefore the scattering matrix is a useful tool. Its entries give the relation between the input ($\vec{a} = (V_1^+, V_2^+, ..., V_n^+)^T$) and the output voltage ($\vec{b} = (V_1^-, V_2^-, ..., V_n^-)^T$).

$$\begin{bmatrix} b_1 \\ b_2 \\ \vdots \\ b_n \end{bmatrix} = \begin{bmatrix} S_{11} & S_{12} & \cdots & S_{1n} \\ S_{21} & S_{22} & \cdots & S_{2n} \\ \vdots & \vdots & \ddots & S_{2n} \\ S_{n1} & S_{n2} & \cdots & S_{nn} \end{bmatrix} \begin{bmatrix} a_1 \\ a_2 \\ \vdots \\ a_n \end{bmatrix} \tag{4.3}$$

This leads to the specific entries of the scattering matrix:

$$S_{ij} = \left.\frac{b_i}{a_j}\right|_{a_k=0, k\neq j} = \left.\frac{V_i^-}{V_j^+}\right|_{a_k=0, k\neq j} \tag{4.4}$$

This means that port j is driven with an incident wave with the voltage V_j^+, while there is no input from any other port. To avoid reflections, every port besides i should be terminated with an impedance matched load. The magnitude of V_i^- is measured and the relation to the input voltage on port j gives the S parameter.

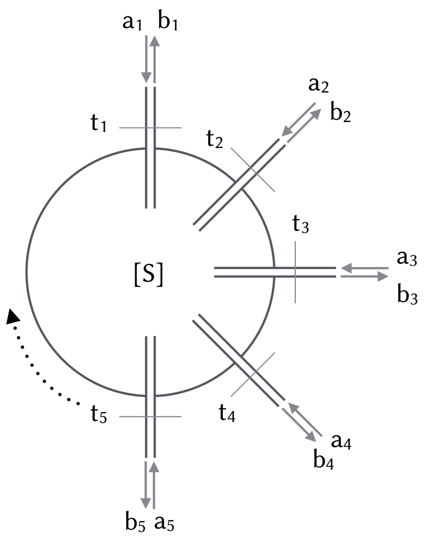

Figure 4.3: Sketch of how the S parameters are obtained for a n port network. t_i denotes the different terminals.

In figure 4.3 it is depicted how S parameters are obtained between different terminals

t for a multiple port network. The corresponding S_{mn} parameter gives the transmission from terminal n to terminal m. In case of a single port network the S parameter reduces to the reflection coefficient:

$$b_1 = \Gamma a_1 = S_{11} a_1$$

In a more complicated network, having multiple ports, every entry in the scattering matrix is related to a reflection coefficient.
Knowing the scattering parameters is a full description of the network. Algebraic conversions to other, in that sense equal, descriptions of a network like the impedance matrix

$$[V] = [Z][I]$$

exist.
In the case of a lossless network, the S matrix is purely imaginary and also unitary.
For the case of a reciprocal network, the scattering matrix is symmetric. Reciprocity implies that the obtained values are equal, whether one probes the transmission from terminal n to m or vice versa. This means that

$$S_{mn} = S_{nm},$$

which leads to a symmetric scattering matrix.
In many of the experiments a reciprocal 2-port network is present, meaning that the knowledge of S_{11} and S_{21} is sufficient to fully characterise the network.

Chapter 5

Design of a circular chiral waveguide

This chapter discusses the design of a waveguide working as a polarisation sensitive element, where the polarisation of the propagating microwave leads either to reflection or transmission. The purpose is to achieve directionality and then to align qubits in the propagating direction. The idea is to only allow communication between the qubits in one direction.
Therefore it is necessary to achieve some kind of non-reciprocal S parameter, $S_{21} \neq S_{12}$. The idea was to design a circular waveguide and use the dependency between its diameter and the cutoff frequency. A screw-like waveguide was designed, where the inner and outer diameter give different cutoff frequencies for circular right and left polarisation. In the following spiral antennas for the feed were designed. Finally, putting everything together, it was obtained that the whole setup was symmetric and the directionality was not achieved, as the antennas exactly lift the asymmetric effect.
To gain information about the features of the designed structures, simulations using the software HFSS where performed. Details about HFSS are given at the end of this chapter.

5.1 Chiral waveguide

A chiral waveguide was designed as a polarisation sensitive element. The dependency of the cutoff frequency on the radius, see equation 3.32, for the circular waveguide was used. A waveguide with two different radii, an inner and an outer one, similar to a screw-like structure was designed, figure 5.1(b). Circular polarised microwaves should either see the outer diameter, or the smaller, inner, diameter depending on their polarisation. The polarisation, which is able to pass is the same for both directions. In this particular case right handed polarised waves can pass while left handed polarised waves get reflected. The chiral part of the waveguide follows this equation:

$$R(x,\phi) = r - d\sin\left(\frac{x\pi}{pitch} + m\phi\right)^2 \tag{5.1}$$

Here x is the propagation direction and ϕ is the angle, similar to cylindrical coordinates around x. R gives the current radius in the y,z plane. This equation is similar to the one describing a corrugate spiral in [11], where a similar waveguide is discussed. In the above equation m refers to the folding of the spiral structure, which is 1 here, $pitch$ is the period of the corrugation. So we see, that the waveguide is periodic in the pitch and also 2π periodic for ϕ. Furthermore, for any value of x, a value for ϕ can be found, where the cross section looks identical to any other point. A detailed description of the wave propagation in such a helical waveguide can be found in [12].

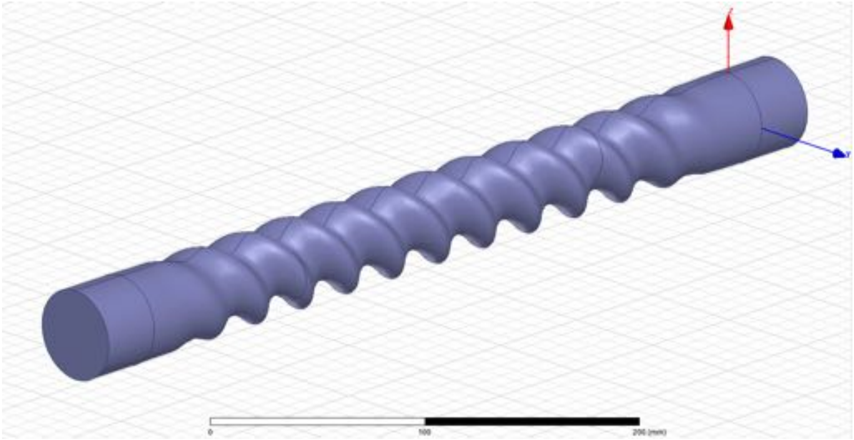

(a)

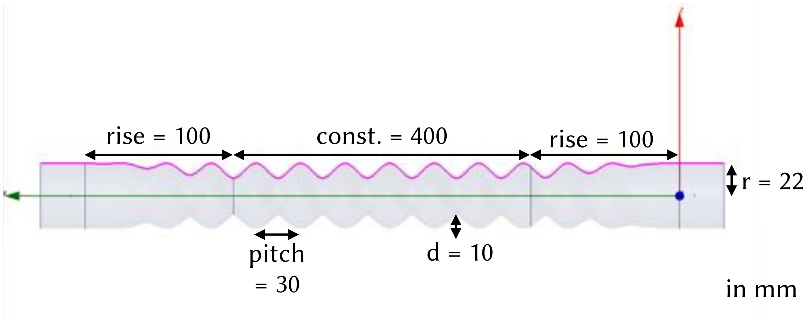

(b)

Figure 5.1: (a) Chiral waveguide model used for the HFSS simulations. (b) Side view of the model including dimensions.

The exact dimensions of the waveguide are specified in figure 5.1(b). For the sections marked with 'rise', the depth d is modulated sinusoidal, $d_{\text{rise}} = \sin(\pi x/(2\text{rise}))$, until it reaches the desired value. The S parameters are obtained performing HFSS simulations. The target was to have (nearly) lossless transmission of right handed polarised signal to the other end and left handed polarised signal attenuated sufficiently, in a suitable bandwidth of several GHz. The expectations were, that above the cutoff for the outer radius, the right polarised mode is dominating, until the frequency gets above the cutoff for the inner radius. From there, on the left circular polarised wave propagates as well and both polarisations should be transmitted with about equal strength.
In figure 5.2 the circular S parameters for right to right handed versus left to left handed polarisation are plotted. They are plotted in transmission and reflection. A bandwidth from around 6 GHz to nearly 9 GHz is obtained, where right handed signal passes, while the left handed one is suppressed by a factor of 100 to 1000. In this range the waveguide works as a polarisation sensitive element, as expected, which was the main goal of these simulations. Looking at the reflection parameters, nearly all the left handed polarised signal is reflected. In case of the right handed polarised signal, only a minor fraction of the signal gets reflected. The reason for the S parameters not entirely adding up, can be normalisation issues from HFSS. In addition, scattering to other modes, like left handed

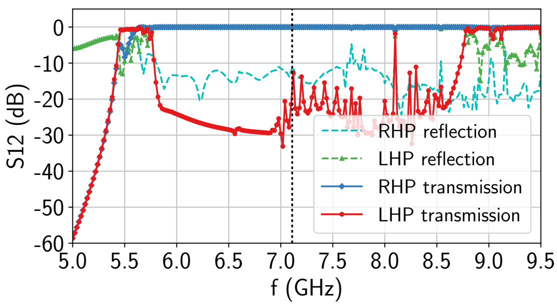

Figure 5.2: S parameters are plotted for transmission of right to right (blue) and left to left (red) polarised waves through the waveguide. The right polarised signal propagates (nearly) lossless. The left polarised signal gets attenuated by a factor 100-1000 between around 6 GHz to 9 GHz. From around 7 GHz onwards ripples in the left to left polarised S parameter are observed. The cutoff of the TM_{01} mode (dotted line) is around 7 GHz. Possibly coupling to this mode takes place.

to right handed is not plotted here.This effect was seen to be around −15 dB or lower, so more than an order of magnitude below the transmission of the right polarised mode.
Two observations are of particular interest. The first one is that while the left handed signal is suppressed, it is not attenuated exponentially. A mode below the cutoff frequency is supposed to be attenuated exponentially. Here, below 9 GHz the left handed mode is suppressed, but its amplitude remains overall constant independent of the frequency until around 6 GHz. The reason is most likely, that some kind of coupling between the two modes takes place. So its actual cutoff is, as for the right polarised mode around 5.5 GHz, only suppressed in a range of nearly 3 GHz.
In addition, from about 7 GHz onwards ripples are observed. Comparing to the cutoff frequencies of the different modes (see figure 3.6), the TM_{01} mode starts propagating in the range, where the ripples start (see figure 5.2). Likely some coupling to this mode takes place.

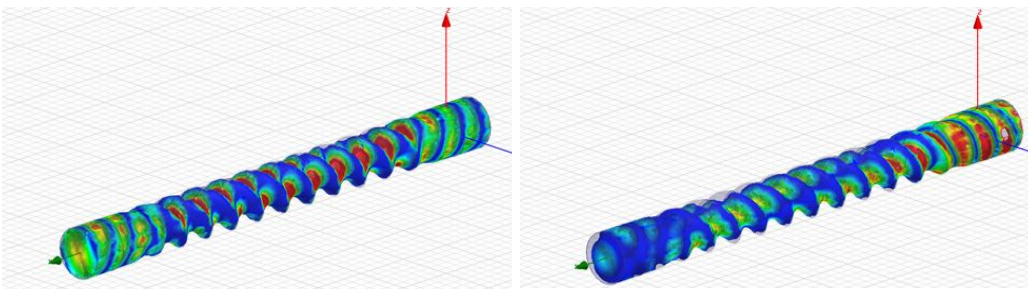

(a) (b)

Figure 5.3: In (a) the right handed polarised mode is excited on one end and the magnitude of the electric field is plotted. It propagates through without major losses. In (b) the left handed polarised mode is excited (on the right end). Only a weak field is observed at the other end, the remaining part was reflected. Red corresponds to a strong field, blue to a weak field (in comparison), the scale is linear. The fields are shown at a frequency of 8 GHz.

Figures 5.3(a), (b) compare the magnitude of the electric field at a frequency of 8 GHz. In (a) the right handed polarised mode is excited and one can see that the mode propagates through the waveguide. In (b) the same for the left handed polarised mode is depicted. The field through the waveguide is weaker, while on the end, where the exci-

tation happens, it is stronger, which is due to the expected reflections.
To summarise, a waveguide was designed, which successfully works as a polarisation sensitive element. Right polarised waves propagate without (or minor) losses, while left polarised waves are attenuated by a factor of 100 to 1000. In the next step an antenna has to be designed to launch circular polarised microwaves in the waveguide.

5.2 Spiral antenna for feed

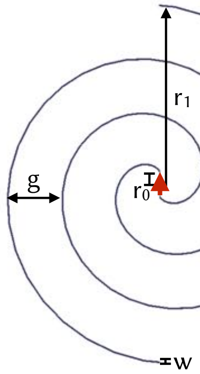

Figure 5.4: Sketch of an Archimedean spiral antenna, r_0 is the initial inner radius, r_1 the outer radius, g the growth rate, and w the inner width of the arms. The red arrow in the center marks the port, which is between the two conductors of the antenna.

For the feed an Archimedean spiral antenna was designed, to launch circular polarised waves. Such an antenna is described by [13]

$$r(\phi) = g\phi + r_0,$$

where r is the radius in dependence of ϕ, which is continuous over 2π, g is the growth rate and r_0 the initial radius. A sketch of such an antenna is plotted in figure 5.4, its design causes the radiation to be circularly polarised. The radiated polarisation is opposite in both directions, so in case it radiates dominantly right handed in one direction, it radiates left handed in the other direction. This is exactly what is required for the antenna in combination with the waveguide to be directional.

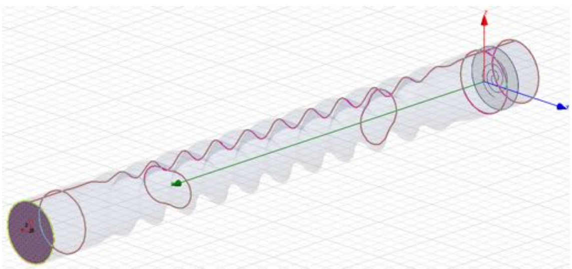

Figure 5.5: Setup used for the simulations. Waveguide in combination with the antenna, oriented right handed in the waveguide. The signal received at the other, far end (highlighted port) is of interest.

There are many free parameters which critically influence the radiation characteristics and the bandwidth. The method to find a suitable setup was to put the spiral

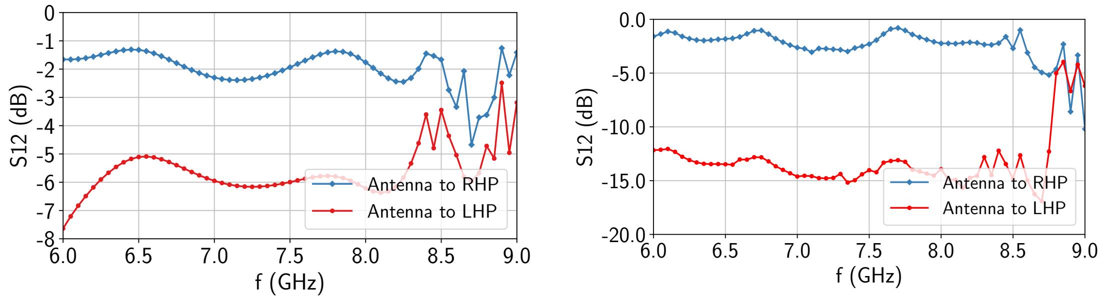

(a) (b)

Figure 5.6: (a) HFSS simulation results of a spiral antenna in a circular waveguide, with the same dimensions as the chiral one (without the corrugation). Transmission of right vs. left polarised waves to the far end of the waveguide. (b) Same as (a), in the chiral waveguide.

antenna in a circular as well as into the chiral waveguide, change its properties and find a suitable working layout. Due to the coupling to the waveguide walls, it was necessary to investigate the antenna in the waveguide. The parameters, which can be optimised, include the number of turns, the inner radius, the growth per turn and the width of the antenna wire itself (see figure 5.4). In figure 5.5 the simulation setup of the spiral antenna in the waveguide is shown. In there the antenna is oriented right handed in the waveguide. The fields of the antenna are discussed in the next section, 5.3.
In figure 5.6 the obtained results are plotted. In (a) the simulation results for the antenna transmission from one end to the other one of a circular waveguide is plotted. This waveguide has the same dimensions as the chiral one without the corrugation. The antenna is excited and the transmission from the antenna port, which is in the center of the antenna, to the far end of the waveguide is shown. The transmission difference between the right and left handed polarisation is the one which had to be increased, while the right handed polarised signal should be as strong as possible. The setup plotted here works satisfyingly and is of sufficient bandwidth.
In (b) the same spiral antenna is placed at the end of the chiral waveguide and the same parameters are plotted. The right handed polarised part propagates similar as in the circular waveguide, which is within the expectations. Additional attenuation of the left handed polarised wave is observed. Probably it is not as strong as expected when compared with figure 5.2, where around 20 dB to 30 dB are expected, while approximately 10 dB are observed. An explanation is that earlier the left polarised excitation was ideal, which is not the case any more using the antenna, and thus a stronger left polarised signal reaches the other end.
Mirroring the antenna, the radiation is exactly opposite.
To summarise, a spiral antenna was designed, which can be used to launch right circular polarised waves into the chiral waveguide. The following, final, step is to put two antennas into a chiral waveguide.

5.3 Two spiral antennas in chiral waveguide

Simulations were run with two spiral antennas in the chiral waveguide, one at each end. The main target was to detect, if an asymmetric effect in their transmission from one to to the other one can be observed, meaning $S_{12} \neq S_{21}$. The antennas were oriented

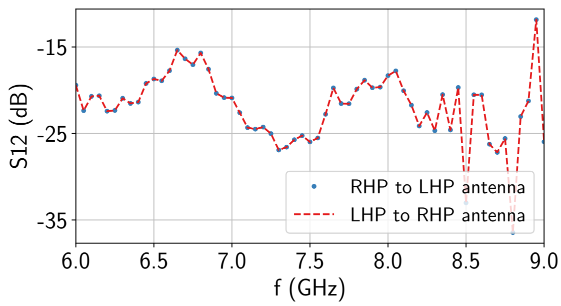

Figure 5.7: Simulation results for the chiral waveguide with two antennas. S parameters showing the transmission between the antennas in both directions, which are identical. This implies that the setup including the antennas is symmetric.

in the same direction, such that looking into the waveguide (propagation direction of interest), one antenna radiates right handed and the other one left handed. So the power received by the left handed antenna should be much higher, as it gets the signal from the right handed antenna, which passes the waveguide without (or minor) attenuation. The other way round, the signal, the right handed antenna receives is much weaker, as it comes from the left handed antenna, and thus is mainly reflected by the chiral waveguide.
So a difference in the S parameters was expected, but they turned out to be exactly identical (figure 5.7). Comparing this to the E field magnitude plots, figure 5.8 the behaviour is not completely intuitive. In (a) the magnitude of the electric field is plotted, for excitation of the right polarised antenna, sitting at the right end. There an equal field strength is observed all over the waveguide, meaning that the wave can propagate through the waveguide without major reflections. In (b) the left polarised antenna, sitting at the left end, is excited. Here the magnitude of the field close to the antenna is stronger than on the other end, meaning that the wave gets reflected with the beginning of the corrugation. This is expected due to the design of the chiral waveguide. Comparing the absolute field strength here to the case without any antenna, the values add up. The strength is about a factor of two weaker than for the case, where the waveguide itself is excited (figure 5.2(a)). This is expected from the transmission S parameter from one antenna to the other end of the waveguide (figure 5.6(b)). This just gives an estimate, as the range for the field strength can be chosen individually by hand.

The reason for the S parameters being symmetric lies in the antenna theorem [14, Chapter 1.7]. It implies that the sending and receiving ability of an antenna is identical. This means for the given setup, that the left handed antenna would get a huge signal, which is right polarised, but is unable to receive most of it. On the other hand, as discussed in the previous section, this left handed antenna sends a fraction of the power right polarised. This part of the signal propagates through and is then well received by the right handed antenna at the other end. Consequently the whole situation is exactly symmetric.
It is stated by the antenna theorem, that reciprocity cannot be broken by antennas in combination with geometric structures. Some other approaches were made with the goal to achieve non symmetric S parameters, which did not succeed. Some of these approaches were to put a planar chiral structure on a substrate into the waveguide, e.g. slit rings [15] or chiral fish scale patterns [16]. The main reason for this not being suitable was the low chiral effect, so both directions were similar in terms of signal.

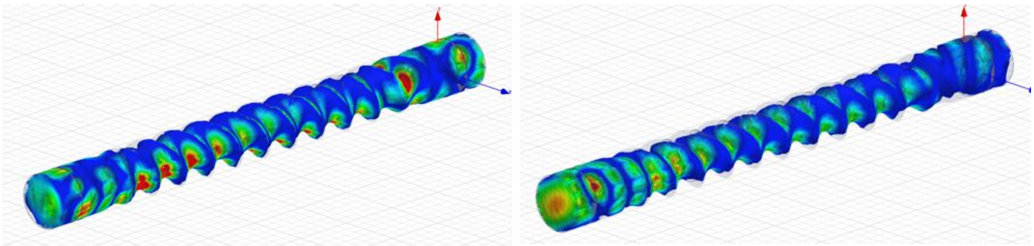

(a) (b)

Figure 5.8: Magnitude of the electric field at 8 GHz. In (a) the antenna is oriented in a way, that it radiates right polarised into the waveguide. There it can be seen that the mode is excited all over the waveguide, the wave propagates through. In (b) the antenna (on the left end) emits left polarised in the waveguide, a major part of the signal gets reflected. Red corresponds to a strong field, blue to a weak field (in comparison), the scale is linear. The fields are shown at a frequency of 8 GHz.

5.4 Conclusions

To summarise, the objective was to design a directional structure. The intention was to use a polarisation sensitive element, a chiral waveguide in the given case, and build qubits coupled to antennas, which should then be coupled to the waveguide.
In the first step, a chiral waveguide was designed as a selective element. Right handed polarised waves could propagate with minor attenuation, whereas left handed polarised waves were reflected to 99% or above. In the second step, a spiral antenna was designed to launch the circular polarised waves. Many parameters could be modified to find the best characteristics, and a satisfying setup was found.
In the final step two antennas were combined in the chiral waveguide. No asymmetry was observed in the S parameters, as the sending and receiving ability of a spiral is symmetric, which is true for any antenna.

5.5 Notes on HFSS

To perform simulations the software HFSS was used, which solves Maxwell's equations inside a given structure (e.g. a waveguide). This chapter presents the fundamentals of how HFSS obtains a solution and lists the necessary steps to start the simulation process. Furthermore, useful considerations and advice on doing the simulations are given.

5.5.1 Basics

HFSS is a finite element solver, which numerically solves Maxwell's equations in a 3D structure [17]. Therefore the structure is divided into tetrahedra, or triangles in case of a surface, called the mesh. The electric and magnetic fields are calculated on the edges of the triangles. A suitable mesh has to be found, which describes the model with sufficient accuracy. This is discussed in chapter 5.5.3.
Using this division into tetrahedra, Maxwell's equations can be transformed to matrix equations and can thus be numerically solved. The magnetic field is computed from the electric field, using $H = \nabla \times \vec{E}/(-i\omega\mu)$, which makes the magnetic field fundamentally

less accurate in comparison [17].
There are two different solution types mainly used in our simulations. The eigenmode gives the resonance frequency and the corresponding field of the setup. For the driven solutions the model is externally excited at given frequencies. To excite the setup, ports are required, which are explained in the next section.
The solution type used for the chiral waveguide was of driven type. Thus the following sections are mainly based on this.

5.5.2 Port and boundary assignment

In the first step a 3D model is drawn, similar to a conventional CAD software. For a waveguide (or similar) the material is set to vacuum or another dielectric, corresponding to the inside of the waveguide. It is possible to place different objects inside the waveguide and assign different materials, the material properties can be customised.
It is advised to assign variables to each dimension, using their dependencies if possible, as this provides a better overview and makes modifications easier.
After completing the structure, ports have to be assigned, to calculate the driven solutions. There are two types of ports, which were used to analyse the chiral waveguide, waveports and lumped ports. Waveports are only possible to assigned to structures supporting travelling waves and are typically assigned to external boundary surfaces. This also implies why the inside of the waveguide has to be either vacuum or a dielectric.
From the dimensions of the waveport the supported modes are calculated and those are used for the excitation [18]. To calculate S_{21}, a second port is required. Integration lines, which are optional when using waveports, can be drawn to get a specific field pattern. Every integration line works as a port on its own again. Combining two ports having a 90° angle and a phase difference in their excitation of 90°, circular polarisation can be generated. Using a different phase difference leads to elliptical polarisation. In

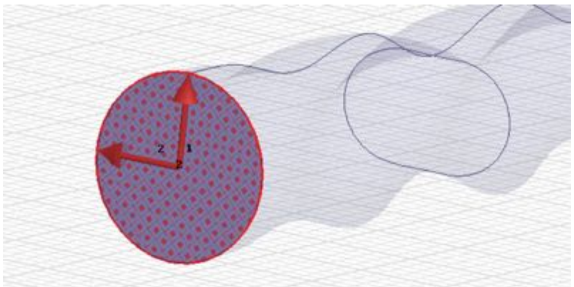

Figure 5.9: Excitation of a port. Integration lines to get circular polarisation.

figure 5.9 a port of the chiral waveguide with two integration lines is shown, necessary for circular polarisation.
For internal ports a lumped port is used. This port requires two conductors, which are excited by a potential difference between them [18]. A lumped port is therefore used for the excitation of the spiral antenna. For this kind of port an integration line is required and is drawn between the two arms of the antenna, which identifies where the potential difference is applied.
Another type of excitation is the incident wave excitation. Different kinds of incident waves exist (e.g. plane, far field) and depending on their type different options exist, like their starting point, direction and polarisation. These kind of excitations are typically

not used in our set of problems, but can be helpful (e.g. when designing antennas).
Similar to ports, which are taken into account in the solution process, different kinds of boundaries exist. Some examples are given here.
One option is to assign finite conductivity to a surface, e.g. to the surface of the waveguide. When designing an element, like an antenna in free space, radiation boundaries exist to gain knowledge about the radiation pattern. These boundaries are required to confine the setup into a finite area and assure a continuous field across them. Similar an air box can be drawn around the structure. An air box is typically vacuum and its purpose is to confine the area, which has to be solved, without interacting with the structure. To full fill this, it should be at least $\lambda/4$ away from the structure.

5.5.3 Creating a solution setup and finding the best mesh

After the model is drawn, the ports and boundaries are assigned, a solution setup has to be created.
Convergence criteria, mainly concerning the ports and the mesh, are defined in there, as well as what kind of basis functions to use. A frequency for the solution setup has to be defined. This frequency should be the maximum frequency, which is of interest for the whole solution. The reason is that the mesh is based on this solution frequency. A higher frequency is linked to a shorter wavelength and the unit length of the mesh should be based on the shortest wavelength to be more accurate. The mesh is computed in an iterative process, which converges, if the different results between two consecutive steps are below a certain limit, given by the convergence criteria.
The solution process, described in the following, is plotted in a flow chart in figure 5.10. At first a mesh is generated, afterwards the current patterns for each port are calculated. Based on them the electric field is computed from the magnetic field and vice visa, at first only at the ports. In case their difference is not acceptable, the mesh at the ports is refined [17]. After sufficient accuracy is obtained, the field inside the whole structure at the probe frequency is solved. The figure of merit for the convergence criteria is the deviation of the S parameter, ΔS. In case this is not reached, the mesh is refined, especially in critical areas, which leads to the adaptive process of finding a suitable mesh.
The accuracy of a solution also depends on the order of the used basis function. In case they are set to 1^{st} order, field values from the vertices of the tetrahedron as well as the middle points of the edges are used for the field interpolation, figure 5.11. This leads to 20 unknown variables per tetrahedron. In case of a 0^{th} order basis function only the values at the vertices are taken into account, leading to 6 unknown variables [17].
Getting a finer mesh also leads to a better description as the solution for the field is obtained in more detail. Thus it might be a better trade-off to use lower order basis functions in combination with a finer mesh. Sometimes it is useful to assign mesh operations for objects, which critically influence the solution and are therefore of high interest. One possibility is to define a maximum unit length for the mesh. An example for that is shown in figure 5.12. In (a) the mesh is plotted using the standard configuration without constraints and in (b) a maximum length per element is defined. For cylindrical or circular structures also an option called surface approximation exists. In there values for the maximum deviation between the structure and the mesh in terms of length and angle is set.
For a given model it has to be seen which kind of mesh fits best, a uniform rule cannot be given. By plotting the mesh itself, it is already possible to see if it might go wrong

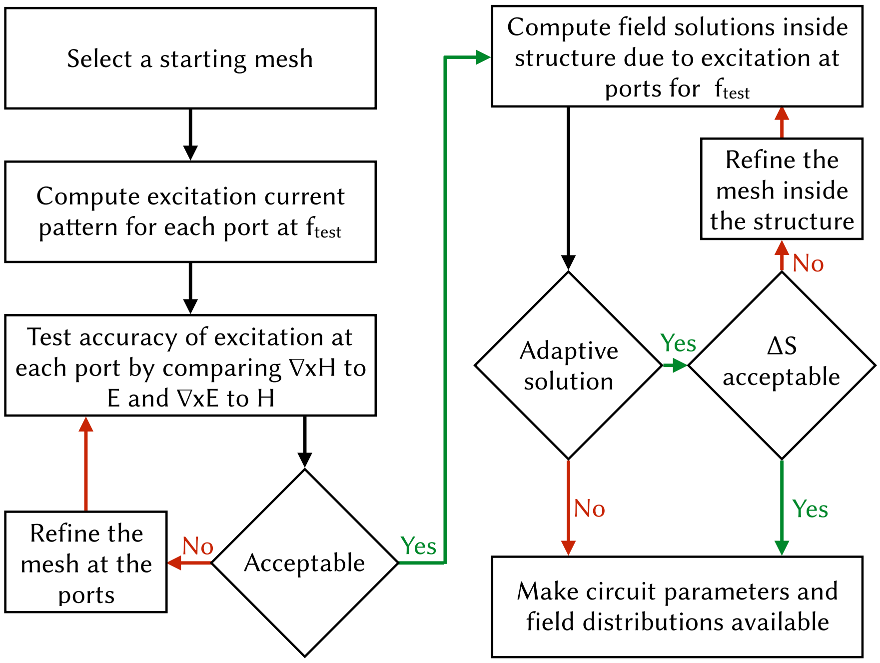

Figure 5.10: Solution process in HFSS to obtain solution for a single frequency. f_{test} refers to the frequency in the solution setup. Details are given in the text. Similar to [17], figure on page 582.

somewhere or if it does not appear to be fine enough. In addition, a possible check is to solve for the eigenmodes. If the change of resonance frequency with the mesh becoming finer is small enough, a suitable mesh is found. Furthermore, one can also monitor features, e.g. a resonance frequency, for its change.
It is always a trade-off between the accuracy of the solution and the computation time. Again a uniform rule cannot be given and it depends on the setup, the required accuracy and the available computational power, how much accuracy is required and reasonable.

5.5.4 Obtaining results

The final step to obtain solutions for the driven type is to perform a frequency sweep. The mesh remains the same for the whole sweep.
Two different options exist, either to solve discretely for each frequency or to do an interpolating sweep. In case of the discrete sweep, the setup is solved for every specific frequency, in addition the fields can be saved. In case of the interpolating sweep, the setup is solved for some points and interpolated in between. HFSS finds the points, where it solves discretely. Interesting features, like resonances, are solved in more detail, other parts in less, which leads to a speed up. There are two major drawbacks using interpolation. In case of a narrow resonance, it can be missed, moreover it is not possible to solve for the fields using interpolation.
It is also possible to set up multiple frequency ranges with different parameters, so one can combine the advantages of the interpolating sweep with the discrete one to some extent.
After the frequency sweep is finished, the results can be obtained. Different parameters like the S parameters can be plotted against the frequency. Moreover, it is possible to set up equations combining variables, like S parameters and plot those. This was necessary

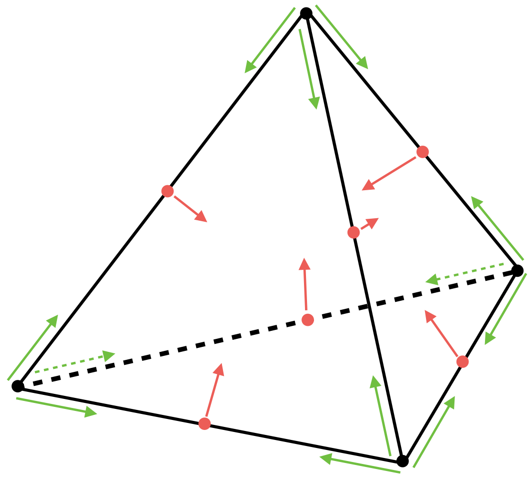

Figure 5.11: HFSS divides the structure into tetrahedra. The tangential field components are stored in the vertices (green). The components tangential to a face and normal to the edge are stored in the midpoints of the edge (red). Somewhere in between the field is interpolated using the stored values. Similar to [17], figure on page 576.

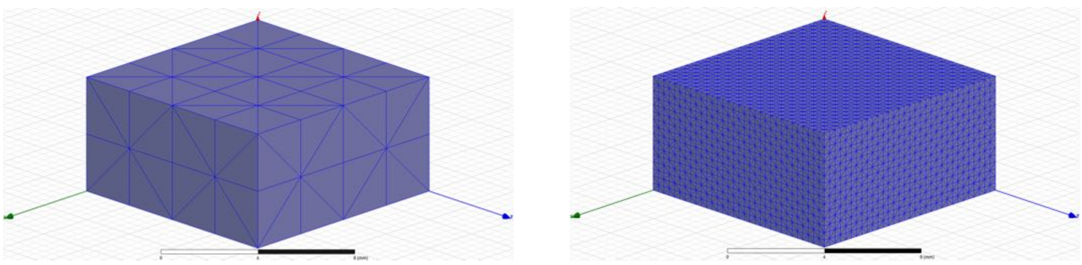

(a) (b)

Figure 5.12: Different meshing setups for a simple box. In (a) a course mesh is used. In (b) a finer mesh is used, where the maximum length per element is limited.

to obtain the results for the circular polarisation in chiral waveguide. The S parameters are normalised, such that $\vec{a}$ and $\vec{b}$ in equation 4.3 carry one watt of power. In addition, only the S parameters for the dominant mode at each port are calculated [17].
In case of the discrete sweep the electric and magnetic fields are stored as well. The magnitude of the fields can be plotted or they can be illustrated using vectors. It is possible to plot the fields on and in any structure. Also planes can be drawn to get a 2D cut of the field at any point. To plot the fields the ports are excited with 1 W by default, this value was used throughout this thesis.
A useful feature is called optimetrics. It allows to change variables (e.g. some dimension) and then carry out the sweep for every given value of it. For example certain values for the growth rate of the spiral antenna can be set and simulations are performed for all variations. The results can be compared to find the best working setup.
To conclude, some basic steps on performing simulations with HFSS were discussed. At first a model has to be drawn, similar to a CAD software. Afterwards ports are assigned, necessary to excite the model. Waveports are used for external excitations, assigned to structures, which support travelling waves. Lumped ports are used for internal excitations, which excite a potential difference between two conductors. Furthermore, bound-

aries can be assigned in this step. In the following a solution setup is created and the mesh is computed. Some options exist to enforce a finer mesh, in case it is required. With this, the setup can be solved, which is either possible using a discrete or an interpolating sweep. Then S parameters are obtained and it is also possible to plot the fields.

Chapter 6

Resonator coupled to a feed line

To obtain information about microwave resonators, they are either measured in reflection or in notch configuration. In reflection configuration the same transmission line is used for the input and readout. The signal gets reflected and propagates back, S_{11} is measured.
In the notch configuration a two port measurement is performed. So S_{21}, the transmission, is measured. The resonator is capacitively coupled to a transmission line connecting the two ports of a measurement device. This represents a so called hanger configuration.
In this chapter at first a circuit model of such a resonator in notch and afterwards in reflection configuration is discussed. A model describing the measured S_{21} parameter (S_{11} for reflection), in dependence of the resonator's properties, is derived. The different loss mechanisms, which are fundamental when describing resonators, are briefly discussed. Afterwards a fit, the so called circle fit, giving information about the properties of a resonator, is discussed. In the final part measurements of a copper and an aluminium cavity are presented and compared in the different configurations.

6.1 Resonator in notch configuration

The notch configuration is depicted in figure 6.1. In (a) it is shown in full generality with arbitrary impedances, where Z_1 and Z_2 are those of the feedline and the coupling, Z_3 depicts the resonator. In (b) the same setup is shown, using specific elements. The resonator is depicted as a LCR oscillator, its losses are modelled with the resistance R. It is capacitively coupled to the feedline, with resistance R_{ext}. The external or coupling losses are losses to this feedline.
Following [19] a model for the readout circuit is derived. It contains the internal and external losses as well as the resonance frequency. The parameters are obtained by fitting the model to the measurement data. The two assumptions therefore are, that it is a two port network and the resonator has a single pole. At first the resonator is also considered to be lossless.
With these assumptions each impedance, seen in figure 6.1(a), can be written as

$$z = \frac{a + ib\omega}{c + id\omega} \tag{6.1}$$

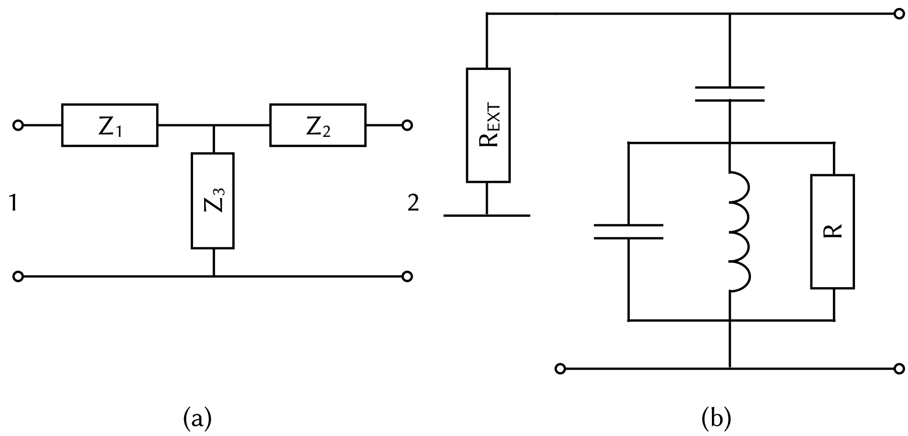

Figure 6.1: Model for a resonator coupled to a transmission line in notch configuration. (a) Circuit with generic impedances, Z_1 and Z_2 depict the transmission line and the coupling , Z_3 is the resonator. (b) The same circuit. Now specific circuit elements are used.

with a to d being complex numbers, which can be different for each impedance. Rewriting these to the S parameters, as those are the measured quantities, and taking the assumptions into account, we obtain:

$$S_{21} = \frac{g + ih\omega}{c + id\omega} \tag{6.2}$$

g and h are complex numbers, c and d are the same as in equation 6.1. For this setup the transmission S parameters are of interest and since the network is reciprocal it is sufficient to know S_{21}.
A lossless resonator shows no transmission on resonance ($S_{21} = 0$), due to the $\pi/2$ shift from the resonator. So it is useful to introduce this property along with the resonance frequency ω_r:

$$S_{21} = \frac{hi(\omega - \omega_r)}{c + di\omega} \tag{6.3}$$

The expression simplifies as the overall magnitude and phase are unimportant, which are related to other losses and imperfections of the transmission line. In addition, $k = c/h$ can be introduced, further simplifying the expression:

$$S_{21} = \frac{i(\omega - \omega_r)}{k + i\omega} \tag{6.4}$$

The measured resonance has the form of a Lorentzian. To arrive at such an expression, it is useful to replace k by $k = \kappa + i\omega_r$, with κ being complex. As k and κ are complex numbers this is valid. We find:

$$S_{21} = \frac{i(\omega - \omega_r)}{\kappa + i(\omega - \omega_r)} = 1 - \frac{\kappa}{\kappa + i(\omega - \omega_r)} \tag{6.5}$$

Here the second part has the form of a Lorentzian

$$L(x) = \frac{1}{\frac{1}{2}\gamma + i(x - x_0)}, \tag{6.6}$$

where γ is the full width half maximum and x_0 the resonance frequency. Furthermore, dissipation is introduced here, which is declared as an additional imaginary part to the resonance frequency: $\omega_r \rightarrow \omega_r + i\epsilon$. Moreover, the introduced κ can be split into its real and imaginary components, $\kappa = \kappa^{Re} + i\kappa^{Im}$. With this S_{21} becomes:

$$S_{21} = 1 - \frac{\kappa^{Re} + i\kappa^{Im}}{(\kappa^{Re} + \epsilon) + i(\omega - (\omega_r - \kappa^{Im}))} \tag{6.7}$$

Comparing this to the Lorentzian, equation 6.6, we recognise that κ^{Im} is an effective shift of the resonance frequency. Therefore, ω_r can be re-written: $\omega_r' = \omega_r - \kappa^{Im} = \omega_r + \delta\omega$, where $\kappa^{Im} = \delta\omega$ is the shift of the resonance frequency. We obtain:

$$S_{21} = 1 - \frac{\kappa^{Re} - i\delta\omega}{(\kappa^{Re} + \epsilon) + i(\omega - \omega_r')} \tag{6.8}$$

The total quality factor of a resonance, Q_l, is given by x_0/γ, comparing the above expression to the Lorentzian (equation 6.6) yields:

$$Q_l = \frac{\omega_r'}{2(\kappa^{Re} + \epsilon)} \tag{6.9}$$

A quality factor generally gives the losses per cycle compared to the stored energy [20], [21]:

$$Q = 2\pi \frac{\text{average energy stored in resonator}}{\text{energy dissipated per cycle}} \tag{6.10}$$

$$= \omega \frac{\text{total energy stored in resonator}}{\text{total power dissipated}} \tag{6.11}$$

Loss mechanisms will be discussed in chapter 6.3.

The total quality factor can be split in two parts, the internal quality factor Q_i and the coupling quality factor Q_c, related to the internal and coupling losses. It is explicitly remarked here, that the real part of the coupling quality factor, Q_c^{Re}, is discussed. It will be clear later, when the final model is obtained, that Q_c is a complex number. The quality factors relate like this:

$$\frac{1}{Q_l} = \frac{1}{Q_c^{Re}} + \frac{1}{Q_i} \tag{6.12}$$

As the dissipation was only introduced as ϵ, it is reasonable to split the total quality factor, given in equation 6.9, in two parts:

$$\frac{1}{Q_l} = \frac{2\kappa^{Re}}{\omega_r'} + \frac{2\epsilon}{\omega_r'} \tag{6.13}$$

Coming back to the S_{21} parameter we end up with:

$$S_{21} = 1 - \frac{\frac{\omega_r'}{2Q_c^{Re}} - i\delta\omega}{(\frac{\omega_r'}{2Q_c^{Re}} + \frac{\omega_r'}{2Q_i}) + i(\omega - \omega_r')} \tag{6.14}$$

This equation can be simplified to the final expression:

$$S_{21} = 1 - \frac{Q_l/Q_c}{1 + 2iQ_l\frac{\omega - \omega_r'}{\omega_r'}} \tag{6.15}$$

Here Q_c describes a complex number, which relates to the earlier Q_c^{Re} by:

$$\frac{1}{Q_c^{Re}} = \mathrm{Re}\left(\frac{1}{Q_c}\right) = \frac{1}{|Q_c|}e^{i\phi_0} \tag{6.16}$$

ϕ_0 is the impedance mismatch between Z_1 and Z_2 of the transmission line, which will become clearer in a later section. $\delta\omega$ only depends on the imaginary part of $1/Q_c$, which was used for the simplification from equation 6.14 to 6.15.
It might seem not entirely intuitive that the real part of the coupling quality factor, Q_c^{Re}, is greater than Q_c. The reason for that is that the physical quantity is κ^{Re}, which is inversely related to Q_c, as seen above:

$$\kappa^{Re} = \frac{\omega_r'}{2Q_c^{Re}}$$

Thus the real part of κ, is smaller than the complex κ, which makes the opposite true for Q_c.

6.2 Resonator in reflection configuration

In the reflection configuration only a single port is required and S_{11} is measured. The signal propagates back through the same transmission line, therefore no impedance mismatch arises, except at the resonator. The layout is sketched in figure 6.2, in (a) with arbitrary impedances, where Z_1 is the transmission line and Z_2 depicts the resonator. In 6.2(b) the reflection configuration with specific elements is shown, the measured resonator remains the same, as in the notch configuration.

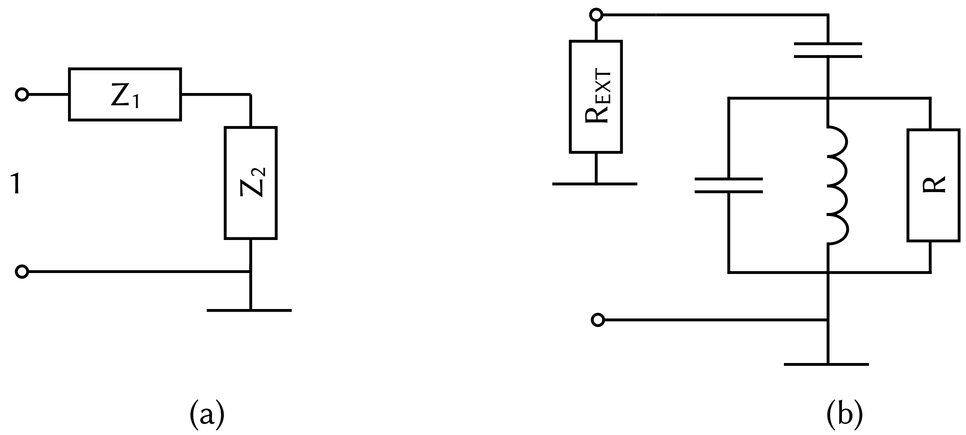

Figure 6.2: Resonator coupled to a transmission line in reflection configuration. (a) Circuit with generic impedances, Z_1 depicts the transmission line, while Z_2 is the resonator. (b) The same circuit shown using specific circuit elements.

Equation (2.16) from [22] describes an ideal resonator in reflection configuration:

$$S_{11} = \frac{\alpha_{out}(\omega)}{\alpha_{in}(\omega)} = \frac{(\kappa_c - \kappa_i) + 2i(\omega - \omega_r)}{(\kappa_c + \kappa_i) - 2i(\omega - \omega_r)} \tag{6.17}$$

$\alpha_{out,in}$ are the output and input signals. κ relates to the quality factors similar to the previous derivation, κ_c to the coupling quality factor and κ_i to the internal one. ω_r is

the resonance frequency.
Replacing the κ's by the quality factors and using

$$\frac{1}{Q_i} = \frac{Q_c - Q_l}{Q_c Q_l} \tag{6.18}$$

we obtain:

$$S_{11} = \frac{2Q_l/Q_c}{1 - 2iQ_l \frac{\omega-\omega_r}{\omega_r}} - 1 \tag{6.19}$$

As there is no impedance mismatch, $\phi_0 = 0$, therefore Q_c is real. Furthermore $\delta\omega = 0$, thus $\omega_r = \omega_r'$.
Some measurements are performed using a directional coupler. S_{21} is measured, but the direct path for the signal is highly attenuated such that it becomes practically a reflection measurement. However, there is a different path for the input and for the output from the resonator. Especially in the coupler itself a mismatch between the input and the output path exists, leading to an impedance mismatch when S_{21} is measured. Therefore, the model describing a measurement with a directional coupler is up to a complex Q_c the same as for the case of reflection. Thus the model given in equation 6.19 has to be extended by a complex Q_c to describe the impedance mismatch.

6.3 Loss mechanisms

6.3.1 Describing loss

The main source of the following considerations was [20].
The quality factor gives information about the losses of a resonator. It is calculated by [20]:

$$Q = \left.\frac{1}{Z_0 \mathrm{Re} Y}\right|_{\omega=\omega_r} \tag{6.20}$$

Z_0 is the characteristic impedance of the resonator, and $\mathrm{Re}Y$ the real part of the admittance $1/Z$ at resonance. For an existing circuit model this can be calculated. Doing some re-arranging and identifying that on resonance $\mathrm{Re}Y = 1/R$, we find [21]:

$$Q = \omega_r RC \tag{6.21}$$

C is the capacitance of the resonator and R the resistance.
The characteristic impedance can be expressed the following way:

$$Z_0 = \left.\frac{2}{\omega\left(\frac{\partial}{\partial\omega}\mathrm{Im}Y\right)}\right|_{\omega=\omega_r} \tag{6.22}$$

With this, equation 6.20 can be re-written as:

$$Q = \left.\frac{2\omega\left(\frac{\partial}{\partial\omega}\mathrm{Im}Y\right)}{\mathrm{Re}Y}\right|_{\omega=\omega_r} \tag{6.23}$$

Several mechanisms, Γ_n, contribute to the losses. The total loss is the sum of these contributions,

$$\Gamma_{tot} = \sum_n \Gamma_n.$$

Thus the quality factor can be written as [20]:

$$\frac{1}{Q} = \sum_n \frac{1}{Q_n} = \frac{1}{\omega E_{tot}} \sum_n \Gamma_n \tag{6.24}$$

It is useful to consider on the one hand, how lossy a certain mechanism is itself, and on the other hand the sensitivity to this mechanism. A useful measure for the sensitivity is the so called participation ratio, p_n. It relates the total energy in the resonator to the part of the energy, sensitive to this loss mechanism:

$$p_n = \frac{\text{Amount of energy sensitive to loss mechanism}}{\text{Total energy stored}} \tag{6.25}$$

So in case the participation is close to 1, the system is particularly sensitive to this loss mechanism.
The loss tangent is given by $\tan\delta_n$ and expresses, how lossy a certain mechanism is. Combining it with the participation ratio leads to the quality factor:

$$Q_n = \frac{1}{p_n \tan\delta_n} \tag{6.26}$$

The participation is more a geometric effect. It gives information how much energy is stored in a lossy volume, compared to the energy stored in total volume. It is dependent on the geometric circuit design and can be modified, by a different circuit layout [20]. The loss tangent is an intrinsic property of a certain medium and cannot be modified without changing the material.
There are many different loss mechanisms and in the first step we typically distinguish between external and internal losses. These are also the ones expressed by the previously derived quality factors for the notch and reflection configuration. The internal losses arise from the resonator itself, thus they cannot be varied by using a different setup. This is in contrast to the external losses, which depend on the coupling between the resonator and the transmission line. So Q_c can be modified with a different setup, by changing the coupling between the resonator and the transmission line. We distinguish between three different regimes depending on the ratio between Q_c and Q_i, which are listed in table 6.1. As the losses are inversely proportional to the quality factors, a resonator is

$Q_c \approx Q_i$	critically coupled
$Q_c >> Q_i$	under-coupled
$Q_i >> Q_c$	over-coupled

Table 6.1: Different coupling regimes

under-coupled in case the majority of the losses happen internally and over-coupled if it mainly loses to the transmission line. Consequently a resonator's lifetime is generally limited by the lower quality factor. In case losses to both mechanisms happen at a similar rate, the system is said to be critically coupled.

6.3.2 External loss

To obtain the external (or coupling) quality factor using equation 6.20, the external part of the admittance, $\mathrm{Re}(Y_{ext})$ has to be computed.

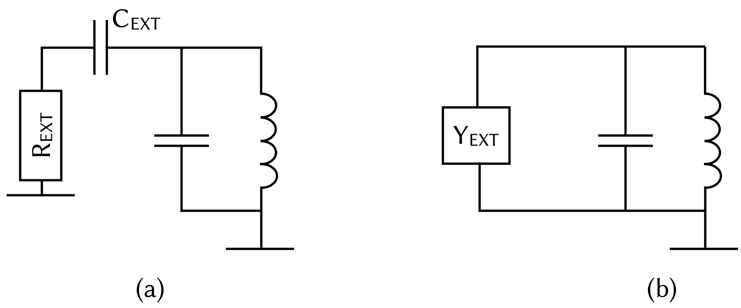

Figure 6.3: (a) Circuit model where coupling of the LC resonator to a transmission line is sketched, illustrated with specific elements. (b) Coupling combined to parallel admittance Y_{EXT}.

Following [20], we assume that an LC oscillator is coupled to the transmission line, depicted in figure 6.3. Y_{ext} combines the coupling capacitor and the resistance of the readout circuit, which leads to the following relation:

$$Y_{ext} = \frac{1}{R_{ext} + 1/i\omega C_{ext}} \tag{6.27}$$

In case of a weak coupling, where ($\omega C_{ext} << R_{ext}$), Y_{ext} can be approximated to:

$$Y_{ext} \approx i\omega C_{ext} + \omega^2 C_{ext}^2 R_{ext} \tag{6.28}$$

Using this equation leads to a total admittance for the whole circuit, with L being the inductance of the resonator:

$$\begin{aligned} Y_{tot} &= \frac{1}{i\omega L} + i\omega C + i\omega C_{ext} + \omega^2 R_{ext} &(6.29)\\ &= \frac{1}{i\omega L} + i\omega C_{tot} + \omega^2 R_{ext} &(6.30)\end{aligned}$$

C_{tot} has to be used for the resonance frequency, $\omega_r = 1/\sqrt{LC_{tot}}$, and the characteristic impedance, which then becomes $Z_0 = \sqrt{L/C_{tot}}$.
The coupling quality factor is then given by:

$$Q_c = \frac{1}{\omega_r^2 C_{ext}^2 R_{ext} Z_0} \tag{6.31}$$

6.3.3 Internal loss

There are several internal loss mechanisms which will be discussed briefly. A more detailed description is given in [20], which is also the main source for the following considerations.
On resonance the circuit stores its energy equally in the magnetic and in the electric field. The energy stored in the electric field leads to dielectric losses. These losses occur in substrates, which are used for holding artificial atoms or similar structures and store electric energy. They also appear in oxide layers, which can form on the surface of the metals and have a thickness of a few nm [23]. To find an estimation for this loss mechanism, the electric field stored in these dielectrics is compared to the total electric field (illustrate in figure 6.4). This leads to a participation ratio. In the sketch, the light gray

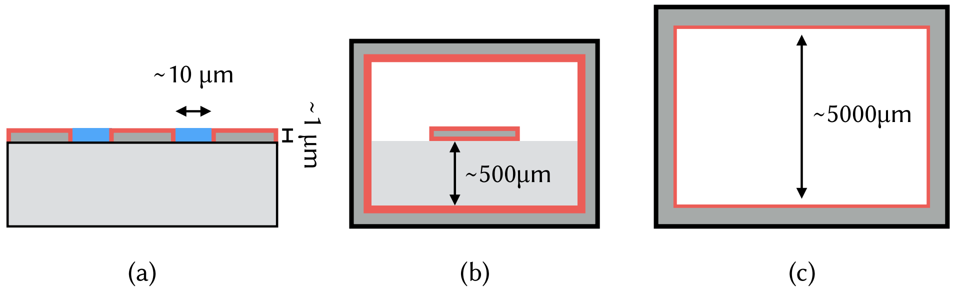

Figure 6.4: Sketches of different resonator layouts and their approximate dimensions. Quantities related to the loss, like the thickness of the oxide layer are in the range of a few nm. (a) Planar resonator, the distance between the two conductors is in the range of 10 μm, with a height of 1 μm. The effective volume is highlighted in blue. (b) Stripline on top of a dielectric substrate, around 0.5 mm from the conductor. (c) 3D cavity, dimensions in the range of cm. The higher the volume to surface ratio, the lower the participation ratio and thus the lower the losses. This points out the advantages of 3D structures. In (a) participation ratios below 10^{-2} are expected, in (b) 10^{-4} and in (c) below 10^{-6}. The dielectrics are sketched in light gray, the metal surfaces in red.

area depicts dielectrics, the areas contributing to losses are colored red. The effective volume is highlighted in blue (a), or in case of (b) and (c) it is the volume inside the structure.
Thus a participation ratio can be obtained, which leads in combination with the loss tangent to the quality factor. The loss tangent for crystalline sapphire is for example 10^{-6} [20].
Moving from 2D structures, similar to the one illustrated in figure 6.4(a), to 3D structures, illustrated in (c), can lead to participation ratios, which are several magnitudes lower. A further advantage of a 3D cavity, next to the large volume, is the mode shape itself, discussed in chapter 6.5.1. The electric field of the fundamental mode vanishes at the walls, which prevents dielectric losses and can lead to high quality factors.
The magnetic field leads to a current, which is related to conductive losses. Conductor losses are only a dominating loss source in case of normal conducting metals. The participation ratio can be found comparing the magnetic leading to a wall current to the total magnetic field, in combination with the resistance of the conductor. In case of superconductors, they only play a minor role in comparison to the other loss mechanisms.
Another loss mechanism is the contact resistance. Most important for us, it occurs at the seams of cavities, as they are typically bolted together. In there power is dissipated, due to the current across the seam. The current across the seam can be estimated by the magnetic field component along the seam. To obtain the participation ratio, the energy of the total magnetic field is compared to this. Combining this with the limited conductance across the seam leads to the quality factor.

6.4 The circle fit

After discussing the parameters characterising a resonator, these parameters have to be extracted from the measurement data. To do this the circle fit was implemented.

	Notch	Reflection
off resonant $\lvert f - f_r \rvert >> 0$	$S_{21} \rightarrow 1$	$S_{11} \rightarrow -1$
on resonance $f = f_r$	$S_{21} \rightarrow 1 - Q_l/\lvert Q_c \rvert$	$S_{11} \rightarrow 2Q_l/Q_c - 1$

Table 6.2: Extreme cases for notch and reflection configuration in the complex plane.

6.4.1 Ideal resonator in notch configuration and reflection configuration

To get the parameters in notch and reflection configuration the circle fit was developed. At first an ideal resonator without the environment, which will be added at a later point, will be discussed.
The resonance of both configurations forms a circle in the complex plane, with similar properties, given in equations 6.15 and 6.19, respectively. To avoid confusion between ω_r' and ω_r, from here on the resonance frequency will be labelled f_r and the probe frequency f.

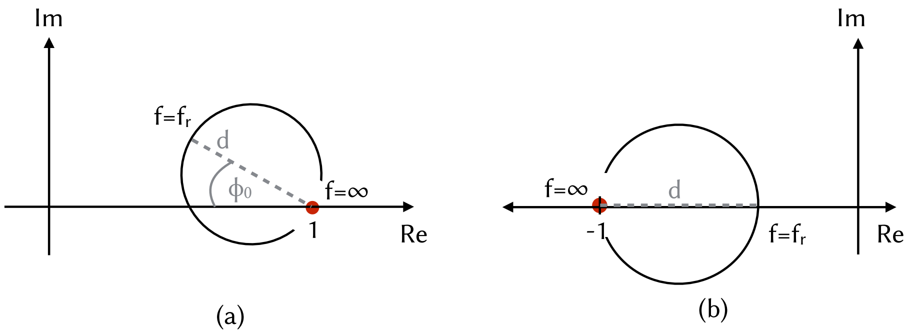

Figure 6.5: (a) $S_{21}(f)$ parameter of an ideal resonator in notch configuration in the complex plane. (b) $S_{11}(f)$ parameter of an ideal resonator in reflection configuration in the complex plane. The off resonant point, for both configurations marked with a red dot, occurs at +1 in case of notch and −1 in case of reflection. The resonance is opposite to the off resonant point, due to the π phase shift. For the notch configuration the additional impedance mismatch can be seen, rotating the circle about ϕ_0.

In figure 6.5 the resonance is shown for both configurations. For the notch configuration (a), it is seen that the impedance mismatch rotates the circle around the off resonant point of the real axis. To get intuition for the model, it is helpful to check the extreme cases, being on resonance or far away from the resonance frequency. This is stated in table 6.2. It is seen, that the diameter of the circle gives the relation between Q_l and Q_c. So in reflection configuration it is sufficient to know Q_l and the radius to gain information about the quality factors. In case of the notch configuration, as Q_c^{Re} is physically relevant, the impedance mismatch has to be known additionally. However, in case we know the circle, we also know the impedance mismatch ϕ_0. Q_c^{Re} then follows from:

$$Q_c^{Re} = \frac{Q_c}{\cos \phi_0} \tag{6.32}$$

In figure 6.6 the circle for different coupling regimes is plotted. The fraction between 1

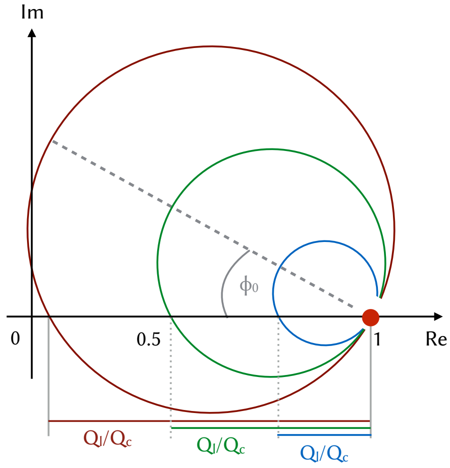

Figure 6.6: Circle for different coupling regimes in case of the notch configuration. All have the same impedance mismatch, ϕ_0, for simplicity. The fraction between 1 and the intersection of the circle with the real axis gives Q_l/Q_c, the remaining part to the origin Q_l/Q_i. The blue circle depicts an under-coupled setup, the green circle a setup, which is critically coupled, the red circle an over-coupled setup.

and the circle crossing the real axis gives the ratio Q_l/Q_c. The remaining part from the intersection to the origin gives Q_l/Q_i. In case the setup is critically coupled, the circle intersects with the real axis at 0.5. In case the intersection happens closer to the origin, the system is over-coupled. In case the intersection is closer to 1, the system is under-coupled. The circle fit works best for a critically coupled system. The circle cannot cross the origin, as in that case Q_c would be greater than Q_l, which is physically not possible. The circle can cross the imaginary axis (below or above the origin), which is illustrated in the sketch (red configuration). The reason is, that for any impedance mismatch ϕ_0, any coupling is possible. So also a configuration, in which the circle crosses the imaginary axis.
In the reflection configuration the off resonant point is at -1 and there is no impedance mismatch. The resonator is coupled critically, for a circle crossing at the origin. In case it is over-coupled, the radius of the circle increases. The maximum, where only coupling losses exist, would be at $+1$.
The discussions in the next sections will be based on the notch configuration, as it is the more complex one. The steps in the reflection configuration are similar, differences will be given in chapter 6.4.4.

6.4.2 Adding the environment

The considerations in this and the next section are based on [24] and [25].
So far the model of the ideal resonator was discussed, not taking external effects like an additional attenuation, a phase shift and the cable delay into account. Considering these we arrive at the following model:

$$S_{21}(f) = (ae^{i\alpha}e^{-2\pi i f\tau})S_{21}^{ideal}(f), \tag{6.33}$$

where S_{21}^{ideal} is the ideal model, discussed until now. a and α describe the additional attenuation and phase shift, τ the cable delay. These effects are sketched in figure 6.7 and discussed below.

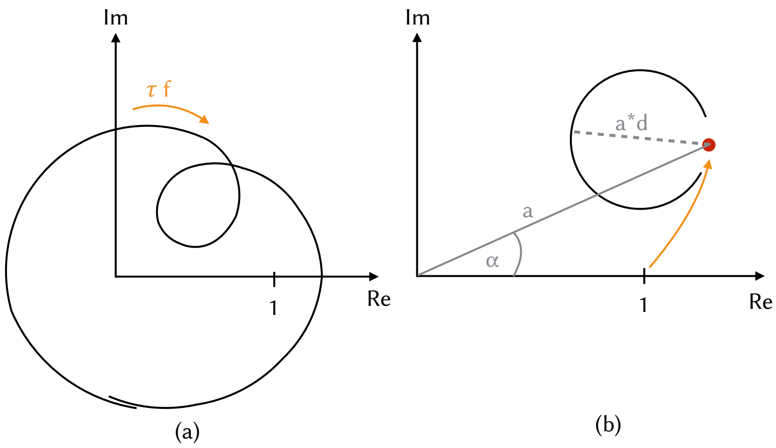

Figure 6.7: Adding the environment. (a) The effect of the cable delay is shown. It adds a linear dependency between the phase and frequency, leading to an effect shown in the plot. (b) Effects of the additional attenuation and the phase shift, after the delay is already subtracted. The circle is rotated by α and its diameter increases by a. The effects can be best seen at the off resonant point, as it is at +1 for the ideal resonator.

Effects of the cable delay

Due to the cable delay the phase of the complex S parameters increases linearly with frequency. The path the signal has to take, when a measurement is performed, is the same for the whole measurement. The frequency is swept during the measurement and so is the wavelength. This leads to a linear dependency between the phase and the frequency, called the cable delay. The effect in the complex plane is sketched in figure 6.7(a).

Effects of additional attenuation and phase shift

The effects of the attenuation and phase shift, represented by a and α in the above equation, can be best seen at the off resonant point. It should be ideally free of any effects arising from the resonator. So it just shifts and rotates the entire circle, as there is no frequency dependence, which is depicted in figure 6.7(b). As imposed by the model, the off resonant point is at +1 on the real axis, a and α can be evaluated combining this information with the measurement data.
As it is an overall gain, the circle diameter increases by the factor a.

Ideally, this model would be fitted to the measured data. The paramaters could be obtained and all the desired information gained. However, doing this would be not as robust as required and would critically depend on adequate initial parameters. As in a typical case the initial parameters are not known to the requested extent, it is not possible to fit the model within one attempt. Hence the fitting routine is divided into several sub routines with a small number of free parameters, such that robustness of the overall fit is guaranteed. The detailed steps of the fitting routine are described in the following chapter. The code used in [24] was used as a basis and then modified and improved.

6.4.3 Steps of the fitting routine

The steps which are taken are shown in figure 6.8

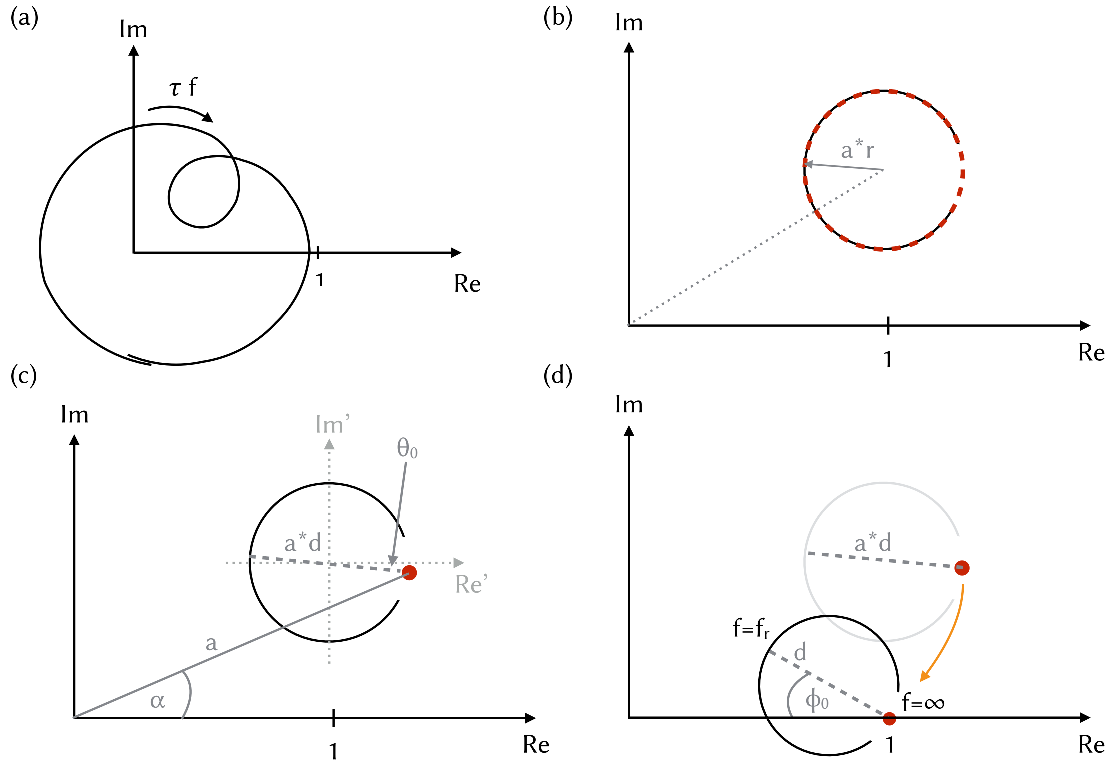

Figure 6.8: Steps which are taken to subtract the environment. The details are explained in the text.

Subtraction of the background

In the first step, the linear background of the amplitude is subtracted, which is useful in case the resonator sits on a slope of the transmission line amplitude. This step is not part of the circle fit itself, however it is supposed to lead to a more robust fitting routine.

Subtraction of the delay

In the first step of the circle fit routine, the delay is subtracted. The effect on the circle is seen in (a) to (b) in figure 6.8. (a) illustrates a measurement, before any step of the fitting routine is carried out. The delay is given as the slope of a linear fit to the phase. The phase before and after the delay subtraction is sketched in figure 6.9. At this point it is already possible to fit a circle, sketched with the dotted line in figure 6.8 (b). This gives the radius and the center point of the not yet normalised circle. To fit the circle, an algebraic fit is used, so no initial parameters are needed and the problem is reduced to an eigenvalue problem, where the smallest not zero eigenvalue yields the solution.

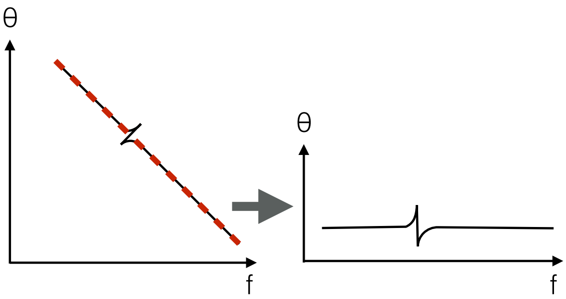

Figure 6.9: Left: Phase versus frequency before subtraction of delay. The linear dependency between frequency and phase is sketched. The resonance is, where the abrupt phase shift occurs. Linear fit (red dashed line) to identify and subtract the delay. Right: Phase after delay subtraction. No dependence on phase versus frequency, except for the resonance.

Intermezzo - to get the off resonant point

After the circle is fitted, the off resonant point has to be found. To achieve this, the origin of the complex plane is shifted to the center of the circle (figure 6.8 (c), dotted coordinate system). Afterwards the following function [25] is fitted to the phase of the centered circle. A sketch can be seen in figure 6.10:

$$\theta(f) = -\theta_0 + 2\arctan\left(2Q_l\left(1 - \frac{f}{f_r}\right)\right) \tag{6.34}$$

In the above equation θ_0 is the argument of the resonant point. f_r, Q_l and θ_0 are obtained from the fit. f_r and Q_l found from this fit are not used further on, as they are very sensitive to small variations of the measured data, and therefore to noise. They are obtained by a fit to the magnitude.
The resonant point is opposite, or π in phase, to the off resonant point. So knowing θ_0 also gives the argument of the off resonant point in the dotted coordinate system. The product $a \cdot r$ is the radius of the circle at this point, which is known from the circle fit, done in figure 6.8(b). Knowing the shift of the coordinate system (center of the circle), the radius of the circle, and the argument of the off resonant point, its absolute position can be found. Thus a and α (see (c)), which give the absolute position of the off resonant point, are obtained.

Normalisation using a and α

In this step the final parts of the environment being a and α are subtracted, see figure 6.8(d). What is left is the ideal resonator described in equation 6.15. Thus it is not required to fit the circle again, as this was already done previously. It only needs to be normalised to the radius r by dividing with the attenuation a.
With the normalised circle, ϕ_0 can be found using:

$$\phi_0 = \arcsin\left(\frac{y_c}{r}\right), \tag{6.35}$$

where y_c denotes the y coordinate of the center point of the circle.

Fit magnitude to get Q_l and f_r

Practically Q_l and f_r could be obtained from the phase fit, described in equation 6.34. As the width of the resonance, being the lifetime of a resonator, can be seen in

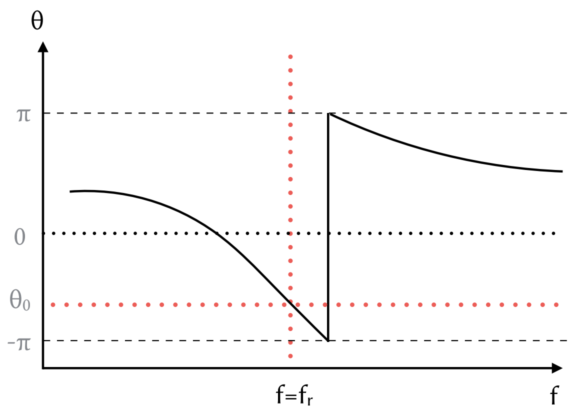

Figure 6.10: Phase versus frequency of the circle translated to the origin. f_r and $\theta = 0$ are obtained by fitting equation 6.34. $\theta = 0$ is the phase of the resonant point, indicated in the plot.

the phase and is therefore related to the total quality factor. f_r can be obtained as well being the frequency at the resonant point. However, this fit is extremely sensitive to ripples in the phase, and using it the overall robustness decreases.
It could be seen that the highest stability was achieved in case the magnitude of the ideal model was fitted to the respective part of the data. There the influence from the ripples away from the resonance is minor.
It would be ideal to obtain values for Q_l and f_r with a single fit, using both the real and the imaginary part of the data. However, it is only possible to use either the magnitude or the phase. The information they contain should be equal. So there is no preferred option from an information content view. As the magnitude proved with example data to be more robust, it was preferred over the phase fit.

Obtaining Q_c and Q_i using parameters of the circle

After obtaining Q_l it is possible to calculate Q_c^{Re}, as it is related to Q_l via the real part of the diameter, such that:

$$Q_c^{Re} = \frac{Q_l}{d \cos \phi_0}, \tag{6.36}$$

where d is the diameter of the normalised circle. Q_i can be evaluated using relation 6.12. At this point the circle fit routine is complete and all values describing the measured data are known. Some further information about the error calculation, the weighting and technical details are given in chapter A of the appendix.

6.4.4 Differences in the reflection configuration

So far the fit to a resonator, measured in notch configuration was discussed. Here, fitting the model to the measurement data of a resonator in reflection configuration is discussed. The idea is the same, as both measurements are similar. Some details are different, which are discussed in this section.
The model of a resonator in reflection configuration was presented in chapter 6.2.

Adding the environment

The environment is taken care of in a similar fashion as before, the only difference is that the off resonant point is at -1, such that one obtains the following relation for the full model:

$$S_{11} = (ae^{i(\alpha-\pi)}e^{-2\pi i f\tau})S_{11}^{ideal}(f) \tag{6.37}$$

So in case that $\alpha = \pi$, there is no additional phase shift and the off resonant point is at -1, as predicted by the model. In figure 6.11 the normalisation of the circle is illustrated, the delay is already subtracted at this point. The subtraction of the delay is identical to the notch configuration.

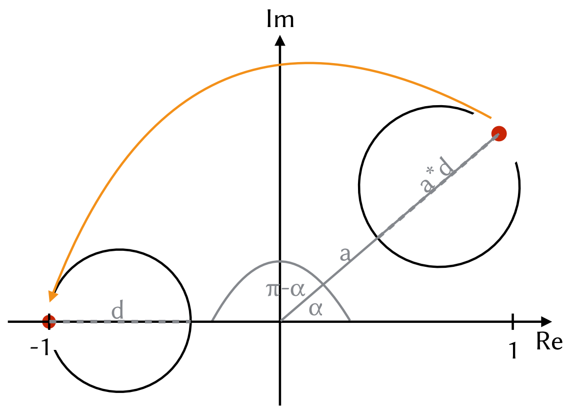

Figure 6.11: Sketch of the reflection configuration after the delay subtraction (circle upper right). Circle gets normalised and rotated such that the off resonant point is at -1 (circle on the lower left). As there is no impedance mismatch there is no additional rotation of the circle.

Differences in the fitting routine

The first two steps, described in chapter 6.4.3, where the circle is actually fit, are the same as for the notch configuration. However, as ϕ is equal to zero, it is easier to find the off resonant point. There is no additional rotation, such that the off resonant point can be immediately found, which can be seen in figure 6.5.
Afterwards Q_l and f_r are obtained similar to before with a fit to the magnitude, where naturally the model for reflection, equation 6.19, is used. Furthermore, Q_c is calculated as in the notch configuration. The only difference is the factor of 2. Q_i is obtained using the known relation 6.12.
The error calculation and the weighting, details in chapter A of the appendix, are done similarly.
To summarise, the circle fit was described, which is a fitting routine for a resonator measured in notch or reflection configuration. It fits the measured S parameter and gives information about the resonance frequency, the internal and the coupling quality factor. The advantage compared to other fits is, that the complex nature of the measured S parameter is not neglected. The magnitude, as well as the phase, is taken into account. There are seven (six in case of reflection) free parameters describing the measurement. Fitting them within one attempt would reduce the robustness of the routine. To provide overall robustness, the routine is split in several sub routines, fitting only a few parameters in each step.

The circle fit works best for a setup being in the critically coupled regime. In a regime of Q_c to Q_i being not more than 2 orders of magnitude apart, the circle fit still gives reliable results. This gives an overall working regime of 4 orders of magnitude.

6.5 Measurement of a cavity in reflection

With measurements of 3D cavities made from copper and aluminium, the circle fit was probed. A brief theoretical description of the cavity modes and the coupling to the cavity will be given. Afterwards some example measurements are shown, and the results will be discussed.
The measurements were performed by Elisa Brunori as part of her internship in summer 2016.

6.5.1 The rectangular cavity

A rectangular cavity is described similarly to a rectangular waveguide [20]. Instead of being infinitely long it is shorted with 2 planes, at a distance of c (figure 6.15). Similar to a cutoff frequency for the waveguide, resonance frequencies for a rectangular cavity are found [9]:

$$f_{mnp} = \frac{1}{2\pi\sqrt{\mu\epsilon}}\sqrt{\left(\frac{m\pi}{a}\right)^2 + \left(\frac{n\pi}{b}\right)^2 + \left(\frac{p\pi}{c}\right)^2} \tag{6.38}$$

In contrast to the waveguide, resonance frequency does not only depend on a and b, but also on c. Here the case $c > a > b$ is considered. m, n, p are integers, with $m, n \geq 0$ and $p \geq 1$. m and n cannot be simultaneously 0, which is seen in the equations describing the fields. So the fundamental resonance is the TE_{101} mode, which only depends on the two longer sides. The resonance frequency and mode shape of the TE_{101} mode does not depen on which of the two sides is longer. It is given by:

$$f_{101} = \frac{1}{2\pi\sqrt{\mu\epsilon}}\sqrt{\left(\frac{\pi}{a}\right)^2 + \left(\frac{\pi}{c}\right)^2} \tag{6.39}$$

The shape of the mode can be obtained using equations 3.21 and 3.22, which describe the rectangular waveguide, where E_x is found to zero. The component of the electric field is sinusoidal in the y direction:

$$E_y \propto \sin\frac{\pi x}{a} e^{-i\beta z} \tag{6.40}$$

Also the z dependence can be re-written to a sine function, similar to the x dependence of E_y. The magnetic field has similar components in the x and z direction, and vanishes in the y direction.
A picture of the copper cavity is shown in figure 6.12. The two halves are bolted together. The next step to consider is the coupling to the cavity, which is done by the SMA flanges seen on top.

Figure 6.12: Picture of a cavity, the two halves are bolted together. The SMA flanges on top are required to connect the cavity to the outside.

6.5.2 Coupling to the cavity

To couple into the cavity, cylindrical copper pins are used, which are plugged into SMA connectors and connected through a coaxial cable to the signal source.
The cavity walls have cylindrical holes to insert the pin, which makes the wave propagate similarly to a circular waveguide. The wave propagation on and after the pin is sketched in figure 6.13. In the first part two conductors, the pin and the wall, are present,

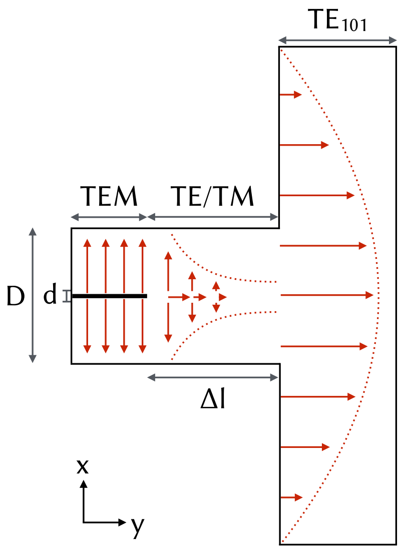

Figure 6.13: Sketch of coupling between the pin and the cavity. The different regimes of wave types are discussed in the text. Similar to [20], figure 4.7.

which allow TEM waves to propagate. After the pin ends, only a single conductor, the wall, is present and the situation is the same as in a circular waveguide. The frequencies in our case are below 10 GHz, while the diameter of the hole is around 3.5 mm (table 6.3). The cutoff for the cylindrical holes with this diameter is around 35 GHz. So the excitation happens below cutoff of the pin holes. Therefore the field is exponentially attenuated. The fraction of the wave, which makes it into the cavity, excites it then.
In addition the SMA connector has an impedance of 50 Ω. To avoid reflections, the ratio

of the diameter of the hole to the pin diameter should be such that it continues with 50 Ω. The characteristic impedance of a coaxial cable is expressed with [26]:

$$Z = \frac{1}{2\pi}\sqrt{\frac{\mu}{\epsilon}}\log\left(\frac{D}{d}\right) \tag{6.41}$$

μ and ϵ are the material properties of the dielectric in between the conductors. In the present case of vacuum, $\sqrt{\mu/\epsilon}$ reduces to the vacuum impedance of $\eta = 377\,\Omega$. Calculating the impedance, using equation 6.41 and the given dimensions, table 6.3), results in 51(4) Ω. So the 50 Ω from the SMA connector are continued.
Due to the exponential attenuation of the signal, the shorter the pin is, the weaker the coupling. This should be seen in the coupling quality factor. So for the pin not reaching into the cavity, which is in case Δl being negative, we expect an exponential relation between the pin length and Q_c.
There is also the case, that the pin reaches into the cavity. Thus TEM waves are present throughout the hole and besides losses no attenuation is expected. The excitation should then in a first approximation scale linearly with the fraction of the pin length inside the cavity, as the mean electric field strength is the same all over the pin on average.
This transition is smooth and with a pin barely reaching into the cavity, the coupling can be described by the exponential attenuation with the pin length until a certain point is reached. This point is expected to in the same range as the pin hole radius.

6.5.3 Experimental setup

The measurements are performed using a vector network analyser (VNA). It can measure complex S parameters versus frequency ranging from 300 kHz to 18 GHz.

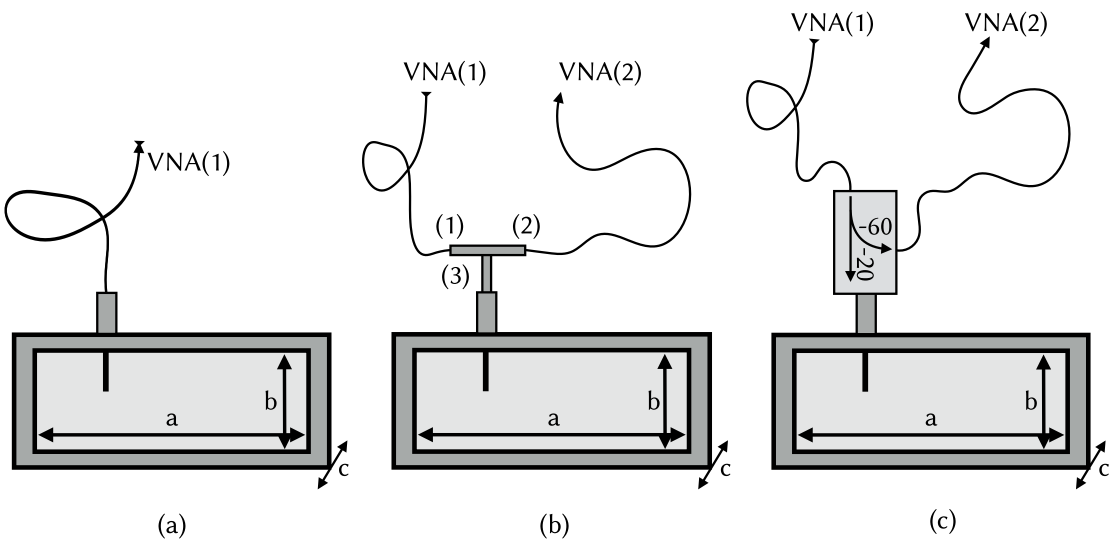

Figure 6.14: Different setups to measure a microwave cavity in reflection. In (a) the reflection configuration is sketched, in (b) the setup with the T-connector and in (c) the directional coupler setup. VNA(1) and (2) are the ports of the VNA.

Different options exist to measure a cavity in reflection configuration. It is possible to

measure directly the S_{11} using the VNA. Such a setup is sketched in figure 6.14(a). The main concern with this setup is that this is not possible in our cryostat. The reason is that the microwave lines used for the input cannot be used for the output. Therefore different lines have to be used, which makes a reflection measurement impossible. This can be circumvented by using a T-connector, sketched in figure 6.14(b). A T-connector is a part connecting three cables together, having the standard impedance of 50Ω for each port. Two of these cables are connected with port 1 and 2 of the VNA, the third port connects to the cavity. Thus it is possible to measure a cavity in reflection by performing a S_{21} measurement. A part of the signal coming from the VNA, port 1 in case of S_{21}, goes into the cavity, while the other part continues to the second port of the VNA. The signal coming from the cavity sees two options, (1) or (2) of the T-connector. The part continuing to (2) goes to the VNA port 2 and is subsequently measured. This configuration is of notch type, so the part of the signal directly continuing to the second port of the VNA is required within the model. The signal coming from the cavity faces two ports, both with 50Ω, which makes the effective impedance it sees lower, which leads to an impedance mismatch.
To circumvent this behaviour, a directional coupler (figure 6.14) was used. A S_{21} measurement is performed, but the direct path is strongly suppressed, which practically makes it a reflection measurement.

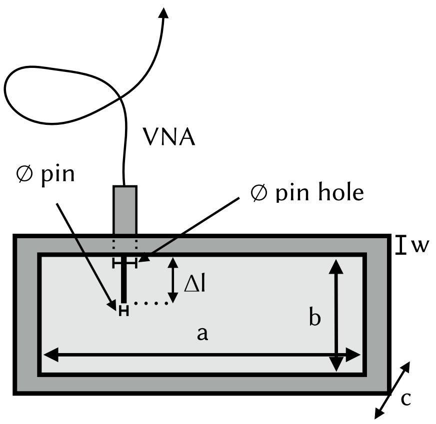

Figure 6.15: Sketch of the cavity with the dimensions listed in table 6.3. Δl is the effective pin length, w the effective width of the wall on top (wall thickness at the SMA connector). The pin hole continues outer the diameter from the SMA, the pin itself the diameter of the inner SMA conductor to avoid an impedance change and keep reflections to a minimum.

Two different cavities were measured, one made from copper and another one from aluminium. Their dimensions are listed in table 6.3. Such a cavity is illustrate in figure 6.15, including the dimensions.
In total six different measurement setups exist with the two different cavities and the three different methods to measure them. Pins of different lengths were used to check the previously discussed behaviour regarding the dependency with Q_c.
All of these measurements were performed under room temperature.
Using the dimensions given in table 6.3 the first resonance frequency of the cavities can be found with equation 6.39.

$$f_r^{\mathrm{Cu}} = 9.66(5)\,\mathrm{GHz}$$
$$f_r^{\mathrm{Al}} = 8.19(4)\,\mathrm{GHz}$$

	Copper	aluminium
a	21.9(1) mm	26.9(1) mm
b	9.9(1) mm	10.0(1) mm
c	22.0(2) mm	25.0(2) mm
effective wall thickness	5.84(5) mm	4.06(5) mm
pin hole diameter	3.5(2) mm	3.5(2) mm
pin diameter	1.50(5) mm	1.50(5) mm

Table 6.3: Dimensions of the measured cavities, corresponding sketch with labels in figure 6.15. Effective wall thickness corresponds to the additional length a pin has to have, to enter the cavity.

6.5.4 Simulation data

Simulations using HFSS were performed. In this case the eigenmode type was used, as the resonance of the cavity itself was of interest. The material assigned to the cavities

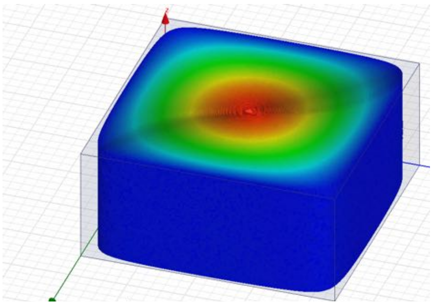

(a)

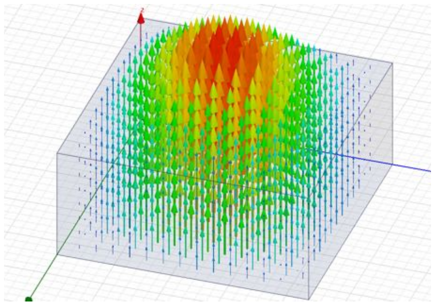

(b)

Figure 6.16: Electric field of a rectangular cavity on resonance. (a) Magnitude plot of the electric field inside the cavity. It vanishes at the walls and has a its maximum in the center. (b) Same as (a), using vectors. In both plots red corresponds to a strong field, blue to a weak field (in comparison), the scale is linear.

was vacuum, as they are empty, or filled with air. The resonance frequencies found were:

$$f_r^{\text{Cu, simulated}} = 9.66\,\text{GHz}$$

$$f_r^{\text{Al, simulated}} = 8.19\,\text{GHz}$$

These are identical to the calculated resonance frequencies. The field is plotted for a cavity with the dimensions of the aluminium one. In figure 6.16 the electric field of the cavity is plotted. In figure 6.17, the surface current and the magnetic field inside the cavity are plotted. The electric field (a,b) has its maximum in the center and vanishes on the walls. This is expected for the TE_{101} mode as given in equation 6.40. In (a) the magnitude of the field is plotted, in (b) the field is plotted with vectors. The surface current is plotted in (c) for three of the walls. It is strongest in the middle of the walls, and exactly cancels out at the center of the top wall. From the flow of the current distribution it becomes clear, why it is not possible to cut the two halves of the cavity, necessary for fabrication, parallel to the x, y plane. In (d) the magnetic field is plotted, where it can be seen that, as expected, the rotation of the magnetic field leads to the current.

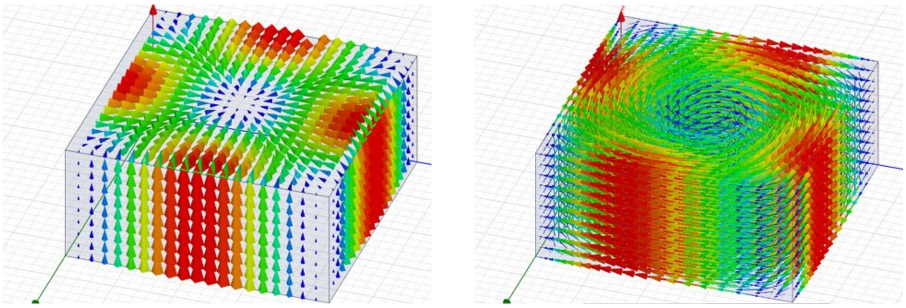

Figure 6.17: Surface current and magnetic field of a rectangular cavity on resonance. (c) Surface current plotted on three walls with a $\pi/2$ phase shift compared to the electric field. The maximum is in the middle of the wall and it exactly cancels out in the middle of the top wall. (d) Magnetic field also with a $\pi/2$ phase shift compared to the electric field. It can be seen that the rotation of the magnetic field leads to the current. In each of the plots red corresponds to a strong field, blue to a weak field (in comparison), the scale is linear.

6.5.5 Example measurement

In figure 6.18(a) a measurement of the copper cavity is shown, being in the under-coupled regime, using the T-connector. In the top left the raw measurement data and the respective fit is plotted in terms of real vs. imaginary. On the top right the absolute magnitude is shown and on the bottom left the phase. From the relatively small magnitude and phase change at the resonance, we can already obtain that this was measured in the under-coupled regime.
In the constant slope of the phase, besides the resonance, one sees the effect of the phase delay.
In the bottom right the normalised circle is shown, where the off resonant point is at +1 and all the effects of the environment are subtracted. The under-coupled regime can be recognised here as the diameter, giving the relation Q_c/Q_l, which is much smaller than 1. Therefore $Q_c >> Q_l$, so this setup is dominated by internal losses.
In addition, there is some noise in the measurement. This is here more visible than measuring over-coupled configurations. The reason is that the magnitude of the resonance is smaller, which makes the influence of the noise relatively stronger.
In figure 6.18(b) a measurement of the aluminium cavity in reflection is shown. In contrast to the other measurement the resonance is more defined, which is due to the critical coupling for this measurement. The previously seen noise cannot be recognised any more.
This is a reflection measurement, so the off resonant point, seen for the normalised circle on the bottom right, is at -1. The size of the circle indicates, that the setup is in the regime of being critically coupled.
Measurements like this were performed for all available pins, using both cavities in the three possible setups. The summarised results are discussed in the next section.

6.5.6 Results

The measurements results of the aluminium and copper cavity using the different setups (discussed in 6.5.3) with different coupling pins are discussed here. Results for Q_i

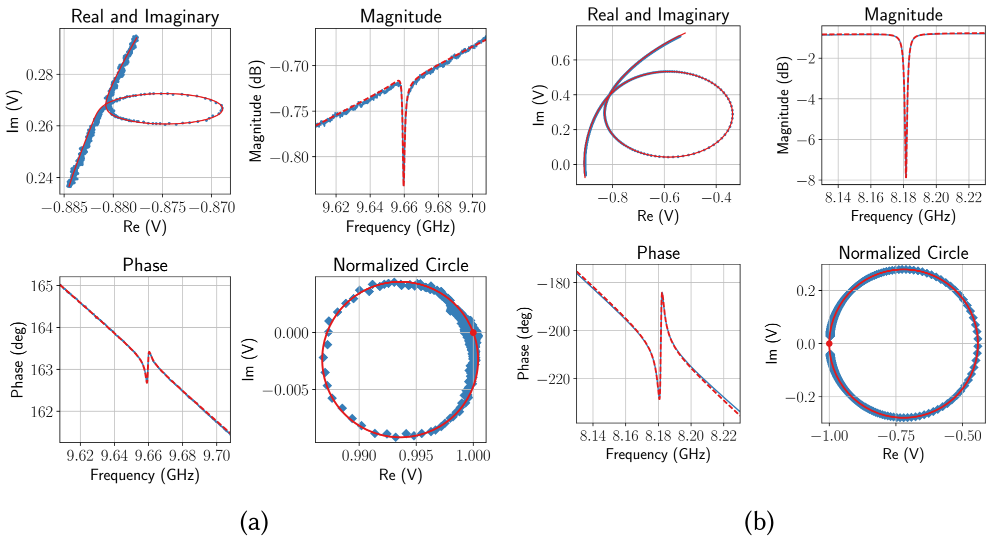

Figure 6.18: (a) Measurement of a copper cavity with the T-connector, in the under-coupled regime. Blue dots are the measurement data, red line is the fit, calculated from the parameters. The effective pin length was −1.41 mm. (b) Measurement of an aluminium cavity in reflection configuration, which is approximately critically coupled. The effective pin length was 0.44 mm. Top left: Raw measurement data with the final fit, imaginary vs. real part of the S parameter is plotted. Top right: Magnitude of the S parameter in decibel scale versus frequency. Bottom left: Phase versus frequency. The cable delay is seen and the abrupt phase change, where the resonance occurs. Bottom right: Normalised circle (after all effects from the environment are subtracted) with the circle fitted to the data.

and the resonance frequency show no (or only a minor) dependency on the pin length, and are therefore discussed briefly. The dependency between the coupling quality factor and the pin length are discussed in more detail, the expectations from theory were discussed in chapter 6.5.2.
For Q_i and the resonance frequency, f_r, only a minor correlation with the pin length is seen in the measurements. This is in line with the expectations, as the pin reaching into the cavity should barely influence the field inside the cavity. Also possible losses to the pin should be completely dominated by losses to the cavity walls. The results are combined in table 6.4. The resonance frequencies coincide with the calculated ones

	Q_i	f_r
Copper	7500(500)	9.66(2) GHz
Aluminium	4500(500)	8.18(2) GHz

Table 6.4: Measured Q_i and f_r for the cavities. The measured values had some variance, the errors give a range, in which they were found.

using equation 6.39 and also with the simulated ones. Thus the discussed model seems to apply.
The reason for the higher Q_i of the copper cavity is the better conductivity of copper at room temperature. According to [27] the specific resistance of copper at 300 K is approximately 16.6 nΩ, for aluminium it is 27.5 nΩ. This is similar to the ratio seen in the internal quality factor and therefore a possible explanation.
The results for the coupling quality factor of the copper cavity are plotted in figure 6.19,

against the effective pin length. So for the effective length 0, the pin is flush, for positive values it reaches into the cavity.
An exponential curve:

$$Q_c^{\mathrm{fit}}(l) = Ae^{-lb} \tag{6.42}$$

is fitted to the data points and plotted on top. To get an equal weighting of all data points, the logarithm of the data was fitted with a linear function. From this the exponential was calculated. This was also done for the aluminium cavity. In panel (a) of

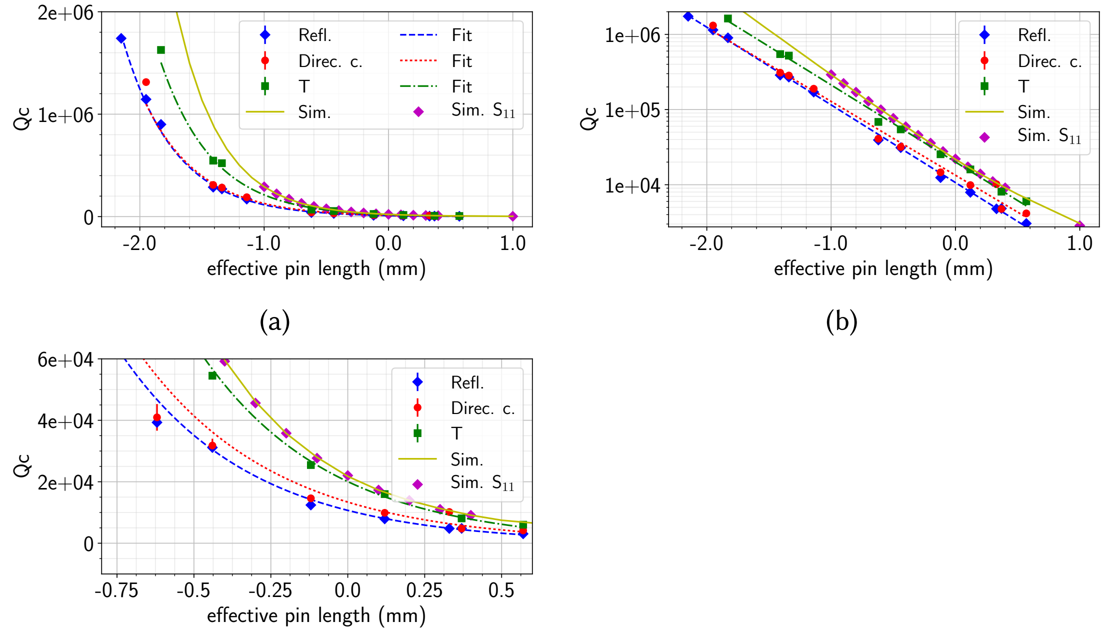

(a) (b) (c)

Figure 6.19: Coupling quality factor for different pin lengths and corresponding fit, for the copper cavity. The whole range is plotted in (a) linear scale and (b) logarithmic scale. In (c) a zoom on the lower Q's is plotted. The cavity was measured in reflection, with a T-connector and with a directional coupler. The coupling simulated with HFSS is also plotted. The two options, eigenmode and driven (labelled with S_{11}), agree. The measured data is in the same range as the simulation results. Also the slope is similar.

figure 6.19 the whole range is depicted in linear scale. The measurement data shows the expected exponential dependency. Also in the logarithmic plot (b) the exponential dependency is obtained and the fit seems to describe the data well. In (c) the low $Q's$ are shown and also these values are in good agreement with the exponential fit. This means that the exponential dependency is still given for the pin being slightly inside the cavity.
The values for the T-connector are above the others throughout the whole range of pin lengths. The reason could be the previously discussed impedance mismatch at the T-connector itself and thus a reduced coupling to the outside. Due to that impedance mismatch reflections occur between the 50 Ω SMA connector from the cavity and the T-connector. This could effectively increases the life time of the cavity, seen in a higher Q_c.
The coupling was also simulated using HFSS, this is also shown in figure 6.19. The coupler was modelled as a cylinder with a hole (representing the pin in the experimental setup), matching the dimensions of the measurement setup, giving 50 Ω. Simulations in

eigenmode were run and HFSS gives the quality factor directly in the solution data. Also driven simulations, labelled with S_{11} were run, fitting the resonance using the circle fit. The values agree with the ones obtained using eigenmode solutions. Simulations were run in steps of 0.1 mm, for both solution types. The solid line, showing the simulation data, is a straight connection of the data points. To save computation time, the driven simulations were only performed for some values of the pin length, to see if they agree, which they do. The simulated configuration with the highest Q_c (not plotted here) also shows agreement with the data from the eigenmode simulations.
The simulation data is throughout above the measurement data, but always in the same range showing a similar slope. The difference to the measurement data is within a different pin length of half a millimeter. A possible reason for the difference is that the pins were not flat at the bottom, as they were shortened using sand paper. In addition, the edges of the cavity (and sometimes the pin) are rounded, also giving an uncertainty. Within these considerations the simulated data is within the expected agreement.
For these measurements no distinction between the two ranges with the pin sticking out into the cavity or being shorter than flush was made. As discussed, the transition should be smooth, furthermore part of the pin, which sticks into the cavity, is far below the pin hole radius.
The fit parameters are given in table 6.5. The exponential constant b is, within the er-

	A	b
Reflection	1.07×10^4	2.38(3)
T-connector	$2.01(12) \times 10^4$	2.36(6)
Direc. coupler	$1.34(13) \times 10^4$	2.26(9)
Simulation	$2.41(3) \times 10^4$	2.54(3)

Table 6.5: Fit parameters with their errors for the copper cavity in the three different configurations and for the data simulated with HFSS. The model is given in equation 6.42.

rors, the same for all measured configurations. This is expected, because the data should have the same dependency on the pin length, independent on the measurement configuration. The simulated data is a bit off, but still in the same range. The offset, A, is similar for the reflection configuration and the directional coupler. This is expected, as using the directional coupler is similar to the reflection configuration. The parameter A for the T-connector is above the others, which makes sense as all the values are higher, due to the discussed impedance mismatch at the T-connector itself. Again it is a bit off for the simulated case, which was already seen in the plot, as the values from the simulation are in the whole range above the other ones.
In figure 6.20 the measurement results from the aluminium cavity are shown. The wall is thinner for this cavity, so the pins are sticking further into the cavity compared to the copper cavity. Therefore the fit was divided into two parts, the exponential part, as for the copper cavity, and from 1 mm onwards a linear fit was used:

$$Q_c^{linear}(l) = -k \cdot l + d \tag{6.43}$$

The reason to use an exponential fit until 1 mm is, that for more than 1 mm the behaviour seems to be different. It was not sure before, where exactly this transition between exponential and linear dependency would occur, only the range was known. So the best agreement with the data was the goal, which was achieved by assuming the transition

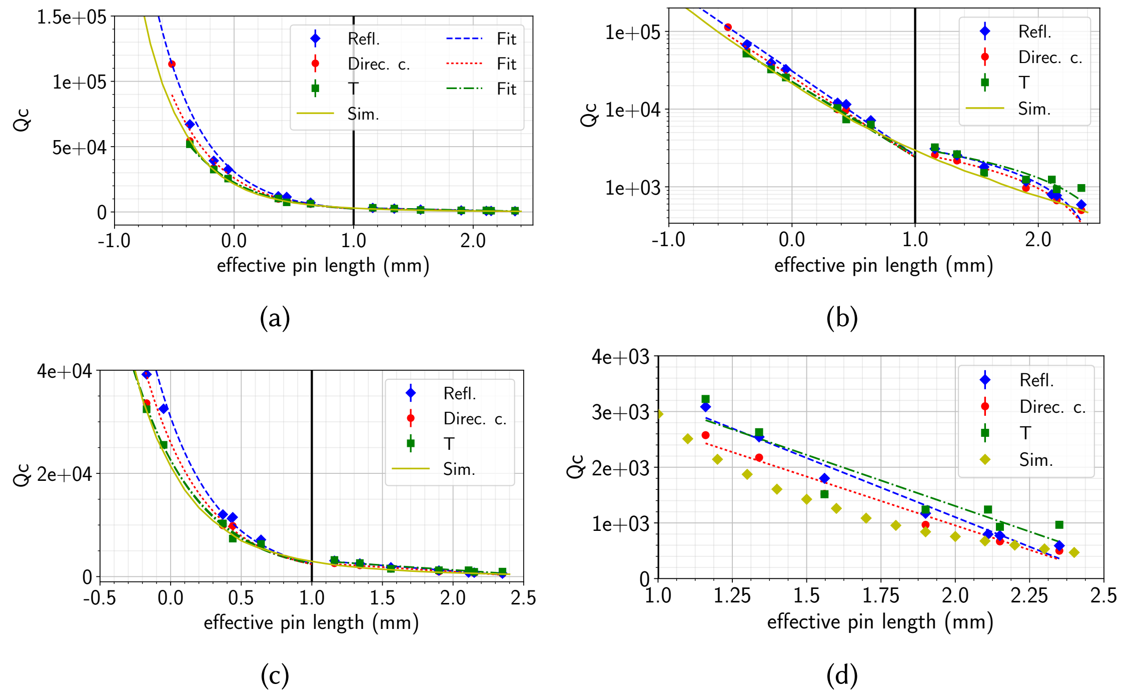

Figure 6.20: Change of coupling quality factor for different pin length and corresponding fit, for the aluminium cavity. The whole range, besides one measurement of the reflection configuration, is plotted, in (a) linear scale and (b) exponential scale. In (c) a zoom on the lower Q's is plotted. The transition to the linear dependency can be seen. In (d) the part showing an approximate linear dependence is plotted. The vertical line indicates the transition between exponential and linear fitting range. The data form HFSS is also plotted, it generally agrees with the measured results. The data was taken every 0.1 mm, except for (d), a solid line connecting them is shown. In (d) they are depicted as points.

to be around 1 mm. In figure 6.20(a) the whole range is plotted. For one measurement in the reflection configuration the shortest pin was used, leading to Q_c being a magnitude above the other measurement points, around 8×10^5. This data point is not plotted in here, but is also described by the fit. In 6.20(b) the same data is shown in a logarithmic plot. The exponential dependency can be obtained and the transition to another dependency around 1 mm is seen.

In 6.20(c) a zoomed segment is shown, and the exponential fits seem to describe the measurement points well. Some measurements showed many ripples, which caused some trouble for the fitting routine, still the values show overall agreement. The results for the T-configuration are similar to the others and not decisively higher, as it was the case in the copper configuration. The reason for this is not clear at this point.

Also in 6.20(c) the transition between the exponential and the linear part is seen. The exponential fit describes the measured values sufficiently well. The linear fit, 6.20(d), seems to be a good enough description for the points. However, especially for the T-connector it is not clear, if a linear dependence is present.

The simulation data is close to the measurement points. In this case only eigenmode simulations were run, as agreement between driven and eigenmode was seen already for the copper cavity. The exponential part has a very similar dependency on pin length compared to the fit. The linear part, already seen in 6.20(b) and more clearly seen in 6.20(d), has a different dependency. The values themselves are still very similar. Given

the different dependency no linear fit to to the simulation data was performed. Simulations were performed every 0.1 mm and except for 6.20(d) they are depicted with a solid line, connecting them. In 6.20(d) the single data points are plotted.
The fit parameters are given in table 6.6. Looking at the exponential part and comparing

	Exponential fit		Linear fit	
	A	b	k	d
Reflection	$3.09(48) \times 10^4$	2.50(13)	$2.13(22) \times 10^3$	$5.36(41) \times 10^3$
T-connector	$2.26(29) \times 10^4$	2.17(16)	$1.84(44) \times 10^3$	$4.98(81) \times 10^3$
Direc. coupler	$2.60(51) \times 10^4$	2.38(22)	$1.76(18) \times 10^3$	$4.47(34) \times 10^3$
Simulation	$2.43(7) \times 10^4$	2.53(3)		

Table 6.6: Fit parameters with their errors for the aluminium cavity in the three different configurations and for the data from the HFSS simulation. The model is given in equation 6.42.

the values to the copper cavity, they are in the same range, but the errors are higher. To some extent this is due to the inferior measurement data, leading to more variance in the obtained data. As already seen in the plot, the difference for the T-connector is not obtained any more. The values obtained from the simulations are close to the measurement, especially the exponential constant is close to the one measured in the reflection configuration.
For the linear part, the values are still within the errors, which are, especially for the case of the T-connector, big. The overall agreement tells that similar data is acquired using the different setups. The simulation data was not fit, as the values do not seem to depend linearly.
Testing the circle fit to check, if the different measurement configurations agree was a main motivation for doing these experiments. In addition, a goal was to investigate the dependency between the pin length and the coupling.
To conclude, for the copper as well as for the aluminium cavity, the values agree and it does not critically depend which measurement setup is used. Due to the higher values for the T-connector measuring the copper cavity, the directional coupler might be the better choice in case the goal is to reproduce a reflection measurement. The exponential correlation between the pin length and Q_c was obtained for a pin not sticking into the cavity. This is in agreement with the theory.
For the measurements with the pin sticking inside the cavity, which were only available for the aluminium cavity, it is not entirely clear, if a linear correlation is given. The main reason is that too few data points of poor quality exist.

Chapter 7

Stripline resonator in a 3D waveguide

U-shaped stripline resonators (SLR) made from aluminium and niobium, sitting on a silicon substrate were placed in a rectangular waveguide, to be able to analyse them. This represents a resonator in notch configuration. The assembly was put into the cryostat and cooled down to around 20 mK, to achieve superconductivity. This is required to measure them and reach high quality factors.
Different input powers, down to the single photon limit, as well as different temperatures up to about 1 K were investigated, to gain knowledge about their behaviour.

7.1 Layout

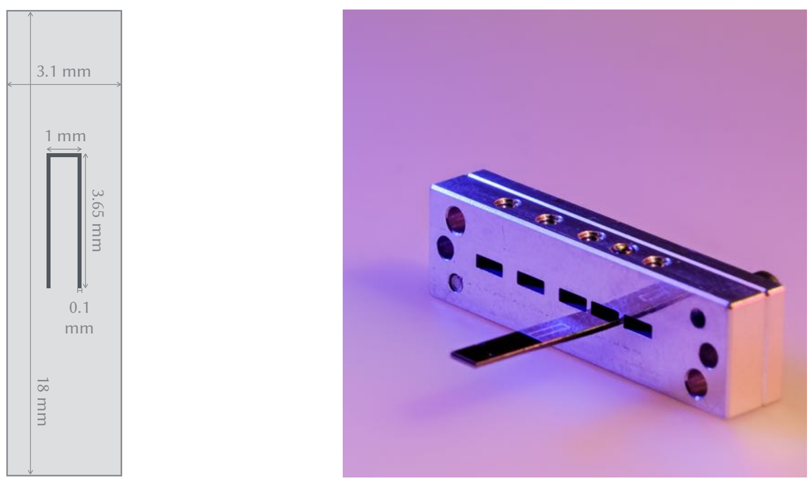

(a) (b)

Figure 7.1: (a) Sketch of the stripline resonator with a resonance frequency of around 8 GHz, sitting on a Silicon substrate. (b) Picture of a symmetric stripline, already in the sample holder, which is necessary to place the sample in the aluminium waveguide. The mounting process is explained in chapter C of the appendix.

In figure 7.1(a) the layout, including dimensions, of such a U-shaped stripline resonator is sketched. The resonance frequency is about 8 GHz. Striplines with a frequency of 7.5 GHz were also measured, having an extended leg length. In (b) a picture of the

stripline is shown, already placed in the sample holder, necessary to put it in the waveguide. The thickness of the stripline on the substrate is about 200 nm.
This stripline was placed in a rectangular waveguide in the plane of the transverse field. For the frequencies we used, only the fundamental TE_{10} has to be taken into account, as the others have a cutoff at much higher frequencies, around 13 GHz and above. A typical setup is shown in figure 7.2. In (a) a sketch, also showing the electric field shape is plotted, in (b) a picture of the waveguide with the stripline is shown. The transverse

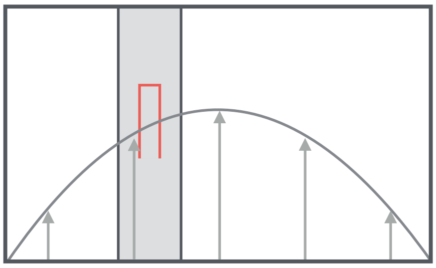

(a)

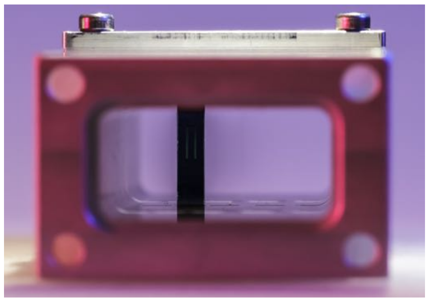

(b)

Figure 7.2: (a) Sketch of typical setup including. SLR in the waveguide, electric field gradient over the stripline. (b) Picture of the stripline in the aluminium waveguide.

field follows a sine, such that a voltage difference between the two legs arises, leading to a current. Driving the waveguide on the resonance frequency of the stripline leads to a drop in the transmitted signal, S_{21}. As stated before, the waveguide in combination with the stripline represents a resonator in notch configuration. Thus it is analysed with the circle fit, discussed in chapter 6.4.
A higher field gradient over the stripline, leads to a higher voltage difference between the two legs of the stripline, leading to a stronger coupling. Close to the walls the field gradient is the highest and therefore the coupling is the strongest. Exactly in the center, there is no gradient of the electric field, thus the stripline does not couple to the waveguide, the coupling quality factor is infinite.
The reason for the U-shape is the compact architecture with a still low resonance frequency, which depends on the overall length. The coupling to the waveguide is defined by the top section of the stripline, as the electric field difference occurs there. This part is around a factor of 20 smaller than the total width of the waveguide, allowing to place the stripline at various positions within the waveguide. This gives flexibility in the coupling to the waveguide. It is also of similar size compared to the transmon qubits, which can be advantageous, as striplines should serve as qubit readout resonators in future experiments.

7.2 Circuit model

To develop a theoretical description for the setup, the input impedance of a terminated transmission line with a load impedance Z_L (equation 2.17) was considered. A similar approach is made in [28], described in their supplementary material.
The stripline itself is modeled as a transmission line, the second conductor is the waveguide wall acting as a ground. For the occurrence of a resonance, the input impedance has to become infinite. Moreover, the voltage should have its maxima on the end of

the legs, the current is expected to have its maximum in the center. This behaviour is exactly the one of an open transmission line with a length of $\lambda/2$, plotted in figure 2.3. The difference here is, that it is not an open, as coupling between the legs takes place, due to the shape of the stripline. This leads to a finite load impedance, $Z_L \neq \infty$. In an approximation, the load is modeled as the capacitive coupling taking place at the end of the legs, leading to a shunt capacitance. This is sketched in figure 7.3. The coupling is only considered at the end of the legs. The reason is, that the highest voltage occurs there, which leads to a maximum coupling. Therefore Z_L can be replaced by the impedance of the shunt capacitance, which is $1/(i\omega C_s)$.

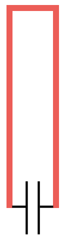

Figure 7.3: Coupling between the legs of the stripline is modeled as capacitve coupling between their ends, similar to a shunt capacitance.

Taking $Z_{in} = \infty$, which is a condition for a resonance, equation 2.17 simplifies to:

$$-\omega C_s Z_0 = \tan \beta l \tag{7.1}$$

In the above equation C_s is the shunt capacitance and Z_0 the characteristic impedance of the transmission line, given by $\sqrt{L/C}$. l is the total length of the stripline, β can be rewritten as ω/v_p (equation 2.12). The phase velocity v_p is expressed by $c/\sqrt{\epsilon_{\text{eff}}}$, where c is the speed of light and ϵ_{eff} the effective dielectric constant.
This is a transcendent equation for the resonance frequency, which has to be solved numerically. Before doing this, values for L, C, C_s and $\epsilon_{\text{eff.}}$ have to be found, which is done by using Maxwell, a software similar to HFSS for the electrostatic and magnetostatic case. Details about performing simulations with Maxwell are given in chapter B of the appendix.
The stripline is modelled in there and a magnetostatic simulation is performed, to get the characteristic inductance. To obtain a value for the characteristic capacitance, the coupling between the wall and the stripline is simulated in the electrostatic case. To get an estimate for the shunt capacitance, the middle part of the stripline, which connects the legs, is excluded and the capacitance between the legs is simulated. All of these simulations are done with the stripline on top of the silicon substrate. The effective ϵ_{eff} is obtained by comparing the capacitance between the outer wall and the stripline with and without the silicon substrate. The parameters from the simulations are stated in table 7.1. Using these parameters and solving the transcendent equation for its resonance

	L	C	Z_0	C_s	ϵ_{eff}
Maxwell simulations	5.76 nH	201.8 fF	168.9	125.6 fF	2.57

Table 7.1: Values for stripline parameters obtained from Maxwell simulations.

frequency leads to:

$$f_r = 8.27\,\text{GHz}$$

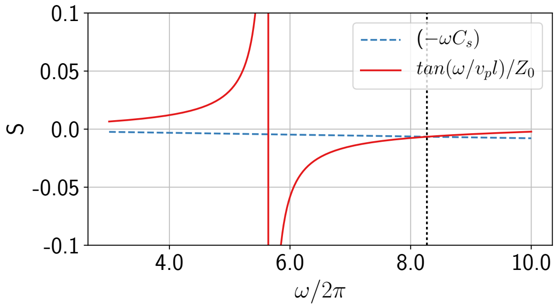

Figure 7.4: Plot of the left and the right part of equation 7.1. Their intersection gives us the solution of the transcendental equation, which is the resonance frequency, marked by the black dotted line. For the case with no shunt, the resonance frequency would be higher.

The two sides of the equation are plotted in figure 7.4, the solution is found where the two curves intersect. So the shunt capacitance leads to an effective shift to lower resonance frequencies.

7.3 Internal loss mechanisms

In chapter 6.3 external and internal loss mechanisms of a resonator were discussed in general. This theory still applies here.
In this chapter a more detailed discussion of the internal loss mechanisms of the stripline resonator is presented. The discussion is based on [21].

7.3.1 Basics

Following equation 6.21 the internal quality factor can be calculated from:

$$Q_i = \omega_r R_{int} C \tag{7.2}$$

C is the capacitance of the resonator and R_{int} the internal resistance related to the losses, which supposedly, can be written as:

$$R_{int} = \frac{Z_0}{\alpha l_s} \tag{7.3}$$

l_s is the length of the resonator, in this case of the stripline and α refers to the real part of the propagation constant γ, given in equation 2.7. Assuming that the specific losses of the transmission line G_l, R_l are small, the propagation constant can be approximated as:

$$\gamma \approx i\omega\sqrt{L_l C_l}\left(1 - \frac{i}{2}\left(\frac{R_l}{\omega L_l} + \frac{G_l}{\omega C_l}\right)\right) \tag{7.4}$$

L_l relates to the conductance per unit length, C_l to the capacitance per unit length of the resonator. Using equation 7.4 the real part of the propagation constant, α, being the attenuation, is found to:

$$\alpha \approx \frac{1}{2}\left(\frac{R_l}{Z_0} + G_l Z_0\right), \tag{7.5}$$

with Z_0 being the characteristic impedance. So two main loss mechanisms are obtained. R_l/Z_0 is related to the conductive losses, $G_l Z_0$ is related to losses to two level systems on the substrate, which the stripline sits on.

7.3.2 Conductive loss

For the probed resonators superconductivity is a requirement to achieve high quality factors. Due to the temperature being finite, there are still normal conducting electrons, which lead to losses. An approximate surface resistance of an infinitely thick bulk superconductor below its critical temperature is given by [21]:

$$R_s \approx A\lambda_{\text{eff}}^3 \frac{\omega^2}{T} e^{-\frac{\Delta}{k_B T}} \tag{7.6}$$

A is a factor which can be calculated or fitted, λ_{eff} is the effective penetration depth, which is explained as a skin depth for the Cooper pairs. Δ relates to the superconducting energy gap, T is the temperature. The equation has good agreement until $1/2T_C$ [21]. The exponential term comes from quasi particle generation.
So the conductive losses mainly depend on the temperature. This emphasises the importance of achieving an as low temperature as possible, to prevent conductive losses.

7.3.3 Losses to two level systems

The stripline can excite two level systems on the substrate. These are impurities, which can be depicted as dipoles, interacting with the field of the stripline. This leads to losses, known as losses to two level systems. Those losses are related to the second part of equation 7.5. Following [21] they can be estimated:

$$\alpha_{\text{TLS}} = \frac{G_l Z_0}{2} = \frac{\pi^2 c}{\omega} \frac{\epsilon_r}{\sqrt{\epsilon_{\text{eff}}}} \tan \delta_{\text{TLS}} \tag{7.7}$$

In this expression the ϵ's relate to the dielectric constants, c is the speed of light. δ_{TLS} refers to the loss tangent, known from chapter 6.3. It is expected, that for a high input power more two level systems get saturated. Therefore the measured quality factor is higher, as less losses from the stripline to the substrate are possible. For a lower input power, especially around the single photon limit and lower, the internal quality factor should converge to a finite value. With such a low input power, the two level system are not saturated any more and maximum losses to the substrate are present.
The loss tangent for silicon is about 10^{-4} at 6 GHz for low temperatures [29], which is about 2 orders of magnitude higher than for sapphire [20].
Also in the case of a higher temperature more two level systems should be saturated, leading to fewer losses. On the other hand conductor losses will increase with a rising temperature. So two processes take place, leading to opposite effects. Depending on which loss mechanism is dominating, the quality factor will increase, decrease or remain constant if they compensate each other.

7.4 Simulation data

7.4.1 Overview

Simulations with HFSS were performed. The results were compared to the measurements and different configurations were tested to find the best configuration for the measurements (e.g. to have the stripline critically coupled). Comparing the measurements to the simulation results also gives an indication, to which extent the simulation

results can be trusted. This is an important outcome for designing future setups.
The waveguide was modelled several wavelengths long, to avoid effects from the ports. Accurate dimensions were used for width and height. Vacuum was chosen for the inside material. The stripline, sitting on the silicon substrate, was chosen to be a perfect electric conductor.
A waveport without any special constraints was used to excite the waveguide. A fine, length based mesh was assigned to the stripline, to achieve the required accuracy. A length based mesh was also assigned to the silicon, but not as fine as for the stripline. The dielectric constant of the silicon was set to $\epsilon_r = 11.5$ for all the simulations, as the exact dielectric constant of our substrate is unknown and 11.5 replicated the obtained resonance frequencies most accurately.
For the majority of the simulations an interpolating sweep was performed, to save computation time. For most configurations HFSS had no trouble in finding the resonance.
The obtained quantities from the simulations are the resonance frequency and the coupling, expressed by Q_c, which are obtained by exporting the complex values of the S parameters from HFSS and performing a circle fit.
The goal of the simulations was to see the behaviour of the stripline for different configurations and also to get some intuition for its behaviour in the waveguide. Furthermore the simulations were used to probe different setups for the actual experiments and find the most suitable one to measure.
The goal is to have a setup, which is in the order of being critically coupled, as the circle fit works most reliable in that regime. The internal quality factors of the stripline, obtained by the first measurements, are in the range of 1×10^5 to 1×10^6, so the goal is to have Q_c in the same range.
In addition a new waveguide was designed and the simulations were crucial to get the demanded specification. The waveguide is described in chapter C of the appendix.

7.4.2 Symmetric stripline

In this part the simulation results for the symmetric stripline are discussed. Symmetric means in this context, that the leg length is equal on both sides. The dimensions of the stripline were the ones from figure 7.1(a).

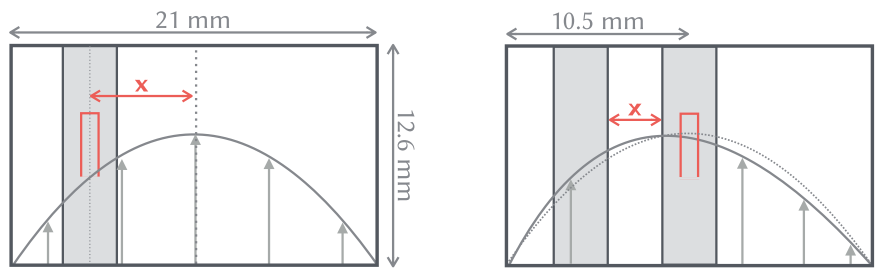

(a) (b)

Figure 7.5: In (a) the position of the SLR within the waveguide was shifted. In (b) the sapphire substrate was shifted, while the position of the SLR was fixed one time to the center and second time to 0.95 mm off center, towards the left wall (and the sapphire).

At first the stripline was shifted along the y axis through the waveguide, see figure 7.5(a). Only the fundamental mode of the waveguide was excited given by the frequency range, having its cutoff around 7.2 GHz. The electric field follows a sine and the

stripline couples to the waveguide mode due to its gradient over y. So for the central position no coupling corresponding to $Q_c = \infty$ is expected, while for the closest position to the wall, the lowest values for Q_c are expected.
The results are plotted in figure 7.6(a), x is the distance from the stripline to the center. Q_c is plotted in a logarithmic scale and shows the expected behaviour for the extreme cases.
The actual waveguide, used for the experiments, has dedicated slots to put the samples, so they cannot be placed arbitrary close to the center, which is required to get a Q_c, being of the same magnitude as the expected Q_i. As a workaround a sapphire substrate was placed in a neighbouring slot of the sample sitting in the center. The sapphire shifts the field, due its high dielectric constant. This is sketched in figure 7.5(b). So for such a configuration it is possible to place the stripline in the center of the waveguide and have a finite Q_c. The simulation results are shown in figure 7.6(b). One time the stripline was

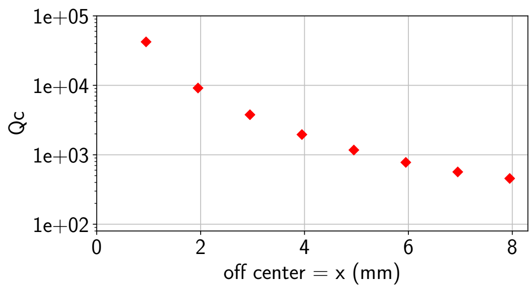

(a)

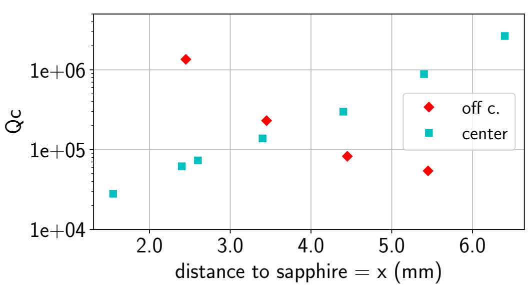

(b)

Figure 7.6: Coupling quality factor of the stripline resonator in different configurations. (a) The position of the stripline was swept, illustrated in figure 7.5(a). The highest coupling was seen, when the stripline was closest to the center. The reason is that the electric field gradient is the smallest in this case. (b) A piece of sapphire was placed in the waveguide, which shifts the electric field of the waveguide mode. The coupling quality factor is plotted versus the distance between the sapphire and the substrate holding the SLR. One time the stripline fixed to the center, one time 0.95 mm from the center, illustrated in 7.5(b). In case the stripline was in the center, the highest coupling quality factor occurs, when the sapphire is far away from the stripline.

placed exactly at the center, the other time the substrate holding it was placed 0.95 mm off center. On the x axis the distance between the substrate with the stripline and the sapphire is plotted. For the stripline placed in the center (blue squares) the highest Q_c is obtained when the sapphire is as far from the stripline as possible. This is expected as the least influence on the field is given, but still enough that the stripline couples to it. For the sapphire moving closer to the center, Q_c decreases due to the stronger perturbation of the otherwise symmetric field.
The values of Q_c for the stripline being 0.95 mm off center are plotted using diamond symbols in figure 7.6(b). The maximum is reached for the sapphire being away from the wall and closest to the sample. This perturbs the field in a way, that it is nearly symmetric over the stripline. These results can be compared with 7.6(a) were in one case the stripline holder was also placed 8 mm from the wall. The coupling quality factor with the additional sapphire are always above the values without the sapphire.
So we see by using a sapphire and placing the stripline in the center, the required values for Q_c can be achieved using the accessable waveguide slots.
The resonance frequencies were found to 7.94 GHz and changed by a few MHz for all the

different setups. So this result is a little more than 300 MHz away from the frequency expected by the discussed model. As there were some assumptions taken, especially that the capacitive coupling between the legs takes only place at their end, this is within the expected accuracy. Compared to the measurements results, which will be discussed in chapter 7.5.7, the HFSS results are closer, being accurate within around 50 MHz. So the circuit model should be taken to get a rough estimate for the resonance frequency and then HFSS should be taken for a more precise prediction.

7.4.3 Symmetric stripline - field analysis

HFSS also allows to plot the fields, which are discussed in this section. To obtain the fields, a port has to be driven, which is done with a watt of power. All the fields are plotted at the resonance frequency of the stripline. The silicon holding the stripline is placed 4 mm away from the left wall.
In figure 7.7 the magnitude of the electric field inside the waveguide is shown. First

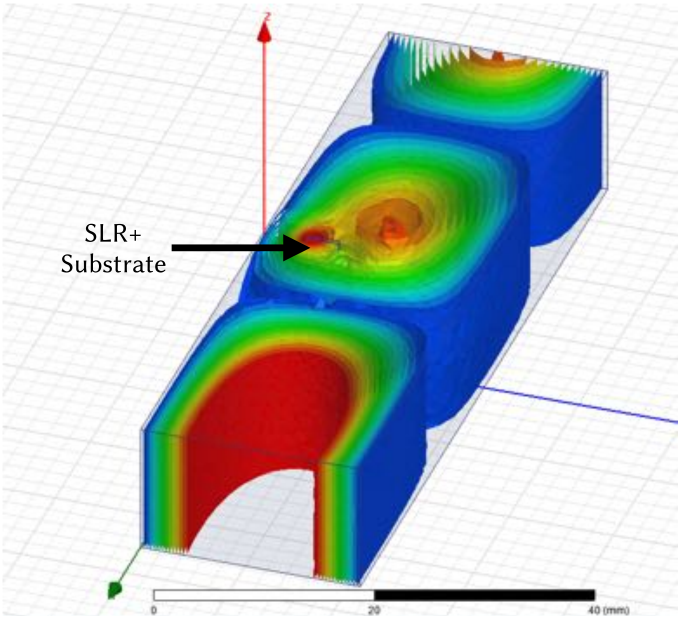

Figure 7.7: Magnitude of the electric field in the waveguide with stripline on a silicon substrate. The stripline can be found close to the coordinate system's origin, at a local field maximum, left from the waveguide center. Red corresponds to a strong field, blue to a weak field (in comparison), the scale is linear.

of all the wavelength, as the distance between two field minima along the propagating direction, coincides with the wavelength of the excitation, which is expected. One has to keep in mind, that the speed of light inside the waveguide is reduced due to an increased wave impedance close to the cutoff frequency of the mode (equation 3.15).
Second we find that the field is lowest at the walls and maximum at the center of the waveguide, moving along the y axis. This is expected, as theory predicts (equation 3.22), that the field follows a sine function, with its maxium in the center.
In addition, the deformation of the field from the silicon and the stripline is seen. The silicon attracts the field due to the higher dielectric constant and this can be perceived in here. Looking at the time evolution, the field would propagate through the waveguide along the propagation direction. In the time evolution animation, the attraction of

the field around the silicon substrate is clearly obtained.

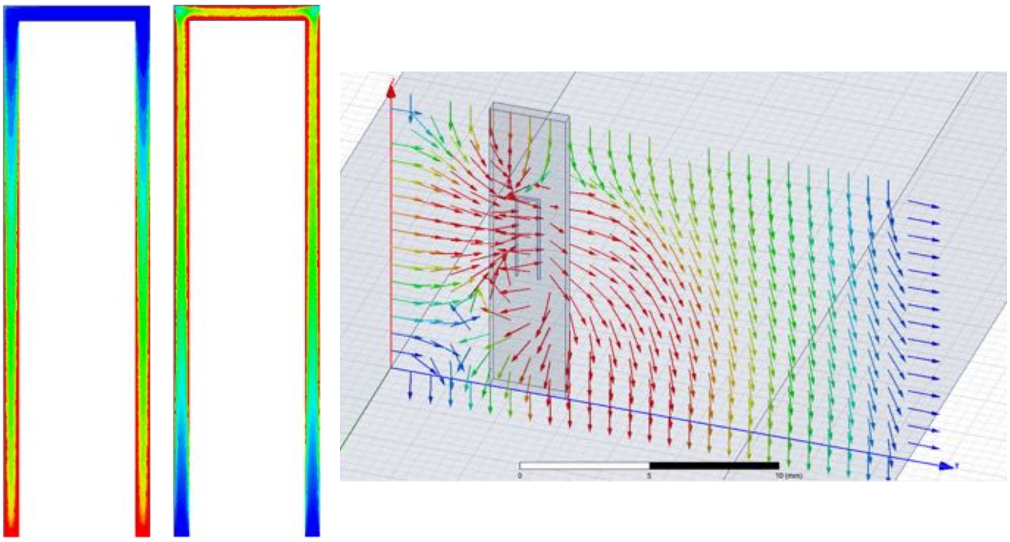

(a) (b) (c)

Figure 7.8: Magnitude of the electric field (a), surface current (b) ($\pi/2$ out of phase) and vectorial depiction (c) of the electric field in the plane of the the symmetric SLR, placed off center in the waveguide. The electric field has a maximum at the end of the legs and a minimum in the center, opposite to the current. This is expected for the stripline being the predicted $\lambda/2$ resonator. Red corresponds to a strong field, blue to a weak field (in comparison), the scale is linear.

In figure 7.8(a) the magnitude of the electric field over the stripline is plotted. As expected from the discussed model, see figure 2.3, the electric field has its maximum at the end of the legs and a node in the center. Thus the stripline represents a $\lambda/2$ resonator. A (small) difference can be recognised between the left and the right leg. On the left leg the field is slightly stronger than on the right leg, which occurs due to the coupling to the waveguide. For the symmetric stripline, the node would be expected to be exactly at the center of the stripline, but due to the electric field, which is higher on the right side, the node is shifted to right, leading to the asymmetry.
Only the magnitude of the field is plotted, so the difference between negative and positive is not obtained. To induce a current flow, one leg has to be charged positive, while the other one is charged negative.
In (b) the magnitude of the surface current is shown, plotted $\pi/2$ out of phase in comparison to the electric field. The current is exactly opposite to the electric field, such that the maximum current is at the center of the stripline and the current is zero at the end of the legs, which again coincides with the expectations.
In (c) the vectorial electric field is plotted in the plane of the stripline. The stripline couples to the waveguide walls which act as a ground. This is a further indication, that the derived model describing the stripline as a transmission line is valid. The waveguide wall is the required second conductor. Moreover the electric field is perpendicular to the waveguide walls and to the stripline. It is strongest in the middle and gets weaker towards the walls. Also the concentration of the field around the stripline is seen and furthermore the perturbation arising from the stripline in combination with the substrate. For a phase being π different, the electric field is reversed, obtained by the electric field vectors pointing in the opposite direction.

7.4.4 Asymmetric stripline

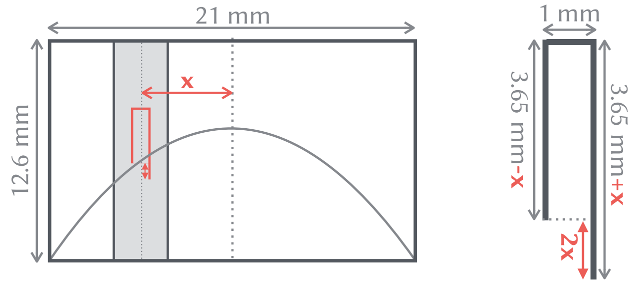

(a) (b)

Figure 7.9: (a) The asymmetric stripline was shifted within the waveguide. The asymmetry of the stripline (length difference between the legs) remained the same. (b) For the stripline, placed in the center of the waveguide, the asymmetry was changed. One leg was extended by the same length the other leg was shortened.

Simulations with an asymmetric stripline were performed. The length of one stripline leg was reduced, while the other one was extended about the same length, illustrated in figure 7.9. The length difference of each leg to the symmetric position is referred to as the asymmetry in the following. The total length of the stripline remained the same. Two different sets of simulations were performed. Illustrated in figure 7.9(a), the asymmetric stripline was shifted through the waveguide, indicated by x in the plot. In this simulation the asymmetry remained constant, being 2 mm. In the second set of simulations, the asymmetry itself was swept for the stripline placed in the center of the waveguide, figure 7.9(b). The results are depicted in figure 7.10.
Close to the wall the highest quality factors are obtained, due to the fact that the asymmetry itself partially cancels the gradient of the field. This leads to a weaker coupling. Around the center Q_c flattens out and the decrease of Q_c is still given, but hard to see in the logarithmic plot. Reaching the other side of the waveguide, the coupling is strongest, there the asymmetry has the same effect as the gradient of the field. For the last data point, where the stripline is close to the waveguide wall, Q_c seems to increase again. There are two effects, which might explain this shift and were not present to that extent for the other data points. The stripline is closest to the wall of the waveguide, so increased coupling to the wall takes place. This might reduce the gradient, and further on increase Q_c. In addition, the substrate holding the stripline is very close to the wall, which might influence the gradient over the stripline. So also this can lead to an increase in Q_c.
In (b) the coupling quality factor against the asymmetry is plotted, this is illustrated in figure 7.9(b). The stripline itself is placed in the center of the waveguide. For the symmetric case an infinite Q_c is expected, assumed to decrease with an increasing asymmetry. The higher the asymmetry, the stronger the stripline couples to the waveguide. The node of the voltage on the stripline is supposed to be in the middle in terms of the stripline length. With a rising asymmetry it shifts towards the longer leg, leading to a higher gradient and a stronger coupling.
In (c) the resonance frequency of the stripline is plotted versus the asymmetry. Compared to the prior sweeps, where the resonance frequency remained nearly constant, a change of more than 10% is observed. This can be explained by a lower shunt capacitance. Comparing the results to the derived model (equation 7.1), the slope of the

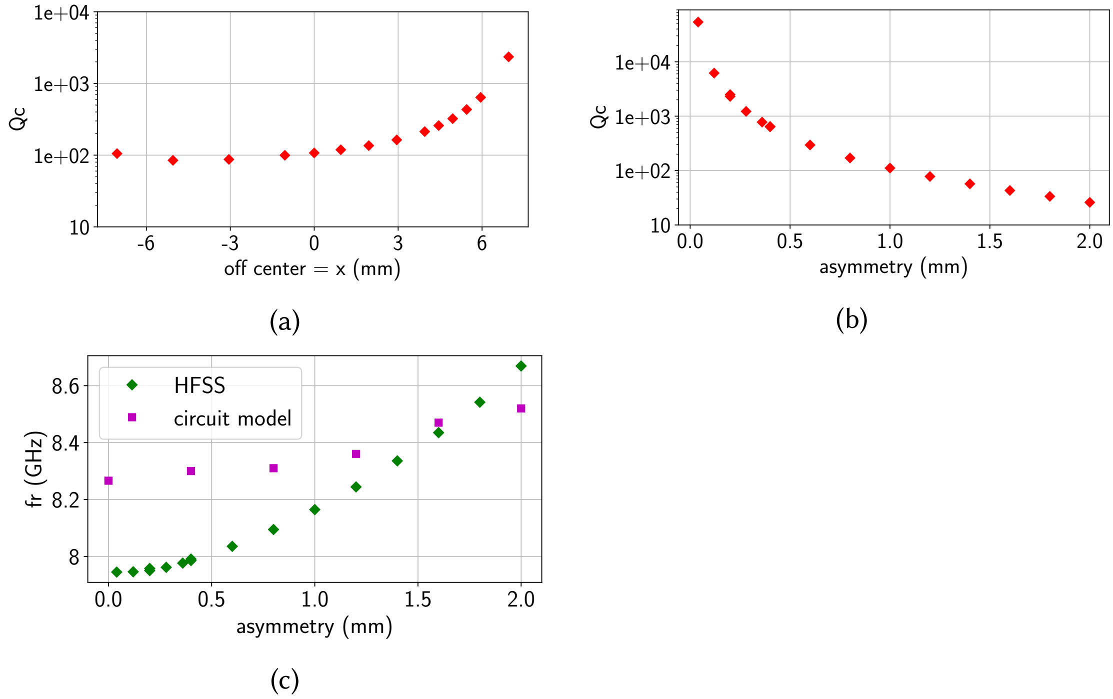

Figure 7.10: Coupling and resonance frequency for different configurations of the asymmetric stripline, sketched in figure 7.9. (a) Coupling quality factor of the asymmetric stripline with an asymmetry of 2 mm for different position within the waveguide. The coupling is the weakest far away from the center, where the asymmetry is similar to the gradient. This reduces the effective gradient over the stripline. (b) Asymmetry of the stripline was swept, for the stripline placed in the center. The higher the asymmetry, the better the coupling, as this leads to a higher effective gradient. (c) Resonance frequency for a swept asymmetry. The higher the asymmetry, the higher the resonance frequency. The reason is, that the shunt capacity gets reduced, related to an increased resonance frequency. The data is compared to the data obtained by the circuit model (chapter 7.2). The data from the circuit model also shows an increasing resonance frequency with asymmetry, but the effect is weaker. Reasons are discussed in the text.

linear (left) part in the equation decreases which leads to higher resonance frequency. In the model the shunt capacitance is the capacitive coupling between the ends of the legs. For the asymmetric stripline the coupling takes place between the end of one, and the middle of the other leg. So this pushes the model to a limit, where the solutions only predict the frequency change partially. This explains the disagreement in the slope between the HFSS data and the data from the circuit model. It still gives the correct picture, but is off in absolute numbers.
In this chapter the HFSS simulation results for a number of different configurations were discussed. The next chapter is about the setups, which were measured, and the results, which will be compared to the simulation data.

7.5 Experimental results

In this chapter the experimental setups and the measurement results of the stripline resonators are discussed. As far as possible the results are compared to the theoretical predictions and the outcomes from the simulations.

7.5.1 Measurement overview

To achieve high internal quality factors the stripline resonators were cooled to a temperature of 20 mK. The samples were put into waveguides fabricated from copper or aluminium, then placed in a dilution refrigerator.
Measurements using the same VNA as for the cavity measurements, described earlier, were performed for different input powers and temperatures. The input power was attenuated around 69 dB by the cables themselves and a series of attenuators. This number was directly measured. The complete measurement setup is discussed and illustrated in chapter D of the appendix.
An important quantity for determining the quality factors is the number of photons in the resonator. It can be estimated using the input power, P_{in}, and the measured quality factors. The following estimation from [30] was used:

$$< n_{\text{ph}} >= \frac{2}{\hbar\omega^2} \frac{Q_l^2}{Q_c} P_{\text{in}} \tag{7.8}$$

So it is dominated by the input power. For the temperature ramp up measurements a heater inside the fridge was used, regulated by a PID controller. After a certain temperature was reached the samples was given sufficient time to thermalise.
The measured data was fitted, using the described circle fit routine, to gain knowledge about the quality factors and the resonance frequency.

7.5.2 Fabrication process

The stripline resonators were fabricated by the Fachhochschule Vorarlberg in two different batches. The first batch consisted of aluminium striplines, the second batch additionally contained ones made from niobium.
In contrast to the first batch, in the second batch the aluminium stripline got exposed to an oxygen plasma after the structures themselves were fabricated. The purpose is to form a controlled, uniform dielectric layer on top of the sample.

7.5.3 Different setups

In figure 7.11 the configurations, which were cooled down in the cryostat and measured are sketched. Details are given in table 7.2. In (a)-(d) the striplines were put in the same waveguide made from copper. One stripline was measured in each cool down. In (e) another waveguide fabricated from copper was used, which was 2 mm wider than the other one.
In (f) the samples were put in an aluminium waveguide, designed in a way that three samples can be measured at the same time. Details about this waveguide, which was fabricated within this thesis, are described in chapter C of the appendix. To measure three samples simultaneously, they were put along the propagation direction in the waveguide. To have their resonance frequency sufficiently far apart, an additional piece of silicon substrate was put at the back of two of the substrates holding the stripline. Additionally one of the striplines backed with a silicon substrate had a designed resonance frequency of 7.5 GHz, due to 0.2 mm longer legs. The additional silicon substrate at the back increases the effective dielectric constant, leading to a decreased resonance frequency.

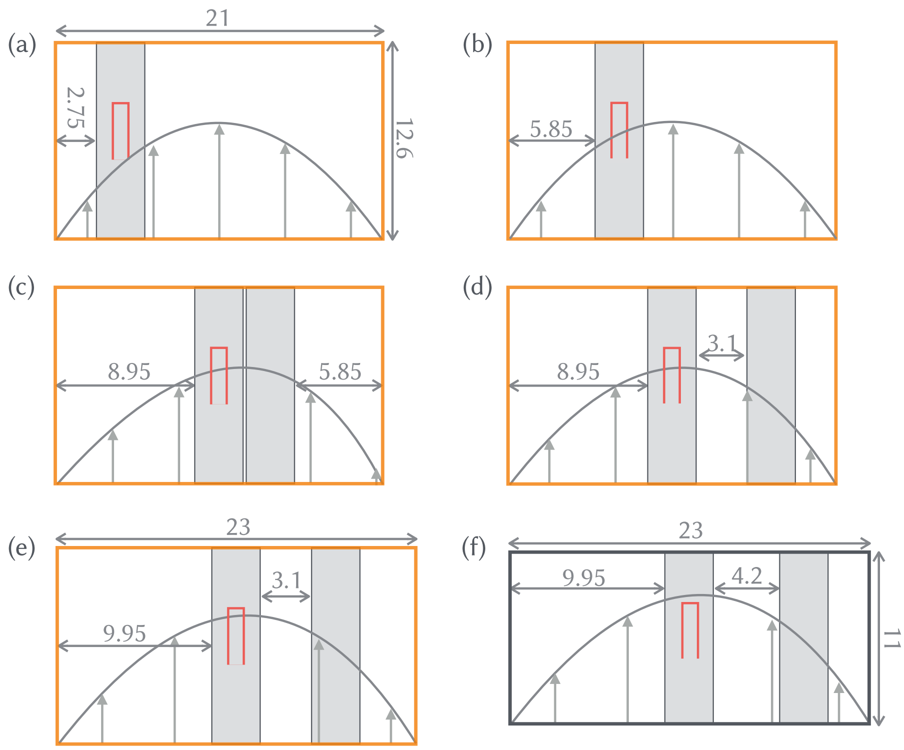

Figure 7.11: Actual setups, which were cooled down in the cryostat and measured. In (f) three striplines were put in the same configuration in the same aluminium waveguide along the propagation direction. In (a)-(e) the waveguides were fabricated from copper (illustrated with colored wall). Details are given in table 7.2. The dimension of the stripline and the substrate are given in figure 7.1.

From (d) on the second batch of striplines was measured, in (e) the stripline was fabricated from niobium, in (f) two of the three striplines were made from niobium, setup (f2) and (f3). The stripline measured in (f1) was exactly the same as measured in (d), otherwise different striplines were used in every measurement.
To shift the field, required for the central striplines in (c)-(e), a substrate of sapphire was used. The dimensions of the sapphire substrate were similar to the dimensions of the silicon substrate containing the sample. For (f) silicon substrates, instead of sapphire ones, were used to shift the field inside the waveguide. Due to their similar dielectric constant the influence on the field is comparable to the one of the sapphire substrate. The use of silicon was required due to the modified sample mounting system in the aluminium waveguide.

7.5.4 Coupling in different setups

In figure 7.12 the coupling quality factors for all the different configurations with respect to the number of photons in the resonator are plotted. The simulation results, which were obtained by simulating S_{21} and using the circle fit, are plotted as lines, the measured data is depicted by points. Overall agreement is observed between the measurements and the simulation data. There is no strong dependency, which is expected, as the coupling should not depend on the input power.
The stripline sitting closest to the wall (a) has the lowest Q_c, followed by the setup where

Setup	WG	WG width	SLR		Wall - SLR	Sapphire - SLR
(a)	Copper	21 mm	Al	8 GHz	2.75 mm	-
(b)	Copper	21 mm	Al	8 GHz	5.75 mm	-
(c)	Copper	21 mm	Al	8 GHz	8.95 mm	0 mm
(d)	Copper	21 mm	Al	8 GHz	8.95 mm	3.1 mm
(e)	Copper	23 mm	Nb	8 GHz	9.95 mm	3.1 mm
(f1)	Aluminium	23 mm	Al	8 GHz	9.95 mm	4.3 mm
(f2)	Aluminium	23 mm	Nb	8 GHz	9.95 mm	4.3 mm
(f3)	Aluminium	23 mm	Nb	7.5 GHz	9.95 mm	4.3 mm

Table 7.2: Different setups in which the striplines were measured. The setups are sketched in figure 7.11. 'Wall - SLR' is the distance from the wall to the substrate with the stripline. The distance sapphire to SLR gives the difference between the neighbouring substrates, if present. In configuration (f), instead of the sapphire, silicon was used to shift the field, which has a similar dielectric constant and therefore a similar influence on the field. The exact same stripline was used in setup (d) and (f1). Otherwise the measured stripline was always a new one. In setups (a)-(c) striplines from the first batch, in (d)-(f) striplines from the the second batch were used.

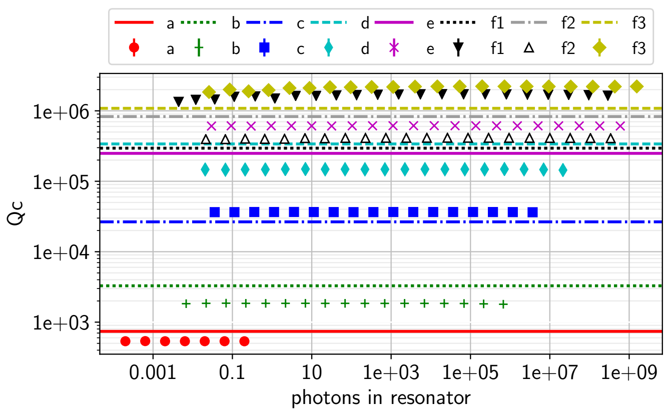

Figure 7.12: Coupling quality factor in different configurations (see 7.11). The lines depict the simulated data, the points are the measurements. Details are discussed in the text.

the stripline was moved closer to the center, (b), in line with the expectations. The next higher Q_c is measured for the stripline in the center with the sapphire substrate right next to it. The difference between the quality factors, observed from the measurements as well as the simulation data, is more than a magnitude for this configuration.
It is surprising, that the coupling is stronger for configuration (d) than for (e). The relative influence from the sapphire on the waveguide field should be higher in (e) than in (d), leading to a stronger coupling. The reason is that the sapphire remains at the same distance, while the waveguide is narrower, thus the influence on the field is stronger. Also according to the simulations the quality factors should be the other way around.
A possible explanation is the critical influence of the stripline position on the coupling. Especially when the gradient of the electric field is low, which is the case for a centrally positioned stripline. In (e) the slot to put the substrate was shorter than in the other waveguide. This leads to a possible bigger deviation in the position of the stripline. Performing simulations it was seen, that a different position of 0.8 mm can lead to a difference of the coupling quality by a factor of 7.
In (f) the silicon substrate shifting the field was further away from the centrally placed

stripline. The quality factors there are the highest, in line with the expectations. The stripline (f1), which is not backed with an empty silicon substrate has a higher Q_c than (f2), backed with a substrate. It is not possible to explain this with the variance of the substrate position. The aluminium waveguide used here has fixed slots for the samples (see appendix). A possible reason is, that the stripline itself was not in the center of the substrate. Another possible reason can be a slightly asymmetric stripline, which would also lead to a different coupling (see figure 7.10c). Still the quality factor is in the expected range from the simulations.
Comparing simulation and measurement shows reasonable agreement. Especially for higher Q_c's the deviation is bigger for some measurements. A possible reason, as discussed, is variance of the stripline position and the leg length.

7.5.5 Internal quality factor dependence on the circulating power

Aluminium stripline

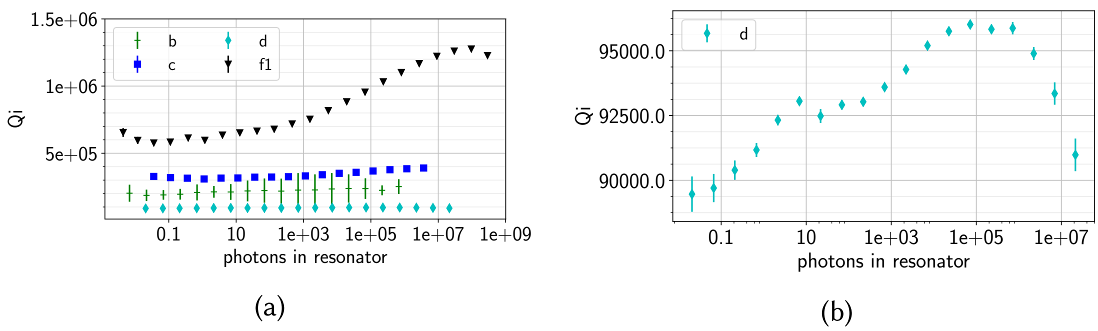

Figure 7.13: Internal quality factors of aluminium striplines against the number of photons in the resonator. The coupling quality factors were around 2×10^3 for (b), 2×10^4 for (c), 1×10^6 for (d) and 1.5×10^6 for (f1), see figure 7.12. (a) Internal quality factor is the highest for the stripline in the aluminium waveguide (f1), which was exactly the same stripline as measured in (d). The highest internal quality factor measured in the copper waveguide was slightly above 3×10^5. For all striplines a decreasing internal quality factor with lower power is obtained. In (b) the results of the aluminium stripline in setup (d) are plotted in detail.

The internal quality factors of the aluminium striplines are plotted in figure 7.13. The measurement of setup (a), where the stripline was closest to the wall is not plotted. This was measured in the highly over coupled regime and no useful information about Q_i could be extracted. In addition to the poor regime, it was only measured under low input power, below the single photon limit (see for example figure 7.12), where the error is naturally higher.
In the configurations (b)-(d) the striplines were measured in a copper waveguide, while configuration (f1) was measured in an aluminium one. The advantage there is, that aluminium gets superconducting below 1.1 K [31]. This prevents losses in the waveguide walls and the formation of vortices due to trapped flux by shielding the external magnetic field.
In (b) a stripline from the first batch, was placed off center. A slight trend, for a decreasing Q_i with photon number is observed. At the single photon limit the internal quality factor is around 2×10^5. The error is still substantial, due to a coupling quality factor being a factor of 100 lower than the internal one. In (c) a different stripline with the

same dimensions was measured, placed in the central slot of the waveguide. It is still in the over coupled regime with the ratio Q_i to Q_c being 10:1. This is sufficient for the circle fit to give reliable data. A trend of a decreasing quality factor with the photon number in the resonator is observed, still it is in the same range for low and for higher power.
In configuration (d) results for the internal quality factor of a stripline from the second batch, placed in the same copper waveguide as used in (b) and (c) is plotted. The field shifting sapphire is now placed one slot further away from the stripline being in the center, which makes the stripline critically coupled. The internal quality factor is lower compared to the others, being around 1×10^5. In 7.13(b) this quality factor is plotted in detail, where it is seen that it increases with photon number. The relative difference is below 10%. The reason for the lower internal quality factor could arise from some frozen fluxoids or vortices, caused by a high magnetic field from a neighbouring lab during the cool down process. A higher photon number in the stripline was reached due to the higher total quality factor. Near the maximum photon number, a decrease in the quality factor is obtained, which could be due to a higher current leading to conductor losses dominating over the reduced losses to two level systems.
The exact same stripline was put in the aluminium waveguide in a similar setup, sketched in figure 7.11. The data points are labelled with (f1) in 7.13(a). The internal quality factor in the single photon limit is around 6 times higher as compared to before. To some extend this can be explained with the reduced losses in the waveguide wall. As seen for the niobium striplines in the following section, the difference seems to be around a factor of 1.5, so this does not account for all the improvement. A possible explanation is, that there was no magnetic field present during the cool down process, due to the shielding from the aluminium waveguide, which probably was the reason for the low Q_i before (see earlier discussion).
The difference between the internal quality factor for low and high power is around a factor of 2. This is more than measured for the other aluminium striplines. Again for the highest photon numbers a maximum in the quality factor is reached, and the quality factor seems to decrease for higher input power.
To conclude, for the aluminium stripline in the copper waveguide a maximum quality factor of around 3×10^5 is achieved at the single photon limit. In the aluminium waveguide this is about two times higher. The quality factor has a decreasing trend for lower photon numbers, which can be seen to a different extent in the different setups. This can be explained with the increasing losses to the two level systems of the substrate.

Niobium stripline

In figure 7.14 the quality factor of the niobium stripline versus the number of photons in the resonator is plotted. Setup (e) was the only one in the copper waveguide, while for the other two measurements the striplines were inside the aluminium waveguide.
For the stripline in the copper waveguide quality factors of around 7×10^5 are observed at the single photon limit, which is higher than the quality factor of every measured aluminium stripline in the single photon limit. Again the quality factor increases with increasing photon number and its measured maximum is around 3 times as high as compared to the single photon limit. In comparison to the aluminium stripline there is no plateau for high photon numbers.
The results of the 8 GHz niobium stripline in the aluminium waveguide are labeled as

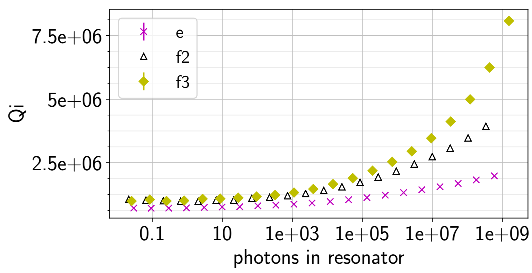

(a) Nb SLR

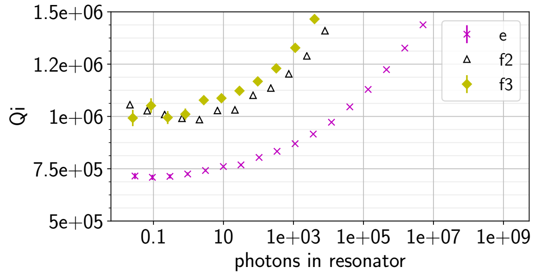

(b) Nb SLR - low input powers

Figure 7.14: Internal quality factor of the Nb stripline for different number of photons in the resonator. In (a) the whole range of measured Q_i's is plotted and in (b) a zoom to see the single photon limit is plotted. The coupling quality factors were between around 5×10^5 and 2×10^6 (figure 7.12), which made a good range for the circle fit, given the internal quality factors. The internal quality factor for the stripline in the copper waveguide was around 7×10^5 and 1×10^6 for the striplines in the aluminium waveguide. A clear dependency on increasing Q_i with photon number is observed.

(f2) in 7.14. The quality factor for low power is around one million, which is around 50% higher than for the stripline in the copper waveguide. The difference here is lower than for the aluminium stripline measured in (d) and (f1). A possible reason was discussed in the previous section. For high power, the increase is around 4 times, which is similar to the copper waveguide.
In (f3) the internal quality factor of the niobium stripline with a nominal resonance frequency of around 7.5 GHz is plotted. In the low power limit its internal quality factor around a million, which is similar to the other stripline. For high photon numbers the quality factor is around twice as high, compared to the other stripline.
To conclude a clear trend for a rising quality factor with increasing photon number was obtained, which is higher than for the aluminium stripline. The quality factor for low photon numbers is around twice as high as for the aluminium stripline, also no plateau is reached for high photon numbers. An explanation is that the critical temperature for niobium is higher with around 8 K [32] compared to 1.2 K [31] for aluminium. So the conductor losses are minor for the measurement regime and the saturation of two level systems, leading to fewer losses, is still dominating.

7.5.6 Internal quality factor dependence on the temperature

The temperature of the cryostat was increased using the previously described heater until around 1.2 K. In steps of a around 100 mK measurements were performed for low input powers around the single photon limit and high input powers (magnitudes above single photon limit).
We expect two effects. On one hand an increasing saturation of the two level systems on the substrate, with rising temperature, leading to an increased Q_i. On the other hand a decrease of Q_i due to an increase of normal conducting electrons in the striplines themselves, leading to losses. Temperature ramps were done for the aluminium stripline in configurations (c) and (d), in the copper waveguide and configuration (f1) in the aluminium waveguide and for all the measured niobium striplines, setups (e), (f1) and (f2). In the aluminium waveguide a further effect is expected, as the superconductivity of the aluminium breaks down around 1 K. So an additional decrease in the internal quality

factor is expected due to increasing losses in the waveguide walls.

Aluminium stripline

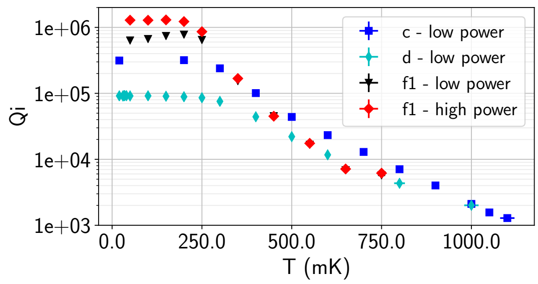

Figure 7.15: Internal quality factor dependence of aluminium striplines on the temperature. Stripline in the copper waveguide (c), (d) and in the aluminium waveguide (f1).

In figure 7.15 the results for the aluminium striplines are plotted. High power measurements were performed before and after the low power measurement, to see if the stripline had thermalised. In configuration (d) the internal quality factor was barley power dependent (figure 7.13), so only the low input power values are plotted.
Independent of the configuration, all striplines showed a decreasing quality factor from around 400 mK onwards. The measured values are similar for each temperature, independent of the configuration. The decrease seems to have approximately the behaviour expected from conductive losses, equation 7.6. However some additional effects have to be taken into account, as the stripline is just a thin film, compared to the model, which assumes bulk aluminium. So the model gives an estimate to the losses, but does not describe the measurement data in full extent.
The critical temperature for aluminium is around 1.2 K, so at around this temperature a quality factory, related to the normal state resistance of aluminium is expected. Simulations with HFSS were performed, where aluminium, instead of a perfect electric conductor, was used for the stripline material. The values measured for around 1 K are in the same range as as thos. This meets the expectations, and the quality factor is then also expected to converge around this value.
Measurements above 1.1 K were not possible, as the resonance vanished within the ripples of the transmission spectrum, since the coupling quality factor being a lot higher than the internal one. The striplines were measured in the then under-coupled regime, since critical coupling was required for low temperatures. Especially in (f1) having the weakest coupling, measurements for above 750 mK were not possible.
Investigating the data at low temperatures, the quality factors stay approximately constant until 200 mK - 300 mK.
The results show the same behaviour as in [20], where an aluminium cavity was measured.
For the stripline in the aluminium waveguide, measured around the single photon limit, a small increase in the quality factor is seen up to 200 mK. This can be explained with the reduced losses to two level systems dominating over increasing conductor losses. Afterwards a decrease is measured, probably slightly earlier than for the other striplines. The most likely reason is the increasing resistance of the aluminium waveguide walls. The stripline is also closer to the waveguide walls in this setup.

Niobium stripline

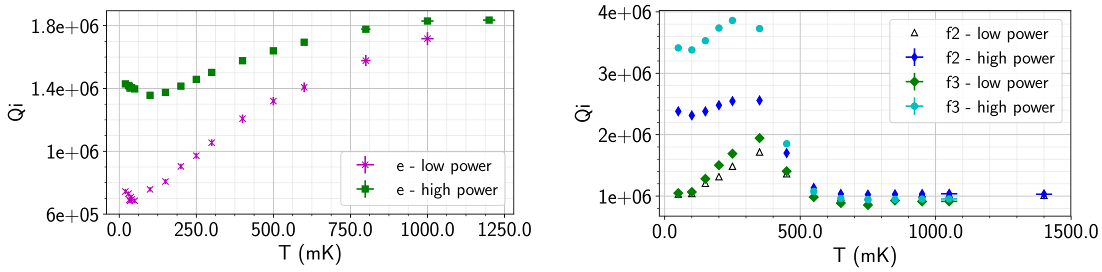

(a) (b)

Figure 7.16: Internal quality factor of the niobium stripline in dependence of the temperatures. (e) in the copper, (f2), (f3) in the aluminium waveguide.

The results of the niobium stripline are plotted in figure 7.16. The behaviour is strongly dependent on the waveguide material.
For the stripline in the copper waveguide, figure 7.16(a), at first a slight decrease of the quality factor is measured, followed by an increase, continuing for the whole measurement range (up to 1.2 K). The losses around 1.2 K appear to be mostly independent of the input power. The increased temperature saturates the two level systems, leading to fewer losses. The critical temperature, being around 8 K, does not play a major role in the region below and around 1 K, in contrast to the aluminium stripline.
In 7.16(b) the results for the 7.5 GHz and 8 GHz stripline in the aluminium waveguide are plotted. The results are similar to the ones in the copper waveguide until around 300 mK. Above this temperature, the quality factor for the stripline using high power begins to decrease. For the low input power this takes place around 400 mK. This might be explained with increasing losses in the waveguide walls. For the low input power the increased saturation of the two level systems seems to be still dominating. After about 550 mK the quality factors for high and low power are similar and remain constant. The losses to the walls seem to have a bigger influence in the aluminium than in the copper waveguide, which arises from the higher resistivity of aluminium. HFSS simulations, where a finite conductivity was assigned to the waveguide walls, were performed. For the waveguide 5083 aluminium was used, so the value for its conductivity, found in [33], was taken. The simulation gave a value for the internal quality factor of around 1.2×10^6. Compared to the measurement, giving a quality factor around 1×10^6, the losses to the wall seem to be the dominating loss mechanism. The difference to the simulation results, can be explained with further imperfections, and other loss mechanism, like two level systems, which are not taken into account in the simulations.
The coupling quality factor does not change significantly for the aluminium and the niobium striplines in the measured configurations. It remains at the value, measured at base temperature, figure 7.12. This is the reason for the values not being plotted.

7.5.7 Resonance frequencies in different setups

In figure 7.17 the resonance frequencies against the number of photons in the resonator are plotted. In (a) the resonance frequencies of all the measured setups are plotted, in (b) only the ones with the same nominally resonance frequency. The resonance frequencies remained constant for the whole range of input powers, which is expected.

In the setup (f2) the intention was to shift the frequency of an 8 GHz SLR by backing the substrate holding the stripline with an empty substrate, which increases the effective ϵ_r. This leads to a decrease of the resonance frequency of around 200 MHz, which is around 100 MHz less than expected from the simulations. Also in (f3) where a 7.5 GHz stripline was put in a similar setup, the empty substrate seems to shift the resonance frequency around 200 MHz. This is again not as much as expected from the simulations. A possible explanation for the deviation of the simulations is that the two substrates are not completely touching, as they are in the simulations. Also ϵ_r can be different form the assumed value in the simulations. Still the simulations are in the same order of magnitude.

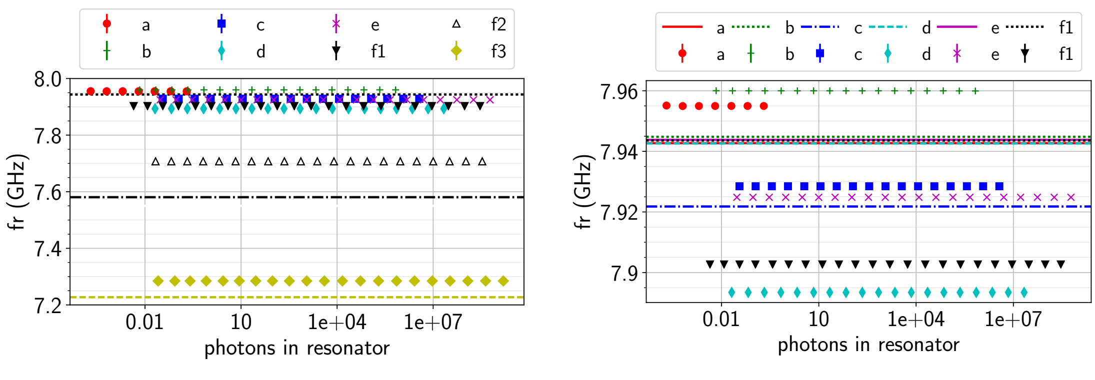

Figure 7.17: Resonance frequency for the different setups. Simulated data from HFSS plotted as lines to compare with measurement data (points). In (a) all configurations are plotted, in (b) only the ones with the same nominal resonance frequency.

In figure 7.17(b) the resonance frequencies of the striplines having nominally a resonance frequency of 8 GHz are plotted. The setups without a neighbouring sapphire have a higher resonance frequency than the one with a sapphire placed next to them. An additional sapphire leads to a slightly increased capacitance of the stripline, leading to a lower resonance frequency, due to the additional dielectric between the stripline and the waveguide wall. This can be obtained in the discussed circuit model, equation 7.1.

The simulated data did not predict the obtained variance for the given setups, but was still within around 50 MHz of the measured frequency. Even though it is not exactly accurate this should be sufficient to plan setups using the simulations.

A possible reason for the different resonance frequency, can be found in a slightly different length of the stripline. According to simulations a length difference of 0.05 mm (both legs shortened about 0.05 mm) leads to a shift of 100 MHz in resonance frequency. Also a different ϵ_r leads to a different resonance frequency.

Comparing to the circuit model, which predicts a resonance frequency of 8.27 GHz, the measurement results are within 400 MHz. Still the simulation results are closer. So the circuit model can be taken to get a rough estimate for the resonance frequency. To get a more exact value for the resonance frequency, finite element simulations should be performed.

7.5.8 Resonance frequency dependence on the temperature

Aluminium stripline

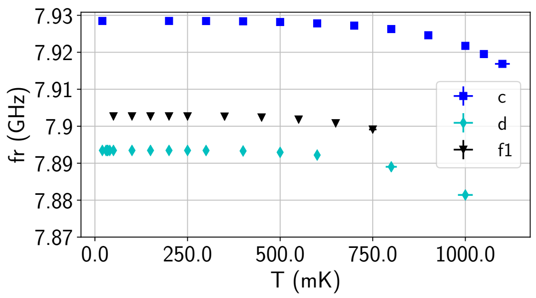

Figure 7.18: Shift of the resonance frequency under ramping up of the temperature.

In figure 7.18 the resonance frequency with respect to the temperature of the aluminium stripline is plotted. As it is not power dependent, it is not necessary to distinguish between low and high input power.
The behaviour is similar for all measured striplines. Up to around 600 mK the resonance frequencies remain constant and decrease afterwards. The decrease is in the regime of 10's of MHz. Compared to [34], where an aluminium cavity was measured, the behaviour is similar. In this paper the frequency drop is explained with BCS theory and the rising surface impedance for an increasing temperature.
It is expected that for temperatures above the critical temperature this decrease does not continue, which could not be measured.

Niobium stripline

The results for the niobium striplines are plotted in figure 7.19, relative to the the resonance frequency at 50 mK. The difference is in the range of a few kHz, furthermore the

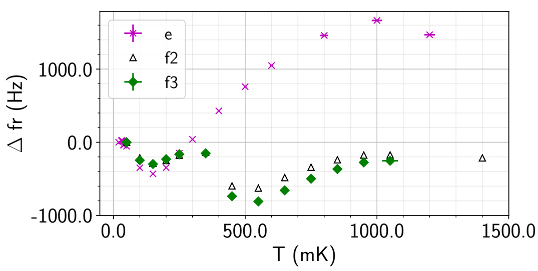

Figure 7.19: Relative shift of the resonance frequency in comparison to its value at 50 mK, which was the first data point.

behaviour is similar to the one of the internal quality factor. For the values until 300 mK, before the influence of the aluminium waveguide walls starts, the trend is similar for all the measured striplines. In [35] a coplanar waveguide, also fabricated from niobium is measured. A similar trend to setup (e) for increasing temperature is observed. In there the frequency shift is explained with the two level systems leading to a variation in the dielectric constant of the substrate, being related to a shift in resonance frequency. This explains the behaviour for the whole measured range.

To conclude, measurements of stripline resonators in a waveguide were presented in this chapter. A circuit model allowing to calculate the resonance frequency was developed. The calculated values agree with the measured data in the expected accuracy, being around 5% off. More exact results were obtained with HFSS simulations. Also the coupling between the stripline and the waveguide could be estimated using the simulations.
The measurement data showed a maximum internal quality factor of around 6×10^5 for the aluminium stripline and one million in case of the niobium stripline in the single photon limit. This was measured for the stripline in the aluminium waveguide. In the copper waveguide the internal quality factors were a factor 1.5 (niobium) and 2 (aluminium) lower. For higher input powers an increase in quality factor was measured, to a different extent, depending on the setup.
Doing measurements with an increasing temperature up to about 1 K, a general decrease in quality factor for the aluminium stripline was seen. This is due the critical temperature, being around 1.2 K. For the niobium striplines a general increase in quality factor was seen. The critical temperature for niobium is around 8 K, so its influence could not be measured. When it was placed in the aluminium waveguide, around 400 mK a drop in the quality factor was observed. This can explained with losses in the waveguide walls.

Chapter 8

Conclusion and outlook

In the first part of this thesis the development of a circular chiral waveguide was presented, which did not leave the simulation stage. The waveguide was the first step in building a system with directionality, such that communication between qubits is only possible in one direction. Simulations showed that right circular polarised waves could propagate nearly lossless, while left polarised signals were attenuated by around 99%. Combining the waveguide with spiral antennas, which were developed for the feed, an overall symmetry was obtained and the directionality was lifted. This can be explained by the antenna theorem.
Microwave resonators in notch and reflection configuration were discussed. Under this thesis, the circle fit was implemented. It makes use of the complex nature of the S-parameters to extract information about the internal and coupling quality factor of a resonator, as well as its resonance frequency. Reflection measurements of microwave cavities made from aluminium and copper are presented. They were performed using different measurement setups and the cavities were investigated in the over- and under coupled regimes. Similar results were found, independent on the overall setup outside. This implies, that the cavities themselves can be measured independent of the setup. Furthermore the behaviour between the coupling pin and the coupling quality factor is within the expectations. The measurements also agree with HFSS simulations. Important information for assembling future setups can be extracted from this work.
U-shaped striplines fabricated from aluminium and niobium were put in a 3D rectangular waveguide and cooled down in the cryostat to its base temperature, being around 20 mK. They were measured for different input powers, while low input powers, around and below the single photon limit, were of special interest. In addition, they were measured under increasing temperature up to around 1 K. The analysis was done using the developed circle fit routine. An aluminium waveguide was designed and fabricated, which allowed to measure the samples more efficiently, replacing the copper waveguide used for the earlier measurements.
In order to obtain knowledge about their quality factors, a configuration with critical coupling was required. Internal quality factors for niobium striplines were found to be around 7×10^5 and 1×10^6, depending on the waveguide material (copper or aluminium), in the single photon limit. The quality factor of the aluminium stripline was measured to be between 1×10^5 and 6×10^5. Both striplines showed an increasing internal quality factor for increasing input power, expected due to the saturation of two level systems.

With increasing temperature, the niobium stripline showed improvements, most likely again due to saturation of two level systems. In the aluminium waveguide, a decrease was seen for temperatures above 400 mK, explained by losses in the waveguide wall. The aluminium stripline showed a decrease from around 300 mK onwards, independent of the waveguide material. This can be explained by increasing conductive losses, as the critical temperature from aluminium is around 1.2 K.
Simulations performed with HFSS give similar values of the coupling and the resonance frequency, compared to the measurements. A circuit model was developed, modelling the stripline as a transmission line with a shunt capacitance. Its results for the resonance frequency are within the expectations, compared to the measurements.
In a next step, the stripline should be coupled to qubits and serve as a readout resonator. The qubits will be placed in the waveguide in a way, they strongly couple to the stripline, but not to the waveguide mode. The striplines furthermore will be strongly coupled to the waveguide, which can be achieved by placing them off center or using asymmetric ones. In that case (nearly) all losses are coupling losses and the internal losses are highly suppressed.

Bibliography

1. Nielsen, M. A. & Chuang, I. L. *Quantum Computation and Quantum Information: 10th Anniversary Edition* (Cambridge University Press, 2010).
2. Cirac, J. I. & Zoller, P. Goals and opportunities in quantum simulation. *Nature Physics* **8,** 264–266. issn: 1745-2473 (2012).
3. DiVincenzo, D. P. & IBM. The Physical Implementation of Quantum Computation. *Fortschritte der Physik* **48,** 771–783 (2000).
4. DiVincenzo, D. P. Two-bit gates are universal for quantum computation. *Physical Review A* **51,** 1015–1022 (1995).
5. Ladd, T. D. *et al.* Quantum computers. *Nature* **464,** 45–53 (2010).
6. You, J. Q. & Nori, F. Atomic physics and quantum optics using superconducting circuits. *Nature* **474,** 589–597 (2011).
7. Devoret, M. H., Wallraff, A. & Martinis, J. M. Superconducting Qubits: A Short Review. *arXiv:cond-mat/0411174* (2004).
8. Frunzio, L., Wallraff, A., Schuster, D., Majer, J. & Schoelkopf, R. Fabrication and characterization of superconducting circuit QED devices for quantum computation. *IEEE Transactions on Applied Superconductivity* **15,** 860–863 (2005).
9. Pozar, D. M. *Microwave engineering* 4th ed (Wiley, Hoboken, NJ, 2012).
10. Leeson, D. B. *S-Parameter Matrices* tech. rep. (1999).
11. Burt, G. Dispersion of helically corrugated waveguides: Analytical, numerical, and experimental study. *Physical Review E 70* (2004).
12. Foulds, K. W. H. & Mansell, J. R. Propagation of an electromagnetic wave through a helical waveguide. *Electrical Engineers, Proceedings of the Institution of* **111** (1964).
13. Hirose, K., Miyamoto, M. & Nakano, H. A two-wire spiral antenna backed by a plane reflector with an unbalanced feed system. en. *Electronics and Communications in Japan (Part I: Communications)* **86** (2003).
14. Stutzman, T. *Antenna Theory and Design* (Wiley, 1981).
15. Plum, E., Fedotov, V. A. & Zheludev, N. I. *Asymmetric transmission through chiral symmetry breaking in planar metamaterials* in *Quantum Electronics and Laser Science Conference* (Optical Society of America, 2008).
16. Fedotov, V. A. *et al.* Asymmetric Propagation of Electromagnetic Waves through a Planar Chiral Structure. en. *Physical Review Letters* **97** (2006).

17. ANSYS. *HFSS Theory* (Maxwell Online Help System, 2001). <http://www.oldfriend.url.tw/Tutorials/Ansoft/hfss/HFSS_Theory.pdf>. (visited Mar. 2017).

18. *Wave Ports and Lumped Terminals* <http://www.cc.ntut.edu.tw/~juiching/Ports.pdf>. (visited Mar. 2017).

19. Geerlings, K. *Measurement of High Q Weakly Coupled Microwave Resonators* 2011.

20. Reagor, M. J. *Superconducting Cavities for Circuit Quantum Electrodynamics* PhD thesis (Yale University, Yale, 2015).

21. Meier, S. *Loss reduction of superconducting coplanar microwave resonators on sapphire substrates* BA thesis (2014).

22. Palacios-Laloy, A. *Superconducting qubit in a resonator: Test of the Leggett-Garg inequality and single-shot readout* PhD thesis (CEA Saclay, 2010).

23. Investigation of Room Temperature Oxidation of Cu in Air by Yoneda-XAFS. *AIP Conference Proceedings* **882,** 490–492 (2007).

24. Probst, S., Song, F. B., Bushev, P. A., Ustinov, A. V. & Weides, M. Efficient and robust analysis of complex scattering data under noise in microwave resonators. *Review of Scientific Instruments* **86** (2015).

25. Gao, J. *The physics of superconducting microwave resonators* PhD thesis (California Institute of Technology, 2008).

26. Staples, J. *Impedance Matching and Smith Charts* <http://uspas.fnal.gov/materials/08UCSC/mml13_matching+smith_chart.pdf>. (visited Mar. 2017).

27. Manfreda, G. Review of ROXIE's Material Properties Database for Quench Simulation. *TE Technology department internal note* **35** (2011).

28. Masluk, N. A., Pop, I. M., Kamal, A., Minev, Z. K. & Devoret, M. H. Microwave Characterization of Josephson Junction Arrays: Implementing a Low Loss Superinductance. *Physical Review Letters* **109** (2012).

29. Krupka, J. *et al.* Measurements of Permittivity, Dielectric Loss Tangent, and Resistivity of Float-Zone Silicon at Microwave Frequencies. *IEEE Transactions on Microwave Theory and Techniques* **54** (2006).

30. Bruno, A. *et al.* Reducing intrinsic loss in superconducting resonators by surface treatment and deep etching of silicon substrates. en. *Applied Physics Letters* **106** (2015).

31. Boato, G., Gallinaro, G. & Rizzuto, C. Effect of Transition-Metal Impurities on the Critical Temperature of Superconducting Al, Zn, In, and Sn. *Physical Review* **148** (1966).

32. Rairden, J. R. & Neugebauer, C. A. Critical temperature of niobium and tantalum films. *Proceedings of the IEEE* **52** (1964).

33. *Conductivity and Resistivity Values for Aluminum & Alloys* 2002. <https://www.nde-ed.org/GeneralResources/MaterialProperties/ET/Conductivity_Al.pdf>. (visited Mar. 2017).

34. Reagor, M. *et al.* Reaching 10 ms single photon lifetimes for superconducting aluminum cavities. *Applied Physics Letters* **102** (2013).

35. Gao, J. *et al.* Experimental evidence for a surface distribution of two-level systems in superconducting lithographed microwave resonators. *Applied Physics Letters* **92** (2008).

36. ANSYS. *Maxwell 3D - user's guide* (2005). <http://ansoft-maxwell.narod.ru/en/CompleteMaxwell3D_V11.pdf>. (visited Mar. 2017).

37. ANSYS. *Lecture1: Introduction to ANSYS Maxwell* (2013). <http://ansoft-maxwell.narod.ru/en/Maxwell_v16_L01_Introduction.pdf>. (visited Mar. 2017).

38. Di Lorenzo, E. *The Maxwell Capacitance Matrix* tech. rep. (2011). <http://www.fastfieldsolvers.com/Papers/The_Maxwell_Capacitance_Matrix_WP110301_R01.pdf>. (visited Mar. 2017).

Appendices

Appendix A

Circle fit

In this chapter additional details about the circle fit (chapter 6.4) are given.

A.1 Error calculation

An estimation for the fitting error is given for each parameter. This chapter describes, how this fit error is computed.
To obtain the errors, the Jacobian matrix is calculated. In addition the squared standard deviation, σ^2, is evaluated using the following relation:

$$\chi^2 = \frac{1}{N-n} \sum_{f_i}^{N} \frac{data(f_i) - S_{21}(f_i)}{\sigma_i} \tag{A.1}$$

Where $data(f_i)$ refers to the measured data point at the given frequency f_i, N is the total number of measured points, while n denotes the number of degrees of freedom, being 7 in the case of the circle fit (6 for reflection). S_{21} refers to the data calculated from the model. In reflection S_{11} is used.
The above equation is set equal to 1, meaning that $\chi = 1$ and in addition $\sigma = \sigma_i$ such that σ is equal for all the measured data points. Using the Jacobian and σ, it is then possible to give an estimate fitting error for every parameter in the model. For the parameters, which are not directly in the model, such as Q_i, Gaussian uncertainty propagation is applied.

A.2 Weighting

In the case of ripples, we encountered that the fit of the circle looses accuracy, as data away from the resonance frequency had too much influence. Hence a weighting was introduced, where a weight is assigned to each measurement point. Data points near the resonance are set to weight 1, whereas for data far away from the resonance (around the full width half maximum and further, in the following formula called $width$) the weight of each data point is reduced. The following formula is used for the reduced weighting:

$$weight(f_i) = \frac{width}{|f_i - f_r|} \tag{A.2}$$

An example of a possible weighting is plotted in figure A.1.

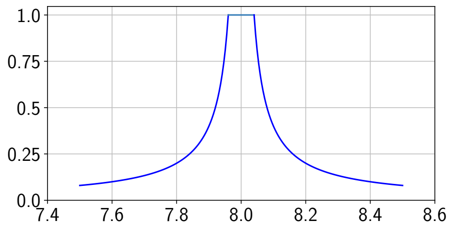

Figure A.1: Possible weighting function. In that example the resonance frequency is set to 8 GHz, and the width with constants weights to 40 MHz.

A.3 Technical remarks

Some technical details are given to the fitting routine, which are not important for the method of the general circle fit. However they give some input of how certain steps within the fit are implemented.

For the fitting of the delay, as well as for the background slope, the first 1/8 and last 1/8 of the data is taken. The slope is obtained with a linear fit to both parts simultaneously. Especially if the resonance has an undesired influence on the phase, for example a lasting 2π shift, a wrong value for the delay is obtained. However there is an option implemented to fit both parts independently, which can be set when calling the circle fit routine. More details are given in the help.

Within the final fit of Q_l to the magnitude, there is a positive magnitude, which might be counter intuitive for a resonance measured in transmission. The reason for this is that the actual calculation goes like $[1-(S_{21}^{ideal})]$, shifting the off resonant point to the origin. Otherwise it would lead to a more complex equation for the magnitude, leading to a less robust fitting routine.

For the comparison with the originally measured data, which is shown in the final plots, the model is calculated with the data obtained from the fits.

The circle fit typically works satisfactorily for Q_c/Q_i being between 0.01 and 100. In the over coupled case, the normalised circle passes close to the origin, leading to high uncertainties in Q_i. As Q_i is given by the distance between the circle crossing the real axis and the origin. In that case Q_l is still obtained accurately.

In the under coupled case, the resonance gets flatter, making it more difficult to perform the fit. Especially if the resonance is in the same order of magnitude as the ripples, the fitting routine might not work any more. This was an issue when doing measurements for increasing temperature with the aluminium stripline. As the temperature increases, Q_i decreases, while Q_c remains constant, leading to an increasingly over coupled setup.

Appendix B

Maxwell

Maxwell is a finite element simulation software, solving 2D and 3D structures in the electric, magnetostatic, eddy current and transient problem case [36]. It is similar to HFSS (see chapter 5.5) and also provided by Ansys. The difference is that Maxwell is focused on the static cases, whereas HFSS is a high frequency electromagnetic solver. In this thesis Maxwell was used to find values for the electrical properties of the stripline, discussed in chapter 7. For the work presented here, only the electrostatic and magnetostatic solutions in 3D were required, the discussion will only include these two. The chapter is based on [36] and [37].

B.1 Basics

The first steps, in doing simulations, are identical to the steps done in HFSS. The way a model is drawn, is exactly the same and the mesh is obtained in a similar style. Also the constraints for the mesh (like maximum length) can be assigned identical to HFSS.
The assignment of the ports, here called excitations, depends on the type of the required solutions, and is different to HFSS.
The solution process is similar to some extent, the solution itself is different again, as other quantities are of interest in Maxwell.
The following two chapters give detailed information on how to perform simulations for the magnetostatic and the electrostatic case. In the magnetostatic case, the inductance of a certain structure is computed, whereas the electrostatic case is used to obtain a value for the capacitance.

B.2 Magnetostatic simulations

To obtain values for the inductance of a structure, the magnetostatic solution type is chosen. A DC current is applied through the structure, therefore it has to be a conductor. In addition, it was found, that using PEC (Perfect Electric Conductor) as the material for the conductor, it did not work due to an occurring error. The reason for that is not clear. So it is advised to chose a material with high conductivity (like copper) for the conductor. There should be no impact on the result for the inductance. Typically the current excitation is assigned to a surface of the conductor. The amount of current can be chosen as a parameter. The surface, where it is assigned, has to coincide with the surface of the region confining the structure (see figure B.1). The region is explained in the next paragraph. The same amount of current has to leave and enter the conductor, so at least two ports have to be assigned. Through one port the current enters and through the other one it leaves the conductor. The current direction can be chosen in the assignment process. For linear systems the amount of current does not influence the value obtained for the inductance.

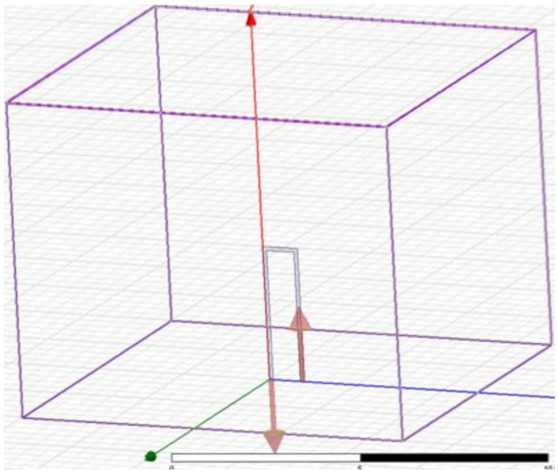

Figure B.1: Stripline in Maxwell to simulate the inductance. The two ports are shown (red arrows), one for the input, one for the output. The box around the stripline is the region confining the solution area.

To confine the structure to a certain area in space, a so called 'region' is drawn around the structure. This is done by selecting 'Draw' > 'Region'. A padding around the structure can be chosen. It was seen that the exact amount of padding does not have a critical influence. The only requirement is, that the current ports have to coincide with the surface of the region, so the padding for this surface is chosen to be 0. It is advisable to make the padding around the remaining structure on the order of the maximum dimension of the structure.
To obtain a value for the inductance, the current excitation has to be included in the inductance matrix. This is done in the project manager, under parameters, where the current source can be included (tick box). Otherwise Maxwell does not calculate (or at least give) a value for the inductance.
The solution can be found via the data table in the results of the project. The solution is given as a matrix of the inductances, which has a single entry in the case of two ports.

B.3 Electrostatic simulations

To get values for the capacitance, the chosen solution type is electrostatic. Voltage excitations are assigned and the whole object has to be on the same voltage, in contrast to the magnetostatic case, where the excitation is only assigned to a surface.
In the electrostatic case, the objects are completely inside the confining region, again in contrast to the magnetostatic case, where one surface has to be touching. A region,

confining the area to be solved, has to be drawn. The capacitance is then obtained between the objects, where a voltage is assigned.
Similar to the magnetostatic case, a matrix has to be assigned, where the voltage excitations have to be included to obtain a solution.
After doing this, the setup is solved and the capacitance matrix can be found in the solution data. It has an entry for every voltage excitation, giving the self capacitance and additional entries for the capacitance between the objects. More information about capacitance matrices is given in [38].
For a linear system the absolute amount of voltage does not influence the results, however different voltages may be used for the different objects.
In case of the stripline, two different sets of simulations were performed. In one case the capacitance between the waveguide and the stripline was of interest. Therefore the stripline was modelled as a single element. The confining region was chosen to have the same dimensions as the waveguide and a voltage was assigned to its surfaces. In this case, the size of the confining region matters, because the coupling between the stripline and the waveguide wall takes place, which is dependent on the distance.

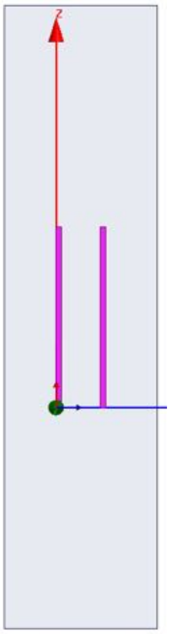

Figure B.2: Two rods of the stripline to simulate the capacitance between them. A voltage excitation is assigned to both of them. The sapphire substrate, which they are placed on, can be seen. The confining region (not shown) has the dimension of the waveguide.

In the second case, the shunt capacitance was of interest. In order to examine that, the top part of the stripline was excluded and both legs were set to a different voltage (see figure B.2). In addition, the wall was also set to a voltage, since the waveguide wall is a conductor, acting as a ground for the stripline. In both cases the silicon substrate was modelled accurately, identical to the HFSS simulations, as it influences the capacitance with its dielectric properties.
This chapter presented the basic tools on how to perform electrostatic and magnetostatic simulations using Maxwell. These are sufficient to obtain values for capacitance and inductance of a structure. Further information can be found in the sources, named in the beginning.

Appendix C

Multiple sample waveguide

A waveguide allowing to measure multiple samples was designed and fabricated. In the previous design, figure C.1, it was only possible to fit the samples in a single layer, which was exactly at the seam of the waveguide. To achieve critical coupling for the striplines, as described in chapter 7, they had to be placed in the center. So it was only possible to measure a single sample per cool down. This was inefficient and in addition, this design carried some difficulties in aligning the samples. Moreover, there were five slots symmetrical around the center, which resulted in a net of three different positions in the waveguide, due to the symmetric field of the fundamental mode.

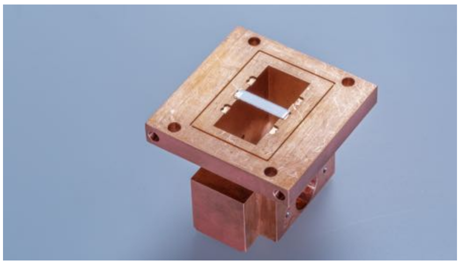

Figure C.1: Picture of the previous waveguide design with one sample placed in the center. Two identical halves are bolted together.

The new waveguide was fabricated from 5083 aluminium, in contrast to the previous one, where copper was used. Aluminium is superconducting [31] at the base temperature of the fridge, which prevents losses to the walls.
In the following section, the design considerations and the dimensions are given. The new mounting system is presented in the section after that. In the final part of this chapter, measurements at room temperature are shown, giving an insight on the waveguide's bandwidth.

C.1 General design considerations

Several considerations were taken into account designing this waveguide. They will be illustrated in this section, which gives some insight, why we ended up with the final design.
A sketch, where the inner dimensions are illustrated can be found in figure C.5 (left).

Additionally the sample holder is shown, which is discussed in the next section. The cutoff was designed to be around 6.5 GHz, required for the qubit frequency to be below cutoff. This is still well below the frequency of the stripline resonators, such that they can serve as readout resonators in future experiments. Based on equation 3.24, giving the cutoff frequency, the width was chosen to be 23 mm.
The height was chosen to be 11 mm. On the one hand, the waveguide should be high enough not to be limited by effects from the wall, therefore a higher waveguide is favourable. On the other hand the mounting system (described in the next section) takes some space, and the samples themselves should preferably be in the middle of the waveguide. Furthermore, we want to operate the waveguide on the fundamental mode, so the length of the shorter edge should be well below the length of the longer one. So the cutoff frequency of the TE_{10} mode should be several GHz below the cutoff of the TE_{01} mode.
The substrates holding the samples could not be modified, as they were already fabricated and are 18 mm long, with the stripline sitting in the middle. Taking the mounting system and the wall thickness into account, which adds up to around 5 mm, 11 mm was a decent choice. Furthermore to improve the mounting in terms of position accuracy, the substrates came through the waveguide on the bottom, also giving a constraint on the height.

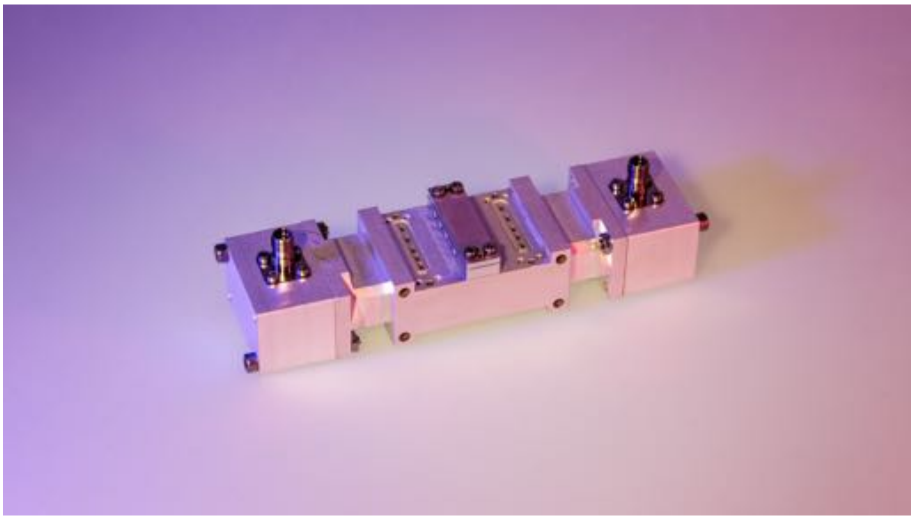

Figure C.2: Picture of the total assembled waveguide. Two identical parts in the beginning and in the end, to launch and receive signal. The SMA connector is seen on top. The samples are placed in the middle section of the waveguide. For one of the set of slots, a sample holder is placed, the other two a are left open for illustration purposes.

The waveguide consists out of three parts. There is the middle part containing the samples, one part to launch and another identical one on the other end to receive the signal. This gives flexibility in future setups, as the middle section can be exchanged, with the couplers remaining the same. In addition, this prevents losses to the seam (discussed in 6.3) at the position of the samples, as the seam is further away.
The waveguide consisting out of the three parts is seen in figure C.2. A picture of the opened up waveguide, with the begin/end part in front is seen in figure C.3. On top of the the middle part, before and after the slots for the samples, there are two indentations, which can be used for coils to apply a magnetic field. Aluminium becomes superconducting, hence this is only useful for a copper waveguide. The distance between

Figure C.3: The waveguide opened up. In the foreground the begin/end part is seen, with a coupler inside. The middle section is placed in the background.

different sets of sample slots was chosen to be 15 mm, to have around $\lambda/2$ in between them. A design with three sets of slots was chosen, to test three samples during the same cool down, which was sufficient for the first layout. Three sets of sample slots were also chosen to limit the overall length of the waveguide.
The mounts for the substrates themselves were then screwed from top, with the samples mounted to them. This is explained in the next section.

C.2 The mounting system

In this section, the mounting system for the samples is described.

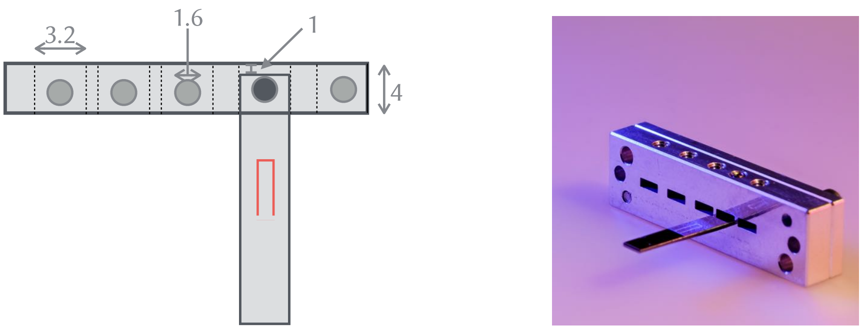

Figure C.4: Left: Sketch of the sample holder. The screw holes to fix the samples are illustrated. 1 mm distance to the top is due to a lid with 1 mm counter parts, shifting the substrates down. The given dimensions are accurate, as it is a sketch the drawing is only approximate. All dimensions in mm. Right: Picture of the sample holder with a substrate.

The mounting is done with the component illustrated in figure C.4 on the left (picture on the right). It can be slided in from top, already containing the samples (see figure C.6). The whole assembly, composed of the waveguide in combination with the mounted samples is illustrated in C.5 on the left. A picture of the waveguide with the slided in sample is shown in C.5 on the right. The advantage is, that samples can be switched without opening up the whole waveguide, which was necessary in the old design. Furthermore the alignment is more precise, as the substrate goes through the waveguide into the slot on the bottom.

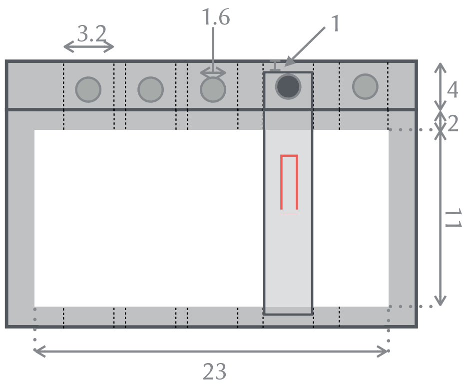

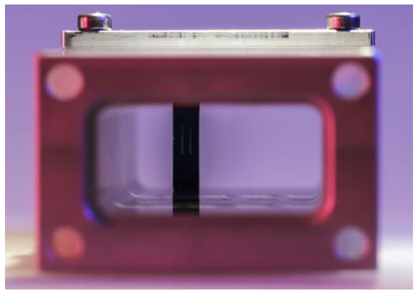

Figure C.5: Left: Sketch of the sample holder, slided in the waveguide. The wall thickness of 2 mm is only sketched at the top. It is also seen, that the substrates goes through the entire waveguide. All dimensions in mm. Right: Picture of the middle section of the waveguide with the sample inside.

The slots are situated around a central one. Two are as close as possible, with a separation of 0.5 mm. The other two are optimised to use all the space. This results in an asymmetric design, which gives slots at a different field strength in total five. The substrates were measured to be 3.1 mm, so the sample holders were chosen to have slits with 3.2 mm. The substrates themselves are fixed with screws.
The slits for the samples were required to have sharp edges, therefore they were fabricated using a wire erosion machine. This requires to have a slit through the hole sample holder and the waveguide. To close the sample holder, lids were constructed, which got screwed on top. To shift the sample down, the lids had a counter part of 1 mm coming from top. This was necessary to move the striplines further into the waveguide.

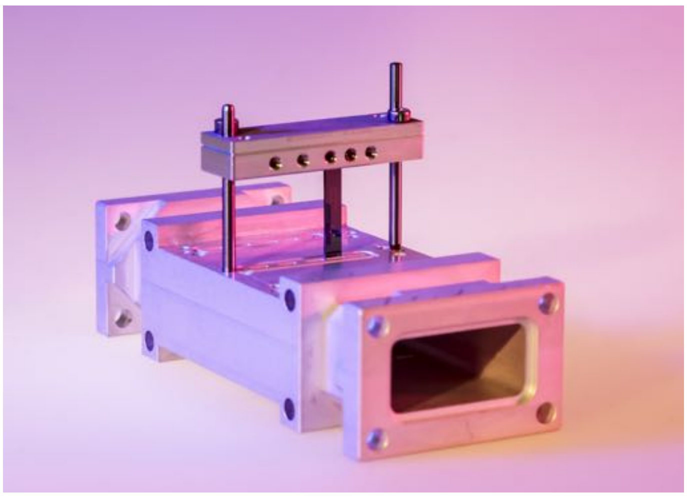

Figure C.6: Image of the sample mounting. The sample holder with a stripline is shifted in from the top. Two metal rods are used as guidance, which prevent the sample form being scratched.

In addition, there is also a lid from the bottom. This allows to check, if the sample is aligned properly before closing it.

To prevent the samples from being scratched, two guiding metal rods at the sides were used, which guide the sample holder when sliding in. Afterwards the metal rods can be removed. A picture of the assembly process is shown in figure C.6.

C.3 Room temperature measurement

Before the samples themselves are mounted, the bandwidth of the waveguide has to be tuned. The reason for this is impedance matching. The cable from the VNA has an impedance of 50 Ω, while the waveguide itself has, depending on the frequency, 377 Ω or above (equation 3.15). Two components are used for the matching.

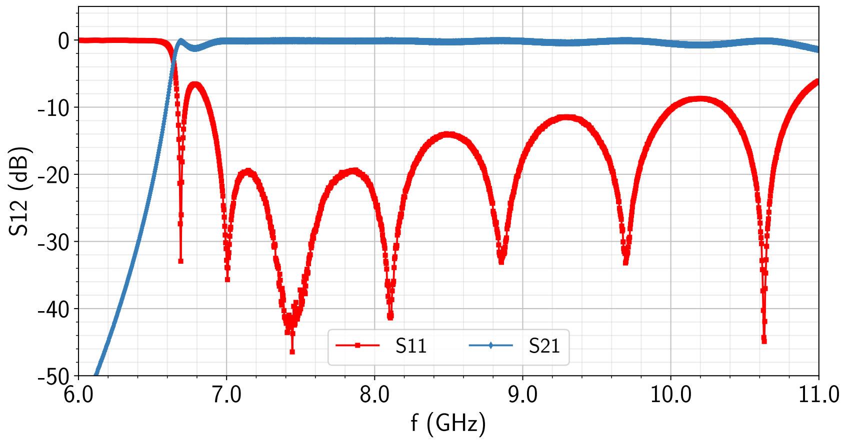

Figure C.7: S parameter measurements of the tuned waveguide at room temperature. The waveguide has a cutoff around 6.6 GHz. It works well in a range from 7 GHz to 8.2 GHz. It still works to some extent till 10.8 GHz

Screws from the bottom are screwed to different lengths inside the waveguide, displacing the field inside and improving the transmitted signal.
The coupler pin itself is such, that the diameter of the inner SMA conductor continues and is terminated by a wider cylinder of several mm length. This enhances the impedance matching.
Typically the bandwidth is given for the S_{11} parameter to be below −20 dB, with the S_{21} parameter showing transmission. In figure C.7 the S parameters after tuning with the best working coupler is presented.
The waveguide has the cutoff around 6.6 GHz, which is within the expectations of the designed cutoff. The bandwidth where it works well is between 7 GHz and 8.2 GHz. It still can be used as a waveguide up to 10.8 GHz. In this case the waveguide was not tuned for maximal bandwidth, but such that the striplines, having their resonances between 7.3 GHz and 8 GHz are well in the band. This requirement was full filled.

Appendix D

Complete measurement setup

In this part of the appendix the full measurement setup is shown and briefly described. In figure D.1 the measurement setup is illustrated. The microwave signal prob-

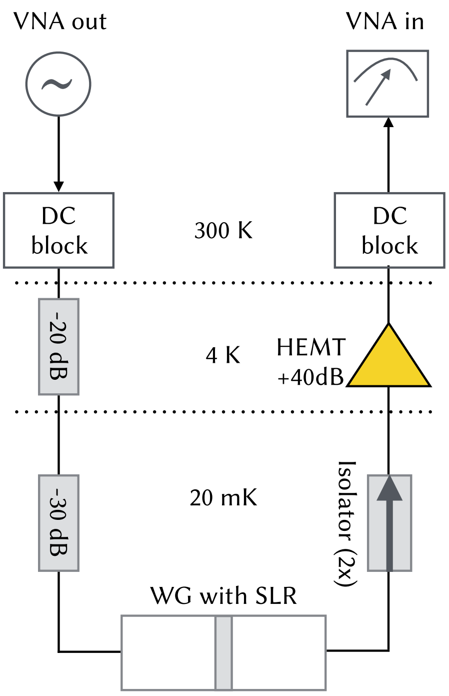

Figure D.1: Full measurement setup. Details are explained in the text.

ing the sample, in this case the stripline, is generated by a VNA, indicated with 'VNA out'. This is followed by a DC block, which prevents DC currents to flow. The black lines represent the microwave lines.

After the DC block the signal enters the fridge and is attenuated at 4 K by 20 dB. At the base plate, which is at a temperature of around 20 mK, the signal is attenuated additionally with 30 dB. Then it enters the waveguide, where the stripline is placed. The microwave propagates through the waveguide and leaves it on the other end.

After the waveguide two isolators are placed, which prevent the signal being reflected back into the waveguide. At the 4 K stage the signal is amplified by 40 dB, using a HEMT (high electron mobility transistor) amplifier. After the HEMT another DC block

is placed, again to prevent a DC current flow.
Finally the microwave signal enters the VNA and gets measured.